

**ANISOTROPIC PARAMETERS OF MESH FILLERS RELEVANT  
TO MINIATURE CRYOCOOLERS**

A Thesis  
Presented to  
The Academic Faculty

by

Evan Landrum

In Partial Fulfillment  
of the Requirements for the Degree  
Master of Science in Mechanical Engineering in the  
School of Mechanical Engineering

Georgia Institute of Technology  
May, 2009

**ANISOTROPIC PARAMETERS OF MESH FILLERS RELEVANT  
TO MINIATURE CRYOCOOLERS**

Approved by:

Dr. S. Mostafa Ghiaasiaan, Advisor  
School of Mechanical Engineering  
*Georgia Institute of Technology*

Dr. Sheldon M. Jeter  
School of Mechanical Engineering  
*Georgia Institute of Technology*

Dr. Carl S. Kirkonnell  
Space & Airborne Systems  
*Raytheon Company*

Dr. Prateen V. Desai  
School of Mechanical Engineering  
*Georgia Institute of Technology*

Date Approved: April 1, 2009

To my parents, Michael and Christine Landrum

## ACKNOWLEDGEMENTS

First and foremost, I would like to thank my advisor, Dr. S. Mostafa Ghiaasiaan, for giving me the opportunity to join the Georgia Tech Cryocooler Research group in the Fall semester of 2007 as a graduate research assistant. This experience not only opened my eyes to the vast industry of cryogenics and their applications, but also helped fund my graduate studies. Dr. Ghiaasiaan's patience and advice were always appreciated when overcoming research challenges. I am very grateful to have worked with such a talented person and trust that any other students who join the team will share the same sentiment.

While working within the research group, I was fortunate to work with an outstanding graduate student, Ted Conrad. His years of experience with research helped to answer many questions I had along the way, offering insight and solutions for tackling design challenges. Ted was also an outlet for time away from research where we could discuss current events and news. In all, his presence made for a much more pleasant working environment. Furthermore, Ted had a substantial impact on the information presented in this thesis and deserves much credit for his contributions. He helped with a range of activities including integrating the data acquisition system and writing the post-processing code utilized for the oscillatory flow cases. Without his input, this collaborative endeavor would not have been a success.

I would also like to thank my committee members Dr. Sheldon M. Jeter, Dr. Prateen V. Desai and Dr. Carl S. Kirkconnell for their participation in my thesis review. Dr. Jeter is a current professor in the Mechanical Engineering department with specializations in energy systems and Dr. Desai is a Mechanical Engineering professor

Emeritus and former head of the Cryocooler Research Group. I thoroughly enjoyed taking Dr. Jeter's thermodynamics courses. Dr. Kirkconnell of Raytheon Space and Airborne Systems provided valuable input on projects and his continued involvement in the GT Cryocooler Group is greatly appreciated.

Lastly, I would like to thank my family. My parents, Michael and Christine, have continually supported me in many ways throughout my life and I am forever indebted to them. Even at a young age, my parents encouraged my brother, Ian, and I to set high goals and work hard to achieve them. Education and academics remained a core priority in my family and lay the foundation for much of my own successes. My fiancé, Sara, has also been a tremendous force in my life. She understands the hectic schedule of a graduate student and was always able to cheer me up even in the darkest hour. I am very lucky to have found such a great person to share my life with.

# TABLE OF CONTENTS

	Page
<b>ACKNOWLEDGEMENTS</b>	<b>iv</b>
<b>LIST OF TABLES</b>	<b>ix</b>
<b>LIST OF FIGURES</b>	<b>x</b>
<b>NOMENCLATURE</b>	<b>xiii</b>
<b>SUMMARY</b>	<b>xviii</b>
<b>1 INTRODUCTION</b>	<b>1</b>
1.1 Cryocooler Background	1
1.2 Pulse Tube Refrigerator's Inception	7
1.3 The Modern Pulse Tube Refrigerator	12
1.4 Project Motivation and Rationale	15
<b>2 THEORY</b>	<b>18</b>
2.1 Fundamental Analysis	18
2.2 Porous Media Theory	20
<b>3 EXPERIMENTAL METHODOLOGY</b>	<b>30</b>
3.1 General Remarks	30
3.2 Steady Axial Flow	33
3.3 Steady Radial Flow	37
3.4 Oscillatory Axial Flow	42
3.5 Oscillatory Radial Flow	46
<b>4 COMPUTATIONAL METHODOLOGY</b>	<b>50</b>
4.1 General Remarks	50
4.2 Steady Axial Hydrodynamic Parameterization	53
4.3 Steady Radial Hydrodynamic Parameterization	56
4.4 Oscillatory Axial Hydrodynamic Parameterization	58
4.5 Oscillatory Radial Hydrodynamic Parameterization	62

<b>5</b>	<b>RESULTS</b>	<b>64</b>
5.1	Steady Flow Results	64
5.2	Pressure Dependence Study	74
5.3	Oscillatory Flow Results	82
<b>6</b>	<b>CONCLUDING REMARKS</b>	<b>98</b>
	<b>APPENDIX A: Steady Flow Data</b>	<b>105</b>
A.1:	Steady Axial Flow Experimental Data	105
A.1.1:	#325 Phosphor Bronze - 67.38% Porosity	105
A.1.2:	#635 Stainless Steel - 63.12% Porosity	105
A.2:	Steady Radial Flow Experimental Data	106
A.2.1:	#325 Phosphor Bronze - 67.02% Porosity	106
A.2.2:	#635 Stainless Steel - 63.04% Porosity	107
	<b>APPENDIX B: UDF Pressure Inlet Boundary Condition</b>	<b>108</b>
	<b>APPENDIX C: Oscillatory Experimental Data</b>	<b>109</b>
C.1:	Oscillatory Axial Flow Pressure Waveform Data	109
C.1.1:	#325 Phosphor Bronze - 67.38% Porosity	109
C.1.2:	#635 Stainless Steel - 63.12% Porosity	109
C.2:	Oscillatory Radial Flow Pressure Waveform Data	110
C.2.1:	#325 Phosphor Bronze - 67.02% Porosity	110
C.2.2:	#635 Stainless Steel - 63.04% Porosity	110
C.3:	Oscillatory Axial Flow Pressure Plot Comparison Data	111
C.3.1:	#325 Phosphor Bronze - 67.38% Porosity	111
C.3.2:	#635 Stainless Steel - 63.12% Porosity	111
C.4:	Oscillatory Radial Flow Pressure Plot Comparison Data	112
C.4.1:	#325 Phosphor Bronze - 67.02% Porosity	112
C.4.2:	#635 Stainless Steel - 63.04% Porosity	112
	<b>APPENDIX D: Simulation Dimensions</b>	<b>113</b>

D.1: Steady Axial Flow Experimental Setup Grid Vertices	113
D.2: Steady Radial Flow Experimental Setup Grid Vertices	114
D.3: Oscillatory Axial Flow Experimental Setup Grid Vertices	115
D.4: Oscillatory Radial Flow Experimental Setup Grid Vertices	116
D.4.1: Large Radial Housing Unit	116
D.4.2: Small Radial Housing Unit	117
<b>APPENDIX E: Pressure Dependence Study</b>	<b>118</b>
E.1: Experimental Data	118
E.1.2: #325 Stainless Steel - 69.69% Porosity	118
E.1.2: #400 Stainless Steel - 69.69% Porosity	120
E.1.3: #400 Sintered Stainless Steel - 61.65% Porosity	121
E.1.4: Metal Foam - 55.47% Porosity	122
E.2: Experimental Setup Control Schematic	124
E.3: Test Setup Grid Vertices	124
E.4: Simulated Fluid Control Volume	125
<b>REFERENCES</b>	<b>126</b>

## LIST OF TABLES

	Page
Table 1.1: PTR developmental milestones	12
Table 3.1: Steady and oscillatory flow test sample details	33
Table 3.2: Radial housing unit application	49
Table 4.1: Limits of convergence criteria	52
Table 4.2: Material property input values	53
Table 4.3: Experimental FFT representation of #325 Ph-Brz data for axial flow	60
Table 4.4: Unsteady simulation time steps	61
Table 5.1: Steady flow sample hydrodynamic parameters	71
Table 5.2: Reynolds ranges for steady flow tests	74
Table 5.3: Pressure dependence study axial sample details	75
Table 5.4: Pressure independent steady axial hydrodynamic parameters	79
Table 5.5: Reynolds ranges for pressure dependence study	80
Table 5.6: Average oscillatory flow sample hydrodynamic parameters	95

## LIST OF FIGURES

	Page
Figure 1.1: Recuperative cryocooler schematics; (A) Reverse Brayton cycle, (B) JT cryocooler	2
Figure 1.2: Regenerative cryocooler schematics; (A) GM PTR, (B) Inertance tube PTR (ITPTR), (C) Stirling expander	4
Figure 1.3: Single Stage (RP-1512A) and multi-stage (RP-052A) PTR photographs (Janis Research Company)	5
Figure 1.4: (A) Single-stage and (B) multi-stage PTR schematics	6
Figure 1.5: Stirling expander diagram	7
Figure 1.6: Ideal Stirling cycle diagrams	8
Figure 1.7: Basic pulse tube refrigerator (BPTR) diagram	10
Figure 1.8: 120 Hz miniature PTR experimental system (NIST)	14
Figure 3.1: Mesh filler sample cuts	31
Figure 3.2: Plain square weave	32
Figure 3.3: Steady axial flow experimental setup diagram	34
Figure 3.4: Steady axial flow test section exploded CAD view	35
Figure 3.5: Steady axial flow experimental setup photograph	35
Figure 3.6: Steady axial flow experimental setup detailed CAD view	36
Figure 3.7: Steady radial flow experimental setup diagram	38
Figure 3.8: Steady radial flow test section exploded CAD view	39
Figure 3.9: Radial flow test section photograph	40
Figure 3.10: Steady radial flow experimental setup photograph	40
Figure 3.11: Steady radial flow test section detailed CAD view	41
Figure 3.12: Oscillatory axial flow experimental setup diagram	42
Figure 3.13: Oscillatory axial flow experimental setup photographs	43

Figure 3.14: Oscillatory axial flow test section detailed CAD view	44
Figure 3.15: Compressor response curves for oscillatory axial flow cases	45
Figure 3.16: Oscillatory radial flow experimental setup diagram	46
Figure 3.17: Oscillatory radial flow experimental setup photographs	47
Figure 3.18: Oscillatory radial flow test section detailed CAD view	47
Figure 3.19: Radial housing units	49
Figure 4.1: Steady axial flow mesh	54
Figure 4.2: Steady radial flow mesh	56
Figure 4.3: Oscillatory axial flow mesh	58
Figure 4.4: Oscillatory radial flow mesh for large radial housing unit	62
Figure 5.1: Pressure contour of #325 Ph Brz steady axial flow case at 0.546 g/s	65
Figure 5.2: Steady axial flow pressure plot	66
Figure 5.3: Vector plot of #635 stainless steel radial porous sample at 1.218 g/s	67
Figure 5.4: Steady radial flow pressure plot	69
Figure 5.5: Steady flow friction factors based on Darcy permeability	72
Figure 5.6: Steady flow friction factors based on viscous resistance	73
Figure 5.7: #325 stainless steel (69.69%) pressure plot	76
Figure 5.8: #400 stainless steel (69.69%) pressure plot	77
Figure 5.9: Sintered #400 stainless steel (61.65%) pressure plot	77
Figure 5.10: Metal foam (55.47%) pressure plot	78
Figure 5.11: Steady axial flow friction factors based on Darcy permeability	80
Figure 5.12: Steady axial flow friction factors based on viscous resistance	81
Figure 5.13: #635 stainless steel axial flow pressure plots at 50 Hz low flow conditions (3.51 MPa)	84
Figure 5.14: #635 stainless steel radial flow pressure plots at 50 Hz low flow conditions (3.44 MPa)	84

Figure 5.15: #635 stainless steel axial flow pressure plots at 75 Hz (3.54 MPa)	85
Figure 5.16: #635 stainless steel axial flow pressure plots at 125 Hz (3.58 MPa)	86
Figure 5.17: #635 stainless steel axial flow pressure plots at 175 Hz (3.61 MPa)	86
Figure 5.18: #635 stainless steel axial flow pressure plot at 100 Hz (2.87 MPa)	88
Figure 5.19: #635 stainless steel axial flow pressure plot at 150 Hz (2.89 MPa)	88
Figure 5.20: #635 stainless steel radial flow pressure plot at 100 Hz (2.88 MPa)	90
Figure 5.21: #635 stainless steel radial flow pressure plot at 200 Hz (2.84 MPa)	90
Figure 5.22: #325 phosphor bronze axial flow pressure plot at 50 Hz (3.51 MPa)	92
Figure 5.23: #325 phosphor bronze axial flow pressure plot at 200 Hz (2.88 MPa)	92
Figure 5.24: #325 phosphor bronze radial flow pressure plot at 100 Hz (2.82 MPa)	93
Figure 5.25: #325 phosphor bronze radial flow pressure plot at 150 Hz (3.44 MPa)	94
Figure 5.26: Friction factor comparison for #325 phosphor bronze sample	96
Figure 5.27: Friction factor comparison for #635 stainless steel sample	96

## NOMENCLATURE

### Variables

$A$	Cross-sectional Area ( $m^2$ )
$\bar{C}, C$	Inertial resistance tensor, scalar ( $m^{-1}$ )
$c_f$	Forchheimer's inertial coefficient ( - )
$d$	Diameter ( $m$ )
$\bar{D}, D$	Viscous resistance tensor, scalar ( $m^{-2}$ )
$e$	Total specific energy ( $J/kg$ )
$\varepsilon$	Sample porosity ( - )
$f$	Friction factor ( - )
$\bar{F}$	Volumetric force vector ( $N/m^3$ )
$h$	Enthalpy ( $J/kg$ )
$k$	Thermal conductivity ( $W/m \cdot K$ )
$K$	Darcy permeability ( $m^2$ )
$l$	Length of sample ( $m$ )
$\lambda$	Frequency ( $Hz$ )
$m$	Mass ( $kg$ )
$\dot{m}$	Mass flow rate ( $kg/s$ )
$\mu$	Dynamic viscosity ( $kg/m \cdot s$ )
$P$	Thermodynamic pressure ( $N/m^2$ )
$\varphi$	Phase angle ( $rad$ )
$\omega$	Angular frequency ( $rad/s$ )
$Q$	Heat transfer ( $J$ )

$r$	Radial coordinate ( $m$ )
$\bar{R}$	Specific gas constant ( $J/kg \cdot K$ )
$Re$	Reynolds number ( - )
$\rho$	Density ( $kg/m^3$ )
$S$	Entropy ( $J/K$ )
$t$	Time ( $s$ )
$T$	Local instantaneous temperature, volume averaged intrinsic temperature ( $K$ )
$\bar{\tau}$	Viscous stress tensor ( $N/m^2$ )
$\bar{u}, u$	Superficial velocity vector, magnitude ( $m/s$ )
$V$	Volume ( $m^3$ )
$\bar{v}$	Local instantaneous velocity vector, physical velocity vector ( $m/s$ )
$x$	Axial coordinate ( $m$ )
$Z$	Pressure amplitude ( $Pa$ )

### **Subscripts**

annular	Annular sample
avg	Average
$bf$	Body force
comp	Compression
cyl	Cylindrical sample
$D$	Viscous resistance coefficient basis
$f$	Fluid

exp	Expansion
heatpump	Heat pumping action
$i$	Directional bases
id	Inner diameter
$K$	Darcy permeability basis
od	Outer diameter
PV	Pressure-volume
$r, x, \theta$	Cylindrical coordinate bases
refrig	Refrigeration
rej	Rejection
regen	Regenerative
sol	Solid
tot	Total

### **Notations**

$\langle \rangle$	Time averaged quantity
$\nabla$	Del operator

### **Abbreviations**

AC	Alternating current
BPTR	Basic pulse tube refrigerator
CAD	Computer aided design
CHX	Cold heat exchanger
CFD	Computation fluid dynamics

DC	Direct current
DIOPTR	Double inlet orifice pulse tube refrigerator
DMM	Digital multimeter
FFT	Fast Fourier transform
FOUD	First order upwind discretization scheme
GM	Gifford-McMahon
ITPTR	Inertance tube pulse tube refrigerator
JT	Joule-Thomson
MEMS	Micro-electro-mechanical systems
OPTR	Orifice pulse tube refrigerator
P1	Pressure measurement at location 1
P2	Pressure measurement at location 2
PhBrz	Phosphor bronze
PISO	Pressure-implicit with splitting operators pressure-velocity scheme
PT	Pulse tube
PTR	Pulse tube refrigerator
PWG	Pressure wave generator
RLITPTR	Reservior-less inertance tube pulse tube refrigerator
SOUND	Second order upwind discretization scheme
SS	Stainless steel
TX	Transfer line
UDF	User defined function
V1	Shutoff valve 1

V2

Shutoff valve 2

WHX

Warm heat exchanger

## SUMMARY

Pulse tube refrigerators (PTR) are a robust type of cryogenic refrigerator or cryocooler able to reach temperatures ranging from 120 K to near absolute zero through single and multistage configurations. Their applications span a wide array of platforms including superconductors, biological preservation as well as thermal management of various sensory devices. Most of these applications are reserved for high-end military and space operations but the industry is evolving towards commercial uses.

Unlike the traditional vapor-compression cycle, PTRs operate by means of oscillating flows created by a pressure wave generator (PWG) in which the working fluid is continually expanded and compressed throughout a closed system. PTRs achieve their desired cooling effects through storage and transfer of thermal energy between various internal components and the external environment. Enthalpy flows and ultimately system efficiencies are highly dependent upon the relationship between the volumetric flow rate and dynamic pressure at point locations within the system. Thermoacoustics, which combines thermodynamics and the harmonic nature of acoustics, is often used for analysis of governing processes. Although the flow and transport phenomena within cryocoolers are not entirely understood, knowledge and control of these processes has led to advancements in design and increases in system performance.

Throughout the last decade, research and development has sought to increase system performance while minimizing parameters such as mass, volume, cost and input power. The concept and implementation of such small-scale devices has been

experimentally demonstrated, however, the productization and subsequent commercial availability of such systems has yet to be seen. Design, construction and analysis of miniature PTRs give rise to a whole host of challenges not seen in their larger counterparts including increased surface to volume effects, amplified sensitivity to parasitic loads and proper thermal management at decreased length scales.

There are a number of methods and tools available for design, modeling and optimization of PTR systems; however, their accuracy at predicting processes of small scale devices is questionable. Some of the more advanced models utilize one-dimensional governing equations and empirical correlations obtained from standard scale devices. Computational fluid dynamics (CFD) modeling is possibly the best available technique in designing and predicting the performance of miniature Stirling and PTR systems. CFD modeling, like other hydrodynamic analysis tools, requires realistic closure relations for the micro porous materials housed within their regenerators and heat exchangers. The closure relations appear as terms in the momentum and energy governing equations. With respect to hydrodynamics, for example, they show up in the form of hydrodynamic resistance coefficients or friction factors.

Comprehensive prediction of fluid-solid interaction through this media can be obtained only by direct pore level simulation; a process which is time consuming and impractical for system level design calculations. Through the application of empirical correlations including the Darcy permeability and Forchheimer's inertial coefficient, the microscopic momentum equations governing the fluid behavior within the porous structure can be recast as viable macroscopic governing equations. With these

constitutive relationships, CFD can be an efficient and powerful tool for system modeling and optimization.

The purpose of this thesis is to determine the hydrodynamic parameters of two of the best commercially available mesh filler materials suitable for miniature PTRs; stacked screens of #635 stainless steel and #325 phosphor-bronze wire mesh cloth. Modular setups were designed and fabricated to measure steady and oscillatory pressures and mass flow rates of research grade helium. Experimental measurements were used as input boundary conditions for a CFD model replicating the sample test section and its vicinity. An iterative process would determine the resistance parameters by matching experimental results to those determined by the simulation. Hydrodynamic parameters for the two mesh fillers were determined for steady-state and steady periodic flow in both the axial and radial directions for a range of flow rates, operating frequencies and charge pressures. The effect of average pressure on the steady axial flow hydrodynamic parameters of other common PTR filler materials was also investigated. This form of determining sample hydrodynamic parameters and their subsequent computational and experimental methodologies were developed by Harvey (2003, [12]) and Cha (2007, [1]).

Directional hydrodynamic resistances are found for the #635 stainless steel and #325 phosphor-bronze mesh samples which minimize the error between simulated and experimental output variables. The results indicate large differences between the directional hydrodynamic resistance parameters for steady and oscillating flow regimes.

# 1 INTRODUCTION

## 1.1 Cryocooler Background

Until the mid 1950s much of the world's refrigeration needs were met by the traditional vapor-compression cycle as seen in classical thermodynamics which achieved evaporator temperatures of about 230 K [Radebaugh (1999, [24])]. As technology advances, there is an increased demand for thermal management at very low temperatures for application in a multitude of fields including medicine, electronics, food and the superconducting industry. This demand is met with the development and use of compact high-performance cryogenic refrigerators or cryocoolers. Cryocoolers can obtain no load temperatures in the range of 120 K to near absolute zero through single and multi-staged setups. Some examples of cryocooler applications include thermal management of optical sensors, tissue ablation, gas liquefaction and preservation of biological material. Most of these applications are reserved for high-end military and space operations but the industry is evolving towards commercial uses.

Cryocoolers, unlike the conventional vapor-compression cycle, utilize very different operating principles for the desired refrigeration effects. The wide variety of systems can be categorized by their processes of heat transfer; regenerative or recuperative. Recuperative cryocoolers function through a continuous flow of refrigerant and employ only recuperative heat exchangers, [Radebaugh (1999, [24])] where heat flows constantly from one location within the fluid flow loop to another. Some examples of recuperative cryocoolers include the Joule-Thomson (JT) and reverse Brayton cryocoolers as illustrated in Figure 1.1.

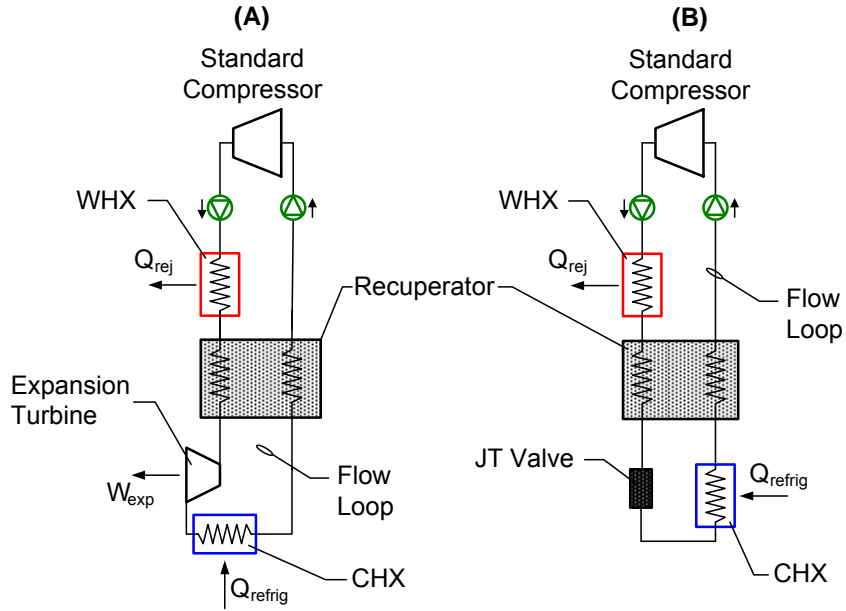


**Figure 1.1: Recuperative cryocooler schematics; (A) Reverse Brayton cycle, (B) JT cryocooler**

These systems resemble a vapor-compression cycle but make use of recuperative heat exchangers due to a much larger temperature difference within the fluid flow loop. The warm heat exchanger (WHX) or aftercooler rejects enthalpy gained by the input compressor work while the cold heat exchanger (CHX) provides refrigeration for the desired environment. The JT cryocooler employs large pressure ratios and contains a JT orifice or throttling device to achieve its cooling effect. The reverse Brayton cryocooler possesses similar components; however, it employs an expansion turbine to reduce fluid pressure within the flow loop. High performance miniature Turbo-Brayton cryocoolers have shown much success in space-borne applications. Using gas bearings, these balanced expansion turbines can rotate at extremely high speeds with very little vibration. Steady flow cryocoolers are driven by a conventional two port compressor containing a fixed low pressure inlet and high pressure outlet. Compressor valves and increased

pressure ratios required for recuperative cryocoolers significantly limits system efficiency [Radebaugh (1999, [24])].

Regenerative type cryocoolers operate under an oscillatory flow regime. They utilize a regenerator which stores thermal energy within its porous structure for one half of its cycle and then releases it. A standard two-port compressor can only achieve this type of flow through a rotating valve assembly resulting in oscillating pressures. More often a simple piston cylinder assembly, known as a Stirling compressor or pressure wave generator (PWG) is coupled with regenerative units. These compressors contain a single port and are commonly designed with dual opposed pistons for vibrational stability. A Stirling compressor is usually preferred for high end applications as the rotating valve assembly is a huge source of irreversibility and limits reliability and operating life. Some types of regenerative cryocoolers include the Stirling expander, pulse tube refrigerator (PTR) and Gifford-McMahon (GM) PTR.

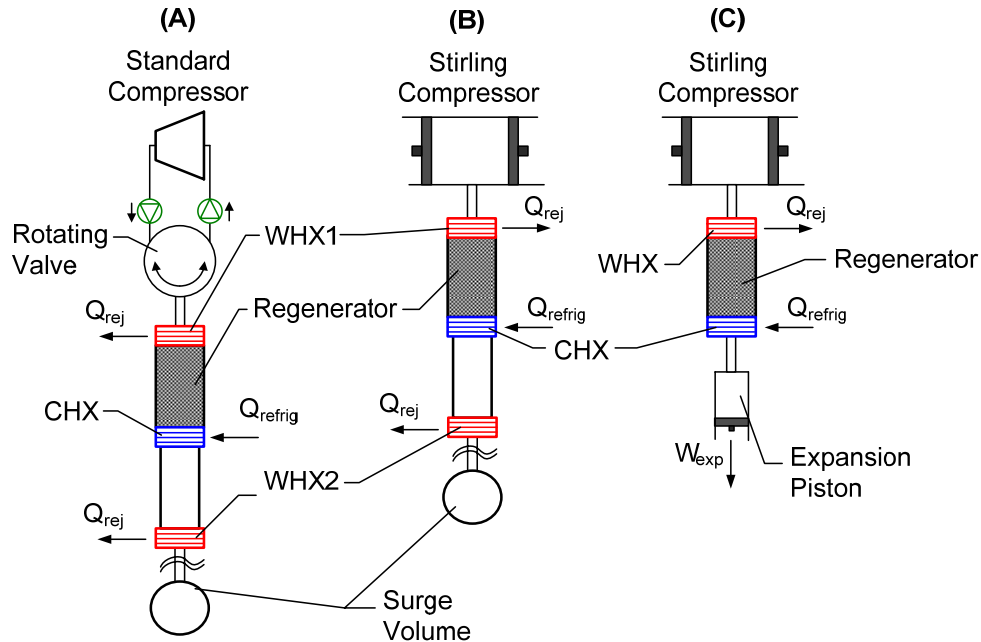


**Figure 1.2: Regenerative cryocooler schematics; (A) GM PTR, (B) Inertance tube PTR (ITPTR), (C) Stirling expander**

Cryocoolers function with a vast array of cryogenes or mixture of cryogenes typically having boiling points less than 120 K. Working fluids are chosen due to their high ratio of specific heats as well as their increased thermal conductivity. Some of these fluids include several forms of helium, oxygen, nitrogen, methane, ethane and propane [Radebaugh and Gully (2008, [25])]. Like all refrigeration systems, assurance of a hermetically sealed construction is vital to proper operation. Cleaning processes must also be followed when assembling cryocoolers to minimize contaminants as they can degrade performance.

Compressor specifications are often suited for individual cryocooler design needs as cryocooler performance and reliability go hand in hand with its associated power input. Industrial cryocoolers can even utilize input power from oscillating pressures created by thermoacoustic drivers. Mitigating gas leakage, increasing operating life and

other such challenges are the impetus of ongoing research. Other important cryocooler design parameters include cooldown time, acoustic noise as well as size and weight. Electromagnetic interference may also play an important role in applications where cryocoolers may disrupt or degrade onboard electronics.

Depending on the particular application, these systems can be configured in single and multi-staged designs. By staging the device, different cooling loads and temperatures can be directed to precise locations through a single unit and compressor. Secondary and tertiary stages achieve lower cold tip temperatures by means of heat rejection at lower temperatures. A comparison of single and multistage PTR units can be seen in Figure 1.3 and Figure 1.4. There are several PTR design configurations, each offering unique positions and orientations of the regenerator, pulse tube and their adjoining heat exchangers. Shapes include linear, u-tube and concentric tube designs. Many of these models will combine the warm heat exchangers into a single flange in order to simplify thermal rejection.



**Figure 1.3: Single Stage (RP-1512A) and multi-stage (RP-052A) PTR photographs (Janis Research Company)**

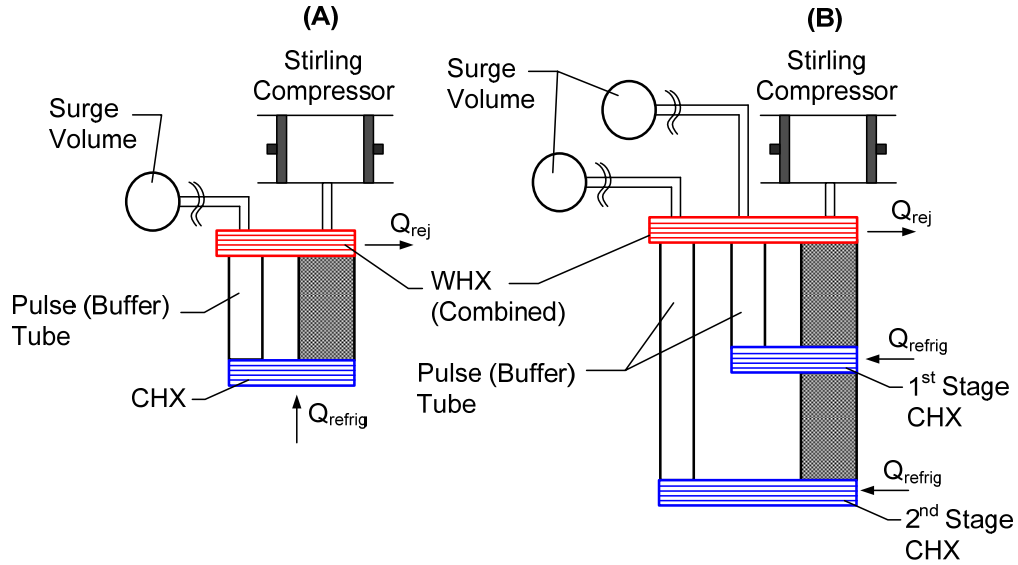


**Figure 1.4: (A) Single-stage and (B) multi-stage PTR schematics**

A cryocooler's performance is commonly characterized through load curves. These maps display the system's cooling power for a given set point temperature associated with the CHX and desired cooling environment. The adiabatic case or point of no heat lift is the ultimate temperature the cryocooler will reach. If the system has multiple stages, then a surface of configurations is presented where cooling load and temperatures are assigned for each primary, secondary and tertiary stages. These curves may be further categorized by localizing other system parameters such as compressor input power.

Cryocooler systems are very sensitive to external heat loads and precautions must be taken to mitigate parasitic losses. Typically units are housed within a vacuum dewar and low temperature components are shielded to eliminate radiative losses.

## 1.2 Pulse Tube Refrigerator's Inception

This investigation focuses on regenerative cryocooler components; in particular, those related to the Stirling and pulse tube refrigerator. A brief explanation of its predecessor, the Stirling-cycle engine along with the inception of the PTR will be followed by its subsequent development and component modifications.

In 1816, Robert Stirling patented his Stirling engine which was used as a prime mover [Organ (1997, [22])]. This closed-cycle, single-phase device was put to use in low power applications such as a water pump as a safer alternative to steam engines. It operated from any input heat source, but required large temperature differences between its thermal source and sink for efficient performance. As the development of steam engines took over the competition, the Stirling cycle would take a back seat to the more powerful and increasingly safer steam cycles. In 1834, John Herschel suggested the engine could be used as a refrigerator, but it was not until 30 years later that Alexander Kirk put this concept into practice [Radebaugh (1999, [24])].

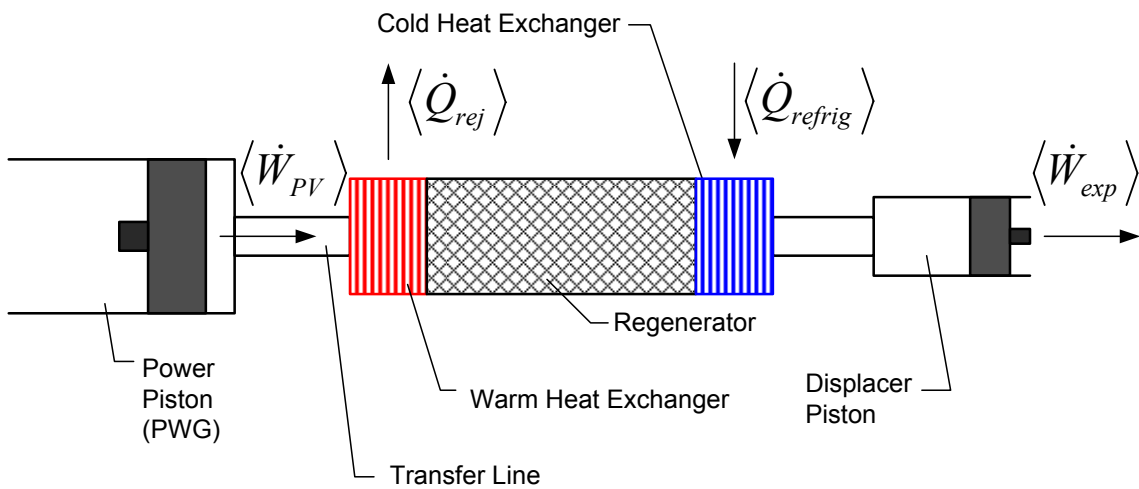


**Figure 1.5: Stirling expander diagram**

The simple Stirling system (Figure 1.5) is a configuration of piston cylinders and heat exchangers designed to provide displacement work by use of controlled heat transfer or refrigeration through gas expansion and compression. It consists of a power piston or compressor, a displacer piston, regenerator and cold and warm heat exchangers. Transfer lines connect the piston assemblies to their associated heat exchangers.

The oscillating pressures and flows produced by the compressor causes cyclic changes at point locations within the system. A different branch of thermodynamics known as thermoacoustics would be employed to describe the physical processes. Using principles of acoustics as well as laws of thermodynamics, thermoacoustics provides a fundamental understanding of these time-varying phenomena associated with the Stirling cycle and other oscillatory thermal systems.

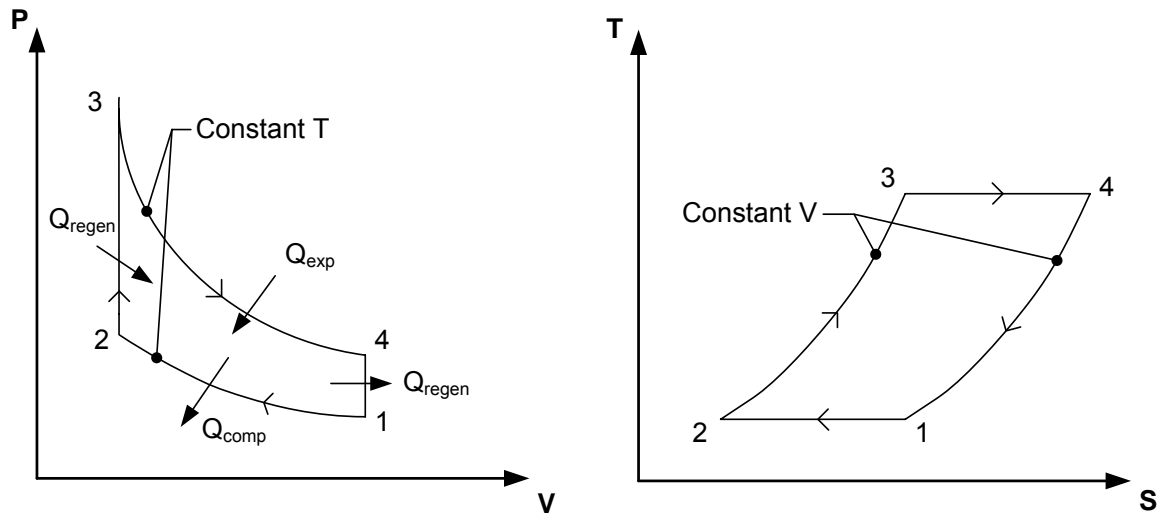


**Figure 1.6: Ideal Stirling cycle diagrams**

The ideal Stirling cycle is described in the pressure-volume (P-V) and temperature-entropy (T-S) diagrams as seen in Figure 1.6. Each diagram describes the

state of the working fluid at four particular instances during each cycle. Heat is transferred to the fluid in the processes 2-3-4 while heat is transferred away from the fluid in processes 4-1-2. In the process from 3 to 4, fluid is isothermally expanded, absorbing heat from the desired refrigerated environment. Some of this heat is then stored within the regenerator through a constant-volume process (4-1). During the process from 1 to 2, the working fluid is isothermally compressed and rejects heat to its surroundings. The thermal energy stored through regeneration is internally absorbed by the fluid in another constant-volume process (2-3).

Since all heat is supplied and rejected isothermally, the efficiency of this ideal cycle equals that of a Carnot cycle operating between the same temperatures. A real Stirling cycle would contain efficiencies much less than Carnot due to non-isothermal expansion and compression as well as other inherent irreversibilities such as viscous dissipation. Research and development on Stirling refrigerators was slow until the mid 1940s, when a system utilizing helium as its working fluid was successfully used for air liquefaction.

More than a century after the Stirling engine was in practice, another similar regenerative cycle had its birth. In the mid 1960s at Syracuse University, researchers Gifford and Longworth discovered that when a metallic tube (or pulse/buffer tube), closed at one end and the other end was exposed to a pressure oscillation, would develop a warming effect at the closed end. Thermal interaction between the working fluid and the tube walls would result in a surface heating effect. Continued research at Syracuse University demonstrated that installing a thermal regenerator between the PWG and the

pulse tube achieved a cooling effect [Popescu et al. (2001, [23])]. This concept led to the creation of the basic pulse tube refrigerator (BPTR), as shown in Figure 1.7.

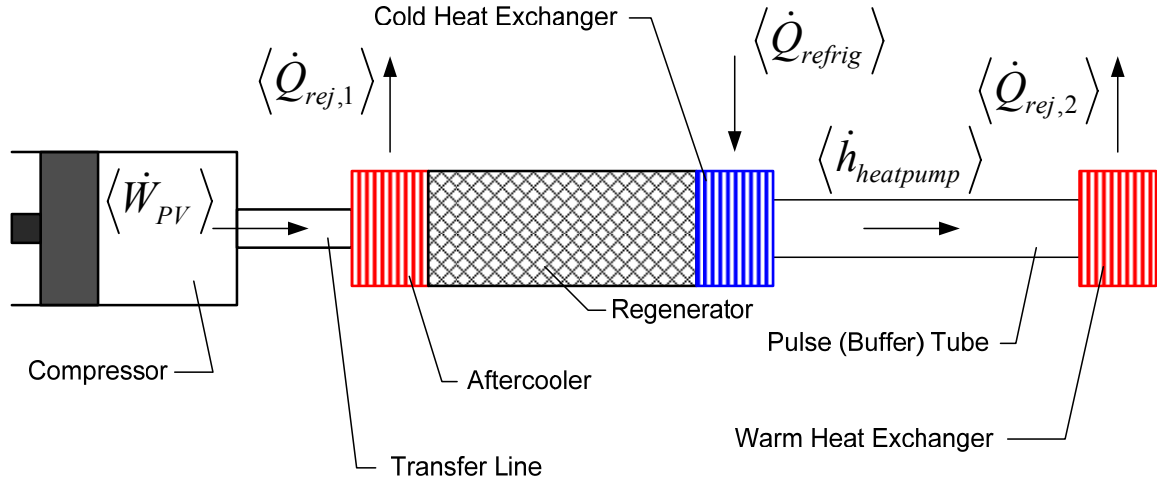


**Figure 1.7: Basic pulse tube refrigerator (BPTR) diagram**

Like the Stirling refrigerator, the BPTR is a simple linear system consisting of a compressor, regenerator and heat exchangers. The compressor generates an oscillating pressure wave and provides a work input to the system. Attached to the compressor through a transfer line (TX) is the first warm heat exchanger or aftercooler. Beyond that lies the regenerator which stores and rejects thermal energy in the course of one cycle. Adjacent to the regenerator is the cold heat exchanger (CHX) which provides the desired cooling load. The pulse tube (PT) is then adjoined with another warm heat exchanger (WHX) on its end. The BPTR functions much like the Stirling refrigerator, but contains one obvious change: the displacer piston in the expansion space was replaced by a compressible gas piston. The distinct advantage of the PTR over the Stirling refrigerator is the lack of moving parts at the cold end, resulting in increased reliability and operating life with decreased heat losses.

A simple energy balance through a control volume enveloping the BPTR shows energy inputs from the compressor work and heat from the refrigerated environment, while thermal energy is rejected to the surroundings through the two warm heat exchangers. These flows of energy, however, are unsteady and averaged over cycles. The BPTR functions through a compression and expansion operation where thermal boundary layers shuttle heat from the cold end of the pulse tube to the warm end. Heat transfers from the compressed fluid to the solid structure and at steady state conditions gas temperature profiles follow that of the tube wall. Ultimately, temperature gradients within the tube wall limited the BPTR performance and modifications had to be made to readily obtain cryogenic temperatures.

Although the BPTR was low in Carnot efficiency, it was recognized that the cooling power varied with the phase shift of pressure waves at the input of the pulse tube and those reflected by the closed end of the pulse tube. A multitude of ideas have been introduced to optimize this phase shift and maximize the enthalpy flow through the pulse tube. In the last several decades, adjustments to the BPTR and other such cryocoolers have led to improvements in overall system performance. A few of these evolutions are summarized in Table 1.1.

**Table 1.1: PTR developmental milestones**

1984	Mikulín et al.	Orifice Pulse Tube Refrigerator (OPTR) – placed orifice inside pulse tube to achieved temperature of 105 K.
1985	Radebaugh et al.	Needle valve placed outside pulse tube to achieved temperature of 60 K.
1990	Zhu, Wu & Chen	Double Inlet Orifice Pulse Tube Refrigerator (DIOPTR) - introduced a bypass channel connecting the compressor and warm end of the pulse tube to reduce regenerator losses.
1996	Zhu et al.	Inertance Tube Pulse Tube Refrigerator (ITPTR) – long tube replaced the orifice as the phase shifting mechanism.
1997	Olson & Swift	Tapered pulse tube was utilized to eliminate acoustical streaming in OPTRs.
2007	Garaway & Grossman	Miniature reservoir-less ITPTR (RLITPTR) is designed and tested, reaching a temperature of 146 K.

An ideal pulse-tube cycle does not exist as there are no well defined stages in which to characterize the state of the working fluid other than pressure. With no sequence of ideal gas processes, the conventional pressure-volume and temperature-entropy diagrams cannot be constructed. The pulse tube cooling effect relies on unsteady behavior and if fluid processes were steady and ideal, the device would fail to function [Organ, (1992, [22])].

### **1.3 The Modern Pulse Tube Refrigerator**

Modern PTR designs often utilize an orifice along with a reservoir volume to achieve proper phasing. However, this sharp contraction remains a large source of irreversibility so an inertance tube can be utilized in place of the orifice leading to increased efficiencies. PTR systems can even achieve compliance through an inertance tube without the aid of a surge volume, drastically reducing overall system volume by coiling the tube into a tight package. Unlike the BPTR, these systems do not rely on heat

transfer with the solid structure which can actually degrade its performance. Proper operation of individual components is essential for system integration.

The pulse tube operates by transferring enthalpy in an oscillating system across a temperature gradient while minimizing hydrodynamic losses and entropy generation. Like the AC power transmission's association between voltage and current, the magnitude of this hydrodynamic flow work is dependent upon the phase angle between the volumetric flow rate and dynamic pressure. Because of this harmonic relationship enthalpy flow is non-uniform throughout the pulse tube and must be time-averaged. The optimal case involves flow at the cold end to lag the pressure while the flow at the warm end of the pulse tube leads the pressure. Gas displacements within the tube must be small to effectively insulate the two ends and the pulse tube shell must minimize axial conduction. Mitigation of turbulence and acoustic streaming are also essential for effective operation.

The regenerator is fraught with many design challenges and optimal performance is a balance of several conditions. Typical regenerators utilize stacks of steel wire mesh screens or metal beads housed within a thin-walled frame. Recent developments shows that the application of multilayer regenerators comprised of several materials can take advantage of temperature dependent thermal properties [Radebaugh and Gully (2008, [25])]. Regenerator structure must provide a large heat capacity for thermal storage and the necessary surface area for optimal heat transfer between the working fluid and solid matrix. This rate of heat transfer is dependent on many factors including operating frequency, pore size and charge pressure. At steady state, one end of the regenerator may be at ambient temperatures while the other end is at cryogenic temperatures. As a result,

the regenerator and its housing must also minimize axial conduction across large temperature gradients and reduce hydrodynamic impedance or pressure drop within its porous media.

The heat exchangers function by transferring thermal energy between the working fluid and external environment. Highly conductive materials such as copper alloys are employed in the exchanger matrix and housing to maximize radial conduction. Heat exchangers also act as flow straighteners to produce a plug-flow regime within the pulse tube. Like the regenerator, they are usually composed of wire mesh bundles; however, there is an increased interest for application of MEMS based structures. Desired cooling loads are adjoined to the cold head via a thermal bus.

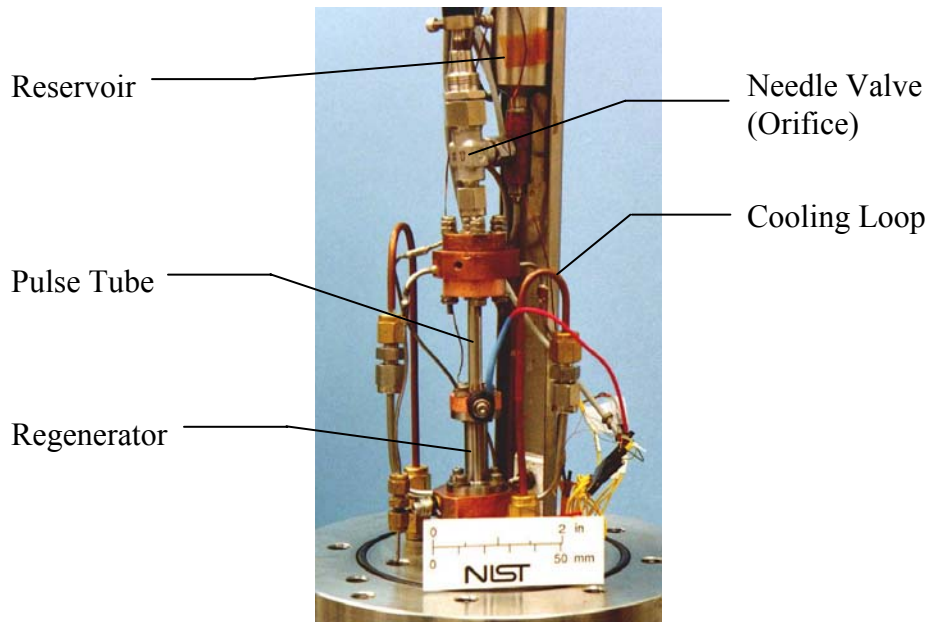


**Figure 1.8: 120 Hz miniature PTR experimental system (NIST)**

In an age of microelectronics, the demand for compact, low-temperature cryocoolers is ever increasing. In the last decade, there has been a considerable effort to

increase cryocooler performance while minimizing parameters such as mass, volume, cost and input power. Miniaturization of cryocoolers has been an ongoing process since 1999; however, the commercial availability of such systems has yet to be seen. Understanding the loss mechanisms of such small-scale devices leads to several design principles essential for miniature PTRs: high operating frequencies at small tidal displacements, a regenerator matrix with small hydraulic diameters and increased fill pressures [Garaway and Grossman (2008, [11])]. Thermal management of temperature gradients over decreased length scales is the ultimate performance limitation.

#### **1.4 Project Motivation and Rationale**

Multiple design tools have been established to accurately capture the working processes governing PTRs. Recent successful CFD models [Cha (2007, [1]), Cha et al. (2006, [2]), Conrad (2008, [9])] of cryocooler systems have shown that such models can provide very useful performance predictions for cryocoolers. For miniature cryocoolers, CFD modeling is likely the best technique available as models developed for larger systems may not accurately represent phenomena which become important as the device scale is reduced. Accurate CFD modeling of Stirling and pulse tube refrigerators requires realistic closure relations, particularly with respect to the hydrodynamic and thermal transport processes for the porous media which make up their heat exchangers and regenerators. Recent studies [Cha (2007, [1]), Clearman (2007, [6])] present useful experimental data and correlations for some common regenerator fillers; however, these fillers may not be suitable for use in miniature cryocoolers due to their relatively coarse structure. Instead, these cryocoolers will require porous material with considerably smaller characteristic pore sizes than those commonly used in larger scale devices.

It should be emphasized that without direct pore-level simulation, the macroscopic conservation equations which govern fluid flow through the porous media require empirical momentum closure parameters, and experimental data is needed for the development of these empirical correlations [Cha (2007, [1])]. These empirical correlations include the Darcy permeability and Forchheimer's inertial coefficient which are needed for the closure of macroscopic momentum conservation equations. Generally, the porous media that are encountered in cryocoolers are morphologically anisotropic, and thus the parameters which characterize them are anisotropic as well. Measurement of the hydrodynamic parameters in at least two dimensions is therefore preferred. Hydrodynamic parameters may also vary when these fillers are subjected to steady or periodic flows. Therefore resistance parameters were found for steady as well as steady – periodic or oscillatory flow conditions. The directional hydrodynamic flow resistance parameters are determined using experimental measurements of the fluid mass flow rate and the pressure drop across the porous media. By simulating the experimental test section using CFD, the viscous and inertial flow resistances of the porous region are iteratively adjusted until agreement is reached between simulated and experimental results.

This thesis describes the measurements of the hydrodynamic parameters of stacked discs of #635 stainless steel and #325 phosphor bronze wire mesh using a CFD – assisted methodology. These materials are among the finest commercially available structures suitable for use as miniature regenerator and heat exchanger fillers. Through experimental testing and the subsequent CFD matching process, unique parameters are determined for each sample. Measurements were made in the axial and radial directions

for both steady and oscillatory flow conditions. Higher frequency operation is preferred for miniature cryocoolers; therefore a frequency range between 50 and 200 Hz was investigated for the oscillatory flow cases. Increased charge pressure and operating frequencies are selected because they are expected to apply to miniature cryocoolers.

An extension of this flow parameterization technique investigated the effect of average pressure on the porous media hydrodynamic closure relations applicable to steady axial flow. Four regenerator fillers materials were used in this study include stacked screens of #325 and #400 stainless steel mesh, screens of stainless steel #400 mesh stacked and sintered together and a stainless steel metal foam.

This method of formulating hydrodynamic characteristics under periodic flow conditions, namely the quantification of hydrodynamic parameters that would lead to agreement between experimental data and the predictions of a detailed, numerical simulation system, was proposed by Harvey (2003, [12]). Cha (2007, [1]) further developed this process through the incorporation of detailed, two-dimensional CFD analyses. The experimental investigations of Harvey and Cha, furthermore, were follow-ups to an earlier study by Kirkconnell (1995, [16]). Although this method predominately focuses on stacks of wire mesh screens, it is also applicable to other such porous structures used for cryocoolers including materials created through micro fabrication techniques.

## 2 THEORY

### 2.1 Fundamental Analysis

CFD is a useful tool to analyze multi-dimensional flow fields with complex geometry where the smallest flow features are orders of magnitude larger than the molecular mean free path. CFD code rigorously solves the governing conservation equations of mass, momentum and energy for discrete cells. These volume average equations not only account for spatial variations in fluid properties but also command temporal variations for unsteady flow. By applying boundary conditions to the system, numerical solutions are calculated to fully characterize the flow field.

A fundamental understanding of fluid mechanics leads to differential equations describing infinitesimal control volumes. Governing equations state that mass cannot be created nor destroyed and a system's momentum and energy must be conserved. Equations (2-1) and (2-2) display the standard fluid mass and momentum conservation equations in vector form.

$$\frac{\partial \rho}{\partial t} + \nabla \cdot (\rho \bar{v}) = 0 \quad \text{Eq. (2-1)}$$

$$\frac{\partial}{\partial t} (\rho \bar{v}) + \nabla \cdot (\rho \bar{v} \bar{v}) = -\nabla P + \nabla \cdot (\bar{\tau}) + \bar{F}_{bf} \quad \text{Eq. (2-2)}$$

The vector  $\bar{v}$  represents the fluid's local instantaneous, physical velocity within the domain. Fluid density and viscosity are represented as  $\rho$  and  $\mu$ , and thermodynamic absolute pressure is shown with  $P$ . The same equations can also represent time, volume or doubly averaged conservation equations; provided that care is taken with respect to the correct representation of properties and closure relations. The left hand side of the Navier-Stokes (Eq. (2-2)) equation represents the Eulerian viewpoint of the fluid including the local and convective acceleration while the right hand side depicts the mechanisms driving the motion of the fluid. The sources or sinks of momentum include pressure gradients, surface stresses and an arbitrary volumetric body force. This body force is often used when simulating external forces created by gravitational, magnetic and electrical fields. Most cryocooler simulations do not include any body forces or gravity for two reasons. First, the inclusion of a body force would constrain orientation and application. Second, in most cases surface forces are dominant and the body force has an unimportant effect. Parametric studies that examine the effect of orientation and gravity induced flows have been reported [Ross and Johnson, (2004, [27])].

The viscous stress tensor ( $\bar{\tau}$ ) determines the fluid's behavior and is viewed in Eq. (2-3). The fluid is assumed Newtonian and Stoke's assumption applies damping only for compression and expansion.

$$\bar{\tau} = \mu(\nabla\bar{v} + \nabla\bar{v}^T) - \mu\frac{2}{3}\nabla\cdot\bar{v}\bar{I} \quad \text{Eq. (2-3)}$$

Since the working fluid in cryocoolers is a gas (usually He) at parameter ranges where the ideal gas assumption is reasonable, fluid density is solved through the application of

the ideal gas equation of state (Eq. (2-4)) with  $\bar{R}$  representing the specific gas constant. Because all experimentation discussed in this thesis is performed at ambient conditions, temperature deviations remain small; however, there is a large variation of pressure. As a result, the energy conservation equation (Eq. (2-5)) must account for temperature and fluid compressibility effects.

$$\rho = \frac{P}{RT} \quad \text{Eq. (2-4)}$$

$$\frac{\partial}{\partial t}(\rho e) + \nabla \cdot (\bar{v}(\rho e + P)) - \nabla \cdot (k \nabla T + \bar{\tau} \cdot \bar{v}) = 0 \quad \text{Eq. (2-5)}$$

$$e = h - \frac{P}{\rho} + \frac{v^2}{2} \quad \text{Eq. (2-6)}$$

Equation (2-6) displays the total specific energy ( $e$ ) of the fluid including the internal and kinetic energies (with units of  $J/kg$  in the standard SI unit system). Specific enthalpy and velocity magnitudes are displayed by  $h$  and  $v$ , respectively.

## 2.2 Porous Media Theory

Complete analysis of the fluid-solid interaction through porous media can be obtained only by direct pore level simulation [Cha (2007, [1])]; a method which is computationally intensive and time consuming, and is impractical for design and parametric calculations. Navier-Stokes and energy equations within the porous structure

can be volume averaged, leading to conservation equations which capture the macroscopic fluid behavior in porous media without solving for the detailed fluid motion at the microscopic scale. These equations utilize material porosity (Eq. (2-7)) or the ratio of open or void volume to the total occupied volume of the structure. Calculation of sample porosity is possible through measurement of the volume of the specimen housing, aggregate mass and average sample density.

$$\varepsilon = \frac{V_{void}}{V_{total}} = 1 - \frac{V_{sol}}{V_{total}} \quad \text{Eq. (2-7)}$$

The porosity, represented by  $\varepsilon$ , is a scalar quantity bound between zero and one. A large porosity represents a near open channel while smaller fractions indicate a constricted flow. The solid material volume can be found by  $1 - \varepsilon$ . Volume and time double-averaging of the local-instantaneous conservation equations and the application of the appropriate closure relations for porous media, allows the governing equations to be recast into Eqs. (2-9) ~ (2-11), restricting the fluid behavior to only the void space of the porous structure. The energy equation must also be modified to describe the interaction between the working fluid and the solid matrix. If the porous medium has uniformly repeated geometry then lattice parameters may be used to symbolize a unit cell. This concept, however, cannot be utilized in the case of random orientation.

$$\frac{\partial}{\partial t}(\varepsilon\rho) + \nabla \cdot (\varepsilon\rho\bar{v}) = 0 \quad \text{Eq. (2-9)}$$

$$\frac{\partial}{\partial t}(\varepsilon\rho\bar{v}) + \nabla \cdot (\varepsilon\rho\bar{v}\bar{v}) = -\varepsilon\nabla P + \nabla \cdot (\varepsilon\bar{\tau}) + \varepsilon\bar{F}_{bf} - \mu\bar{D} \cdot \bar{v} - \frac{\bar{C}\rho}{2} \cdot |\bar{v}|\bar{v} \quad \text{Eq. (2-10)}$$

Equation (2-10) shows the modified momentum conservation equation with viscous and inertial resistance coefficient tensors,  $\bar{D}$  and  $\bar{C}$  (having units of  $m^{-2}$  and  $m^{-1}$  in the standard SI unit system, respectfully). These tensors are hydrodynamic loss mechanisms and are often determined through empirical relationships. Resistance parameters can be obtained from direct simulation at pore-level (at least for laminar flow); however, specification of these parameters is not generally feasible because porous structures often have irregular and complicated pore geometries. The viscous resistance is proportional to the velocity while the inertial resistance is relative to the square of the velocity. At low flow rates the viscous term dominates and the inertial term can be neglected. Conversely, the inertial term will prevail at large velocities as it has a squared relationship. It has been suggested that the viscous and inertial resistance coefficients are intrinsic to the geometry of the porous structure and are independent of the nature of the flow [Nield and Bejan (1999, [20])]; however, new research shows variation of these coefficients with temperature and oscillation frequency. If lattice parameters can be defined, mathematical correlations may exist for these resistances.

Hsu (2005, [13]) has also confirmed the existence of another such resistance term proportional to  $\bar{v}\sqrt{\bar{v}}$  which accounts for viscous boundary layer effects in transitions regimes. This present investigation follows common practice and omits the latter term.

The energy equation can be represented as,

$$\begin{aligned} \frac{\partial}{\partial t}(\varepsilon\rho_f e_f + (1-\varepsilon)\rho_{sol}e_{sol}) + \nabla \cdot (\varepsilon\bar{v}(\rho_f e_f + P)) \\ - \nabla \cdot ((\varepsilon k_f + (1-\varepsilon)k_{sol})\nabla T + \bar{\tau} \cdot \varepsilon\bar{v}) = 0 \end{aligned} \quad \text{Eq. (2-11)}$$

The energy equation (Eq. (2-11)) for a porous medium encompasses both the fluid and solid matrix using subscripts *f* and *sol* to denote the fluid and solid structure. Local thermal equilibrium is assumed between the different phases; however, this assumption fails at high velocities and separate energy equations for the distinct phases must be solved separately [Nield and Bejan (1999, [20])].

It is important to note that conservation equations can be written by presenting the fluid velocity as being superficial or physical. Superficial or Darcy velocity describes the flow outside the porous zone while the physical velocity depicts the fluid motion within the porous matrix. Eq. (2-12) is sometimes referred to as the Dupuit-Forchheimer relationship, where  $\bar{u}$  and  $\bar{v}$  symbolize the superficial and physical velocities, respectfully. It is obvious through conservation of mass flow that the physical velocity will always be larger than the superficial velocity. For an open channel, the physical and superficial velocities are equal.

$$\bar{u} = \varepsilon\bar{v} \quad \text{Eq. (2-12)}$$

Utilizing the superficial velocity, Eq. (2-10) can be rewritten in the following form:

$$\frac{1}{\varepsilon} \left[ \frac{\partial}{\partial t} (\rho \bar{u}) + \nabla \cdot \left( \rho \frac{\bar{u}\bar{u}}{\varepsilon} \right) \right] = -\nabla P + \nabla \cdot \left( \overline{\tau} \right) + \bar{F}_{bf} - \frac{\mu \bar{D}}{\varepsilon^2} \cdot \bar{u} - \frac{\bar{C}\rho}{2\varepsilon^3} \cdot |\bar{u}| \bar{u} \quad \text{Eq. (2-13)}$$

The viscous stress tensor is now  $\overline{\tau}$  signifying that it is with respect to the superficial velocity.

A channel's average superficial velocity ( $\bar{u}_{avg}$ ) is also related to the internal mass flow rate through Eq. (2-14), where  $A$  is the cross sectional area perpendicular to the flow.

$$\bar{u}_{avg} = \frac{\dot{m}}{\rho A} \quad \text{Eq. (2-14)}$$

If the momentum conservation equation is exhibited in a cylindrical coordinate system with the assumption of symmetry along its longitudinal axis, axial and radial directions of the modified momentum equation can be displayed as Eq. (2-15) and Eq. (2-16), respectfully. Directional viscous and inertial resistances are designated for each orthogonal basis. The simplifying conjecture still produces an angular velocity ( $v_\theta$ ) component; however, it equals zero for the two-dimensional axisymmetric case.

$$\begin{aligned} & \frac{\partial}{\partial t} (\varepsilon \rho v_x) + \frac{1}{r} \frac{\partial}{\partial x} (r \varepsilon \rho v_x v_x) + \frac{1}{r} \frac{\partial}{\partial r} (r \varepsilon \rho v_x v_r) + \varepsilon \frac{\partial P}{\partial x} + \\ & \frac{1}{r} \frac{\partial}{\partial x} \left\{ \varepsilon r \mu \left( 2 \frac{\partial v_x}{\partial x} - \frac{2}{3} \left( \frac{\partial v_x}{\partial x} + \frac{\partial v_r}{\partial r} + \frac{v_r}{r} \right) \right) \right\} + \frac{1}{r} \frac{\partial}{\partial r} \left\{ \varepsilon r \mu \left( \frac{\partial v_x}{\partial r} - \frac{\partial v_r}{\partial x} \right) \right\} \\ & + \mu D_x v_x + \frac{C_x \rho}{2} |\bar{v}| v_x = 0 \end{aligned} \quad \text{Eq. (2-15)}$$

$$\begin{aligned}
& \frac{\partial}{\partial t}(\varepsilon\rho v_r) + \frac{1}{r} \frac{\partial}{\partial x}(r\varepsilon\rho v_x v_r) + \frac{1}{r} \frac{\partial}{\partial r}(r\varepsilon\rho v_r v_r) + \varepsilon \frac{\partial P}{\partial r} + \\
& \frac{1}{r} \frac{\partial}{\partial x} \left\{ \varepsilon r \mu \left( \frac{\partial v_r}{\partial x} + \frac{\partial v_x}{\partial r} \right) \right\} + \frac{1}{r} \frac{\partial}{\partial r} \left\{ \varepsilon r \mu \left( 2 \frac{\partial v_r}{\partial r} - \frac{2}{3} \left( \frac{\partial v_x}{\partial x} + \frac{\partial v_r}{\partial r} + \frac{v_r}{r} \right) \right) \right\} - \quad \text{Eq. (2-16)} \\
& 2\varepsilon\mu \frac{v_r}{r^2} + \frac{2}{3} \frac{\varepsilon\mu}{r} \left( \frac{\partial v_x}{\partial x} + \frac{\partial v_r}{\partial r} + \frac{v_r}{r} \right) + \varepsilon\rho \frac{v_\theta^2}{r} + \mu D_r v_r + \frac{C_r \rho}{2} |\bar{v}| v_r = 0
\end{aligned}$$

By ignoring the convective acceleration, viscous dissipation and external body forces, Eqs. (2-15) and (2-16) yield analytical solutions for pressure drop in steady axial and radial flow.

$$\varepsilon \nabla P = - \left[ \mu \bar{D} \cdot \bar{v} + \left( \frac{\bar{C}_\rho}{2} \cdot \bar{v} \right) |\bar{v}| \right] \quad \text{Eq. (2-17)}$$

Eq. (2-17) shows the momentum equation in vector form; neglecting convective (spatial) acceleration, viscous dissipation and external body forces. This equation is adequate for steady flows without significant compressibility effects. The two terms on the right hand side, which together represent the total drag force imposed by the porous medium, can then be used for the definition of the Darcy permeability and Forchheimer's inertial coefficient. Equation (2-18) relates the directional viscous and inertial resistances to the directional Darcy permeability and Forchheimer's inertial coefficient. Index notation allows the subscript  $i$  to represent each coordinate basis.

$$-\left[ \frac{\mu D_i \bar{v}_i}{\varepsilon} + \frac{C_i \rho}{2\varepsilon} |\bar{v}_i| \bar{v}_i \right] = -\left[ \frac{\mu \varepsilon^2}{K_i} \bar{v}_i + \frac{c_{f_i} \varepsilon^3 \rho}{\sqrt{K_i}} |\bar{v}_i| \bar{v}_i \right] \quad \text{Eq. (2-18)}$$

Equations (2-19) and (2-20) explicitly displays the relationship between the directional viscous resistance coefficient and the Darcy permeability, as well as the directional inertial resistance coefficient and Forchheimer's inertial coefficient, respectfully, when the global coordinates are the principle coordinates of the porous structure.

$$K_i = \frac{\varepsilon^2}{D_i} \quad \text{Eq. (2-19)}$$

$$c_{f_i} = \frac{C_i \sqrt{K_i}}{2\varepsilon^3} \quad \text{Eq. (2-20)}$$

Assuming isotropic flow resistances, the viscous and inertial resistance coefficient tensors become scalar quantities. This assumption, although strictly speaking is often unrealistic, is justifiable if the flow within the porous structure is predominantly one-dimensional (and therefore the lateral flow phenomena are of little consequence) or the lattice of the porous structure is approximately isotropic.

Fluent CFD code [Fluent (2003, [10])] solves the momentum equation for porous zones using either the physical or superficial velocity notation. The code has user inputs for the viscous and inertial resistance coefficients of their respective principle direction.

A complimentary form of accounting for hydrodynamic resistances lies with the dimensionless friction factor,  $f$ . Equation (2-21) illustrates the Darcy-Weisbach equation

which is commonly used to determine pressure losses in one-dimensional channel flow with constant cross sectional area. The hydraulic diameter of the channel is denoted,  $d$  and scalar notation is used to express the uni-axial direction of flow. The superficial length of the porous region is indicated as  $l$ .

$$\frac{\Delta P}{l} = f \frac{1}{d} \frac{\rho u^2}{2} \quad \text{Eq. (2-21)}$$

There are many ways to represent head loss through porous media by using either the physical or superficial velocities and coupling that with an appropriate characteristic length. Two forms utilizing the superficial velocity will be developed.

By applying Eq. (2-21) to a change in pressure across a porous structure an expression can be derived for the relationship between the Darcy friction factor and the viscous and inertial resistances.

$$\frac{\Delta P}{l} = \frac{1}{2} f \sqrt{D} \rho |u| u = \mu D u + \frac{C \rho}{2} |u| u \quad \text{Eq. (2-22)}$$

Using the magnitude of the superficial velocity as well as the fluid density and viscosity, a Reynolds number can be formed based on the inverse square root of the directional viscous resistance coefficient.

$$\text{Re}_D = \frac{\rho |u|}{\mu \sqrt{D}} \quad \text{Eq. (2-23)}$$

By dividing through by the common velocity component, substituting  $Re_D$  and completing some slight rearrangement Eq. (2-22) can be recast as:

$$f_D = \frac{2}{Re_D} + \frac{C}{\sqrt{D}} \quad \text{Eq. (2-24)}$$

It is again seen from this expression for the Darcy friction factor that at small velocities or low Reynold's numbers that the viscous term is dominant when compared to the constant inertial term. As velocity increases the viscous term's contribution diminishes and at very large velocities the viscous term approaches zero while the friction factor approaches a constant value. A particular application may be limited to a particular range of Reynolds numbers.

Another such correlation is established with a Reynold's number based upon the square root of the Darcy permeability. Eq. (2-25) and Eq. (2-26) illustrate this formulation.

$$Re_K = \frac{\rho |u| \sqrt{K}}{\mu} \quad \text{Eq. (2-25)}$$

$$f_K = \frac{2}{Re_K} + 2c_f \quad \text{Eq. (2-26)}$$

The style found in Eqs. (2-25) and (2-26) is commonly used to characterize the flow regime within a porous medium; however both forms of friction factors will be applied in this thesis. It should be noted that there are other types of friction factors based upon various length scales and caution must be exercised when comparing them.

Up until this point all of the analysis and discussion has focused on the steady flow regime; however, regenerative cryocoolers function under steady-periodic flow conditions. A structure's viscous and inertial resistances, when subjected to steady flow, may be very different from those associated with oscillatory flows. A recent study by Hsu et al. (1999, [14]) measured pressure and velocity correlations for porous media under oscillatory and steady flows and found that low frequency flows replicate those measured in steady flow. However, resistances determined at higher frequencies tend to deviate from steady flow results rather significantly.

Due to the complexity of the experimental setup, resistances are sometimes measured at room conditions and then applied to models in which the structure is exposed to a range of temperatures; some of which are cryogenic. However, some recent investigations [Nam and Jeong (2006, [18]), Shen and Ju (2008, [29])] claim that resistances obtained at ambient temperatures may be very different than those gathered at cryogenic temperatures.

Much of these phenomena are not well understood and measurement of hydrodynamic resistances remains acute to a particular application and range of experimental parameters.

### **3 EXPERIMENTAL METHODOLOGY**

#### **3.1 General Remarks**

Experimental tests were performed to determine the hydrodynamic resistances of stacked screens of #635 stainless steel mesh and #325 phosphor bronze mesh in the axial and radial directions under steady and oscillatory flows. Consequently, each direction and flow regime utilized a unique test section, instrumentation and methodology. The experimental test setups provide measurements of pressure and mass flow rate which offer empirical relationships to determine hydrodynamic resistance parameters of the investigated materials.

All test setups shared some common attributes. Research grade helium with a nominal purity of 99.9999% was employed in all test setups as the working fluid. Test runs were only performed after strict assurance of a hermetically sealed setup. Although the mesh fillers were not subjected to the rigorous cleaning processes that a standard cryocooler assembly would undergo, all experimental setups were purged of air and particulates. Each test was performed at room temperature (27°C) where the test section containing the porous sample remained in thermal equilibrium. Slight rises in temperature and accordingly increases in pressures were observed in oscillatory flow cases as a result of viscous heating effects.

Wire cloth material was supplied from TWP Inc. and test samples were machined by Virtual AeroSurface Technologies using a punching operation. This manufacturing technique was labor intensive and inefficient; however, it produced clean edges unlike

the more efficient wire electric discharge machining processes. Sample #635 stainless steel and #325 phosphor bronze screen discs used for testing are displayed in Figure 3.1.

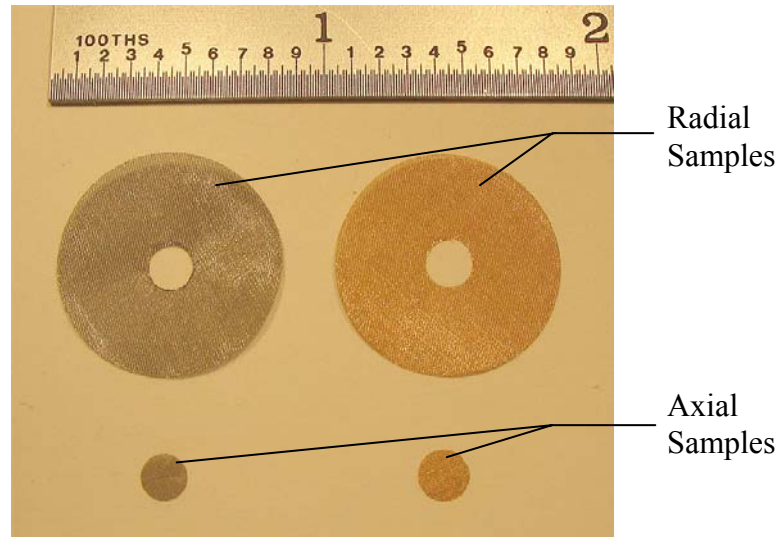


**Figure 3.1: Mesh filler sample cuts**

Each mesh utilizes a plain square weave pattern where perpendicular wires are woven into a simple over and under configuration as seen in Figure 3.2. Mesh screens are characterized the number of strands of wires it has parallel per inch within its matrix; square weave patterns have the same number in each direction. A random orientation was developed when stacking screens and a high packing density aimed to mimic industry standards for regenerator and heat exchanger applications.

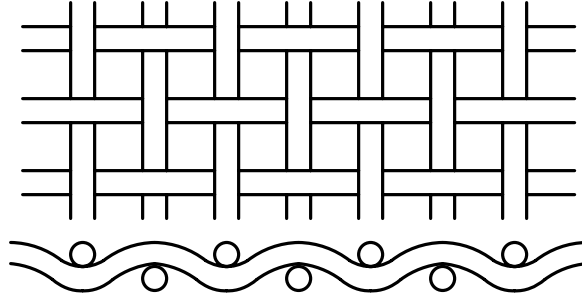


**Figure 3.2: Plain square weave**

Porous materials have several intrinsic parameters including pore size, tortuosity and porosity. Pore size is the average unit length of an open channel perpendicular to which fluid will flow. In the case of mesh screens, it is characterized by the hydraulic diameter created by an opening within its screen. Tortuosity is the average total distance a fluid particle will traverse upon entering and exiting a porous region and is commonly larger than the superficial length of the porous zone. Tortuosity is extremely difficult to measure for structures with irregular patterns and is beyond the scope of this investigation.

Porosity, as previously mentioned, is a ratio of the void space to the total space within a porous structure and is a volume-averaged measure of fluid within the material. Sample porosity is calculated for axial and radial flow samples using Eq. (3-1) and Eq. (3-2). Bulk densities of  $8,030 \text{ kg/m}^3$  and  $8,860 \text{ kg/m}^3$  were utilized for stainless steel and phosphor bronze constituent samples, respectively. Near equal porosities for each material's axial and radial flow directions are desired to fully characterize the resistance parameters of the porous structure.

$$\varepsilon_{cyl} = 1 - \frac{V_{sol}}{V_{tot}} = 1 - \frac{4m_{sample} / \rho_{sample}}{\pi l_{cyl} d_{od}^2} \quad \text{Eq. (3-1)}$$

$$\varepsilon_{annular} = 1 - \frac{V_{sol}}{V_{tot}} = 1 - \frac{4m_{sample}/\rho_{sample}}{\pi l_{annular} (d_{od}^2 - d_{in}^2)} \quad \text{Eq. (3-2)}$$

**Table 3.1: Steady and oscillatory flow test sample details**

Porous Media	Sample Geometry			Mesh Geometry			Measured Porosity [-]
	I.D. [mm]	O.D. [mm]	Length [mm]	Wire Dia [micron]	Thickness [micron]	Pore Size [micron]	
Axial Samples							
#325 Phosphor Bronze	N/A	4.0	12.7	35.6	71.1	43	0.6738
#635 Stainless Steel	N/A	4.0	12.7	20.3	40.6	25	0.6312
Radial Samples							
#325 Phosphor Bronze	4.0	20.0	3.4	35.6	71.1	43	0.6702
#635 Stainless Steel	4.0	20.0	6.1	20.3	40.6	25	0.6304

Important characteristics of the porous samples tested are summarized in Table 3.1. Please note that experimental setups for each flow direction employed the same porous samples; meaning both the steady and oscillatory axial flow parameterization tests employed the same axial test samples (same idea pertains to radial testing).

The four specific experimental setups and procedures used for each flow direction and regime are described in detail.

### 3.2 Steady Axial Flow

The steady axial flow experimental apparatus consisted of a helium supply tank and pressure regulator, two Paine Electronics Series 210-10 static pressure transducers, a Sierra Instruments 820 Series Top-Trak mass flow meter, a specially designed test section containing the porous sample and the associated piping and Swagelok fittings and valves. Pressure signals were amplified and calibrated through an Omega DMD-465WB signal conditioner. The static pressure transducers and mass flow meter each have an

accuracy of  $\pm 0.35\%$  and  $\pm 1.5\%$  of full scale, respectively. Pressure and mass flow rate measurements were read as analogue voltage signals via handheld digital multimeters (DMM). Each DMM used in the steady flow setups had a resolution of at least 0.01 Volts.

A linear calibration was applied to both of the static pressure transducers used in the steady flow experiments. The signal conditioners zeroed the reading at atmospheric pressure and the gain was set at 500 psig (3.55 MPa) to sync pressure measurements with a dial gage. The mass flow meter was calibrated at atmospheric conditions using helium gas.

Visual aids for the steady axial flow experimental setup are shown in Figure 3.3 through Figure 3.6. For complete dimensions of the steady axial flow experimental test setup please refer to Appendix D.1 for simulation vertices.

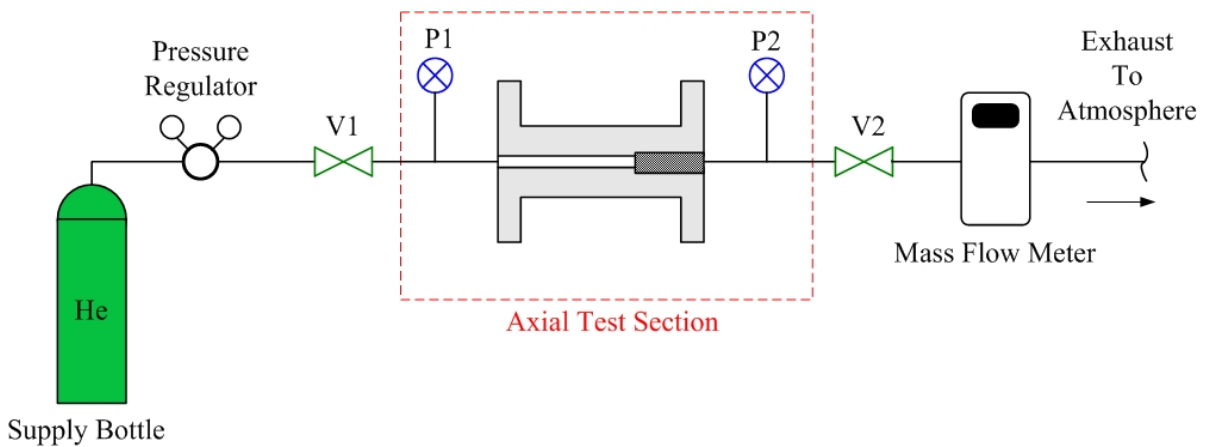


**Figure 3.3: Steady axial flow experimental setup diagram**

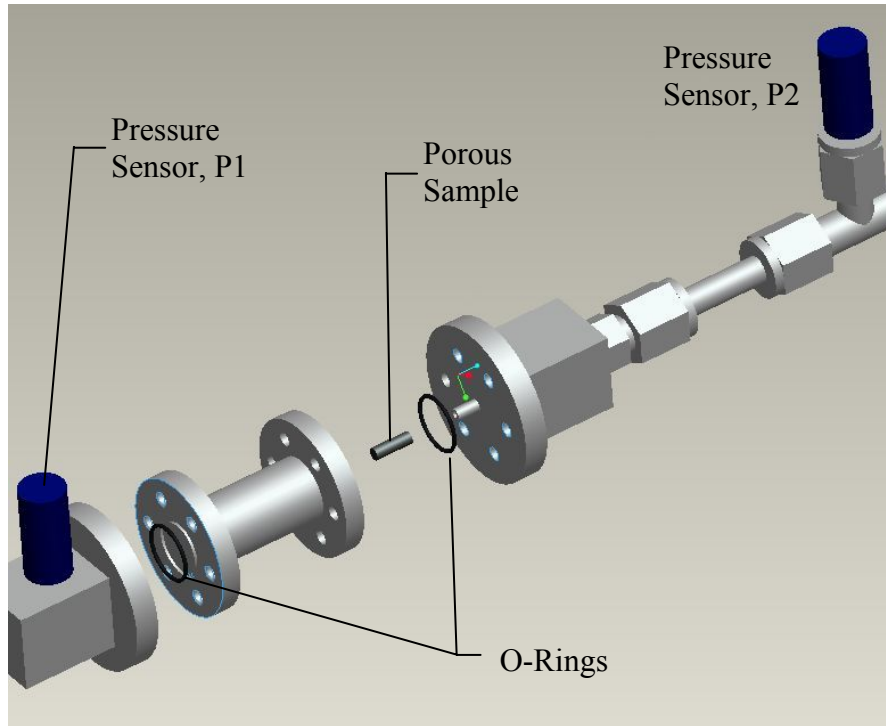


**Figure 3.4: Steady axial flow test section exploded CAD view**

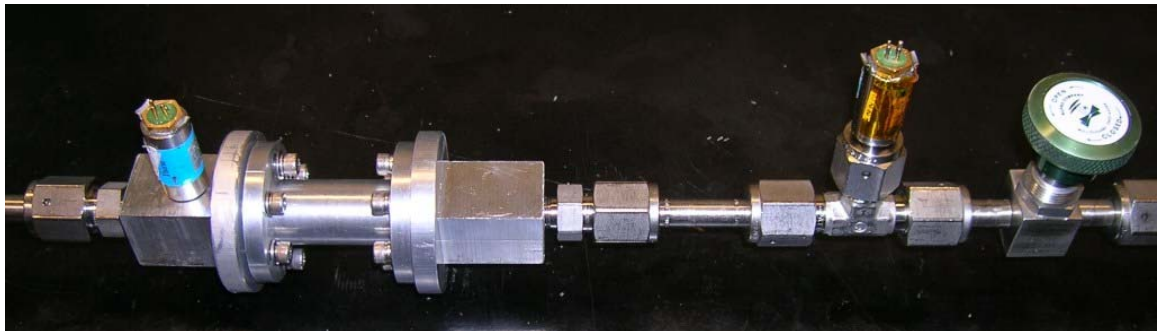


**Figure 3.5: Steady axial flow experimental setup photograph**

The axial flow test section which houses the porous media is a hollow aluminum cylinder with two inner diameters separated by a step change. A 2.007 mm (0.079 in) passage opens up to a 4.013 mm (0.158 in) diameter channel which contains the stacked discs. End pieces bolted onto flanges located on either side of the test section constrain the porous samples and provide a mount for one of the static pressure transducers.

Greased Viton o-rings provide a seal for each end piece junction. The test sample and housing were specifically designed with a large aspect ratio (axial length divided by diameter) of 3.175 to ensure that the flow had a predominant axial velocity component; and flow in the radial direction can be considered small. Each porous sample was fabricated with a strict tolerance to ensure negligible clearance between its circumference and the inside of the test section. A detailed view of the test section and its surrounding area is shown in Figure 3.6.

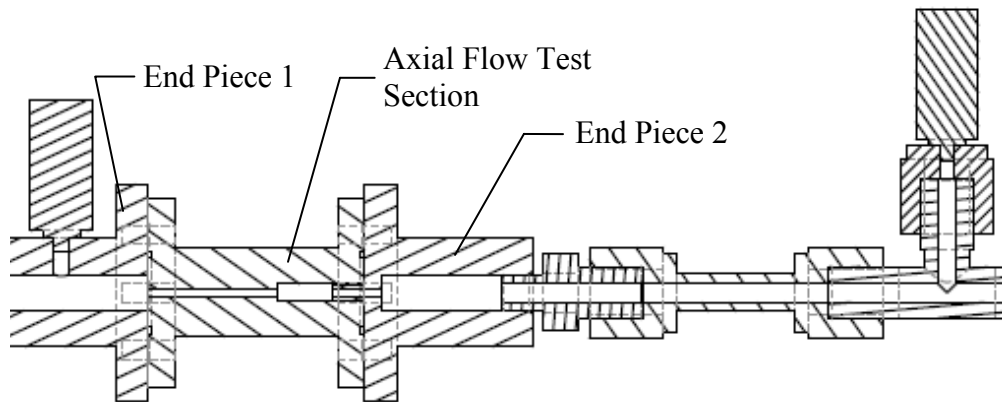


**Figure 3.6: Steady axial flow experimental setup detailed CAD view**

Valves, V1 and V2, and the static pressure transducers, P1 and P2, are respectively located upstream and downstream of the axial test section. During each steady flow test, helium flows from the charged bottle through the pressure regulator, past the valve V1 and into the test section. The fluid then leaves the test section through valve V2 and is straightened before it passes through the mass flow meter and is exhausted to the atmosphere. With valve V2 closed and valve V1 open, the system was charged to a pressure of 2.86 MPa (400 psig) as set by the regulator. Valve V2 was then modulated to offer a suitable range of mass flow rates between 0.0 and 1.5 g/s. Static

pressures P1 and P2 were recorded for each distinct flow rate. Experimental data for steady axial flow analysis is tabulated in Appendix A.1.

It should be noted that a single stage pressure regulator is used for all steady flow tests; offering little change in delivery pressure over a range of flow rates. However, single stage regulators exhibit a large variation in delivery pressure as the regulator's supply pressure decreases while the cylinder empties [Scott Specialty Gases (2008, [28])]. As a result, only test runs where there is significant bottle pressure were considered valid and used for analysis.

In order to prevent a large fluctuation in mean pressure throughout each sample run, the maximum allowable change in pressure across the test section was limited to 0.69 MPa (100 psi). For each test sample, pressure drops between static pressures P1 and P2 were then plotted against mass flow rate. In order to simplify the data analysis, axial flow experimental data for each filler material was curved fitted to a 5<sup>th</sup> order polynomial. Each curve fit was constrained with a zero intercept and would act as a guide for defining the boundary conditions to be used for CFD simulations.

An extension of this steady axial flow case investigates the effect of pressure on hydrodynamic parameters on four different sample filler materials. The study utilized a similar experimental setup with slight variations in test section geometry, however, the testing procedure and analysis was identical. Results for this particular test can be found in section 5.2. Please refer to Appendix E for experimental setup and test data.

### **3.3 Steady Radial Flow**

Equipment utilized in the steady radial flow experimental setup is identical to the steady axial flow test rig, with the exception of the porous test section, sample housing

and its associated fittings and sensor mounts. The system contains the same pressure transducers, mass flow meter, in-line signal amplifiers and measurements are read through digital multimeters. Visual references for the steady radial flow experimental setup are shown in Figure 3.7 through Figure 3.11. For complete dimensions of the steady radial flow experimental test setup, please refer to Appendix D.2 for simulation vertices.

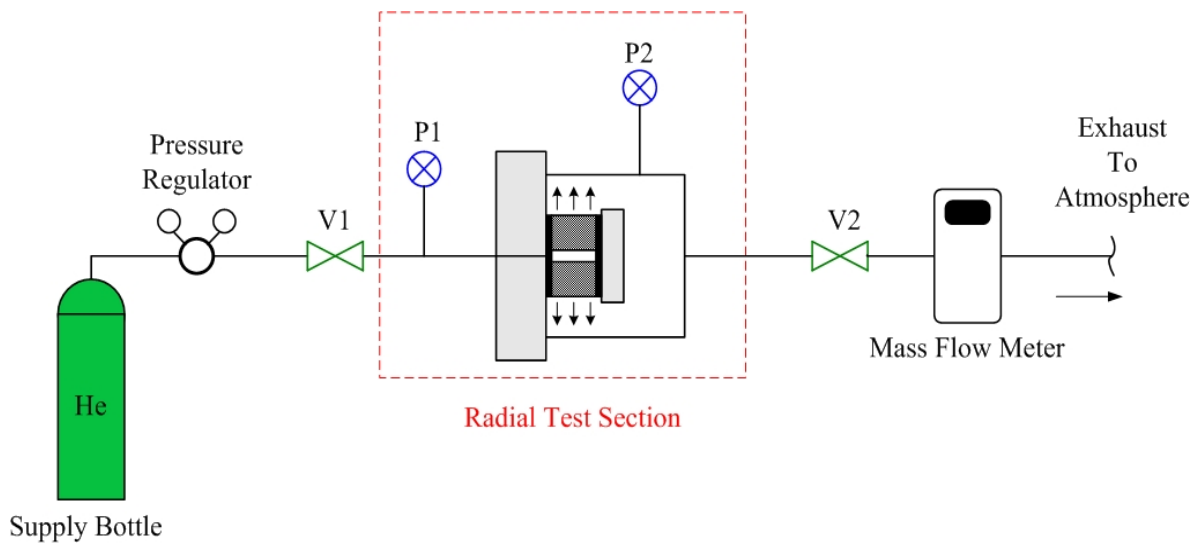


**Figure 3.7: Steady radial flow experimental setup diagram**

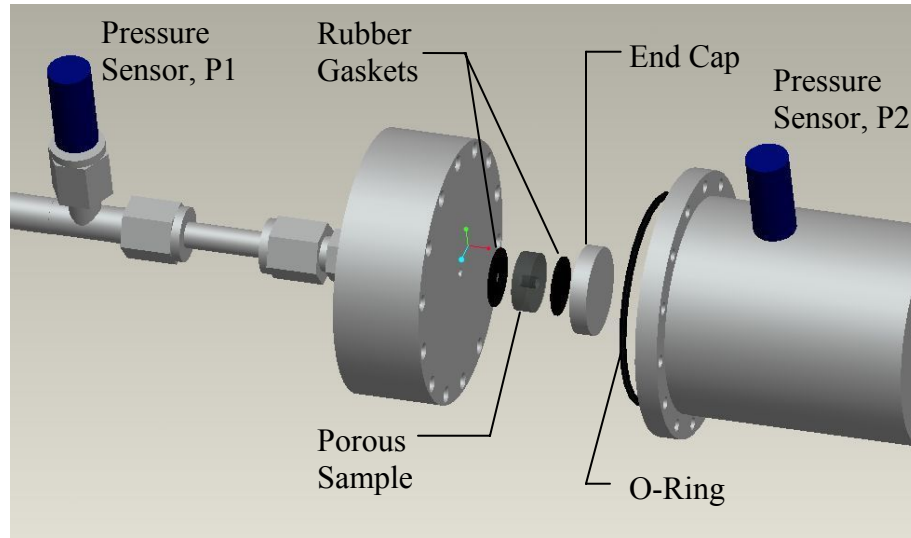


**Figure 3.8: Steady radial flow test section exploded CAD view**

The radial test section contains an annular ring of the porous media of interest mounted onto an aluminum slab constrained by an end cap, nuts and three threaded rods. The annular ring is composed of stacked discs of sample material with an inner diameter of 4.0 mm and an outer diameter of 20.0 mm. Radial test samples were specifically designed to produce a predominately radial flow regime within the porous media. Rubber gaskets on either side of the porous material ensure that all the mass flux passes in the radial direction through the inner diameter and exits through the outer diameter. The length of the annular porous sample is adjusted by tightening the nuts on the threaded rods to closely match the porosity of its axial counterpart. A detailed view of the test section and its surrounding area is shown in Figure 3.11.

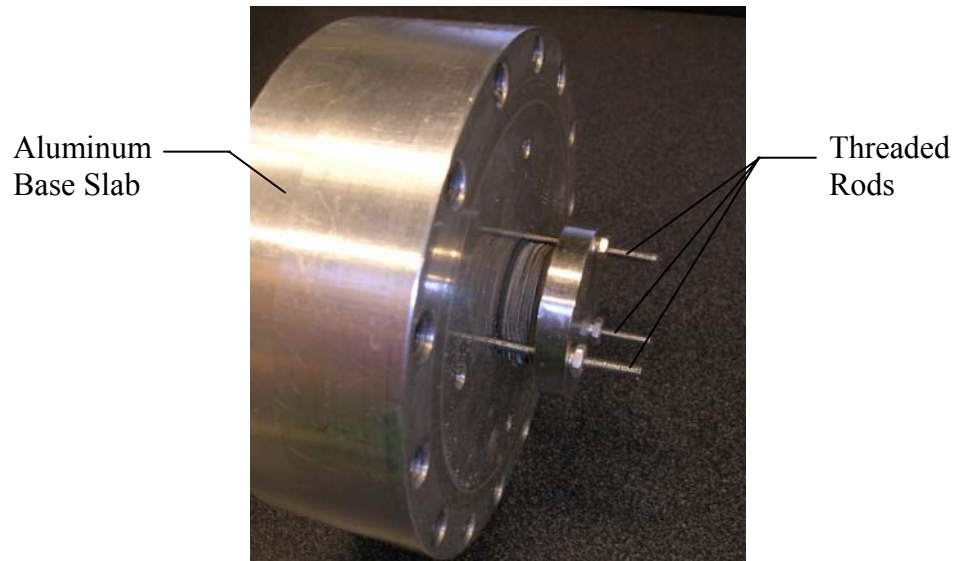


**Figure 3.9: Radial flow test section photograph**

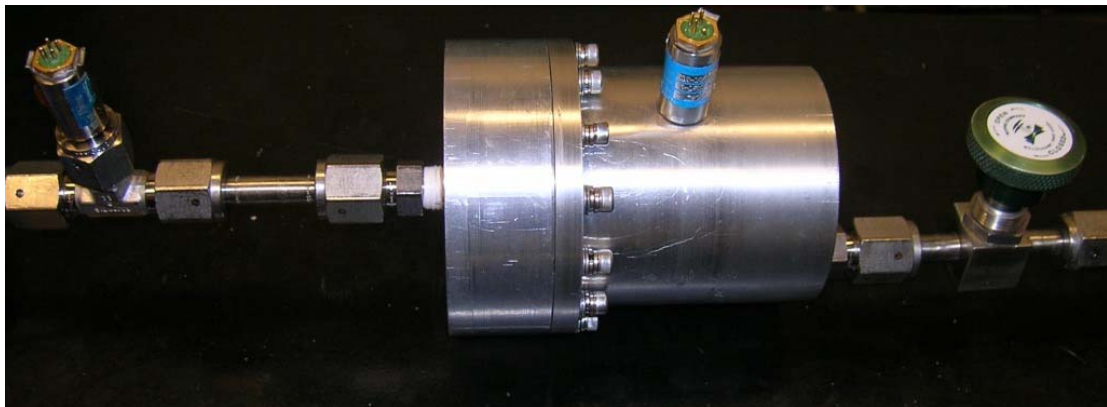


**Figure 3.10: Steady radial flow experimental setup photograph**

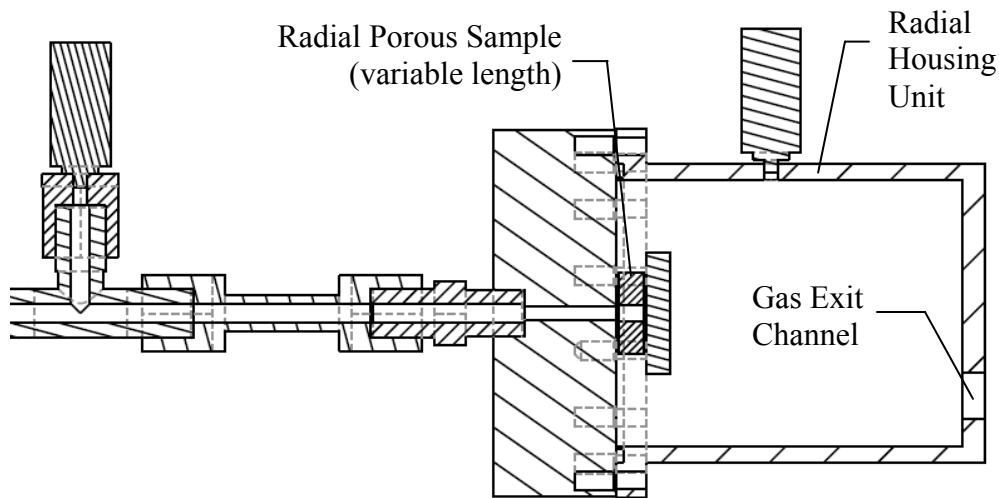


**Figure 3.11: Steady radial flow test section detailed CAD view**

Like the steady axial flow setup valves, V1 and V2, and the static pressure transducers, P1 and P2, are respectively located upstream and downstream of the test section. For the radial flow system, sensor P1 is mounted in an inline tee fitting before the test section inlet while sensor P2 is secured to the housing unit.

The testing procedure is the same as the steady axial flow experiment; the system is charged to 2.86 MPa (400 psig) and helium flows through the test section where it is eventually exhausted to the atmosphere. A range of flow rates between 0.0 and 1.5 g/s are controlled by valve V2. Pressure measurements are recorded for each discrete mass flow rate and a maximum allowable change in pressure across the test section was again limited to 0.69 MPa (100 psi). Plots displaying pressure drops as a function of mass flow rate were generated for each test sample. Data for each filler sample was curved fitted to a 2<sup>nd</sup> order polynomial. The curve fits were constrained with a zero intercept and would become the blueprint for defining the boundary conditions to be used for CFD

simulations. Discrete data points obtained from steady radial flow testing is tabulated in Appendix A.2.

### 3.4 Oscillatory Axial Flow

The oscillatory axial flow experimental setups consisted of a Hughes Aircraft Tactical Condor compressor, HP-Agilent 33120A function waveform generator and HP-Agilent 3852A data acquisition control unit, Crown DC-300A Series II amplifier, two high frequency PCB Piezotronics 101A05 dynamic pressure transducers, a specially designed test section containing porous media and the associated piping, fittings and a helium charge tank. The dynamic pressure transducers have a resolution of 0.002 psi (0.014 kPa). An HP VEE virtual console was operated to integrate all sensor measurements and store their output data. An iron core transformer was also utilized to offer better power transmission from the amplifier to the compressor. Displays of the oscillatory axial flow test setup are shown in Figure 3.12 through Figure 3.14.

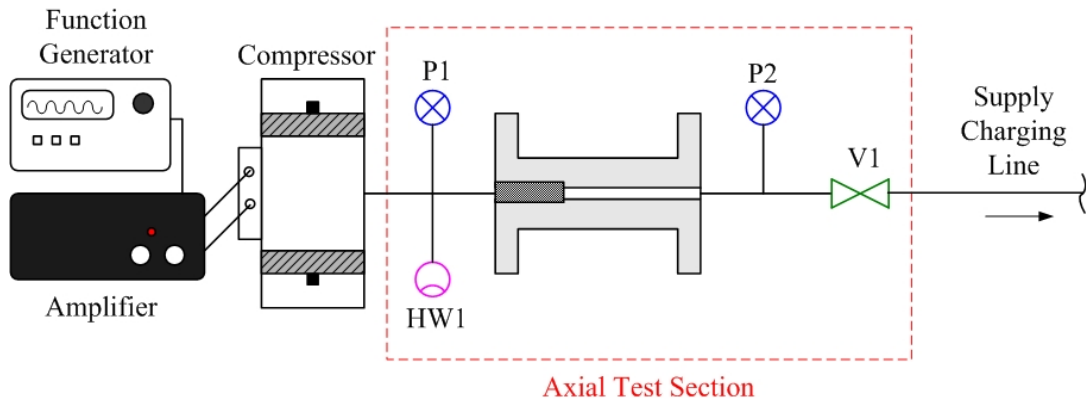


**Figure 3.12: Oscillatory axial flow experimental setup diagram**

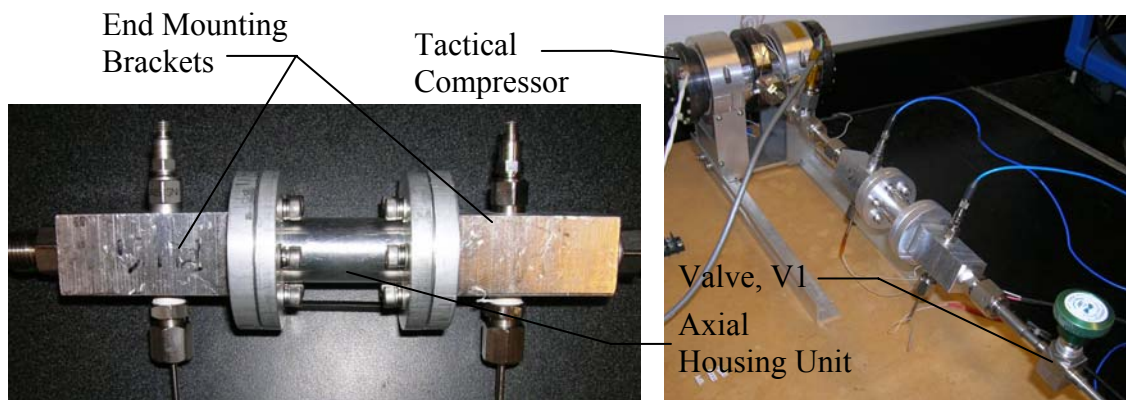


**Figure 3.13: Oscillatory axial flow experimental setup photographs**

The experimental setup for periodic flow is a closed system bounded by the compressor and the valve, V1. Oscillatory axial tests employed constant temperature hot wire anemometers; however, this data is part of continued research and will not be included in this investigation.

The oscillatory axial flow test section consists of the same sample pieces and housing utilized in its steady flow counterpart but includes unique end mounting brackets on either side of aluminum cylinder. Each bracket houses a single dynamic pressure sensor. End mounts also internally fitted with an  $8.0^\circ$  sloped transition cone located between the housing unit junction and sensor tap locations. This transition functions to avoid a large step change in pipe diameter and acts to reduce flow disturbances which would be present for such a large step change in diameter. A section view of the oscillatory axial test section is shown below in Figure 3.14. For complete dimensions of the oscillatory axial flow experimental setup, please refer to Appendix D.3.

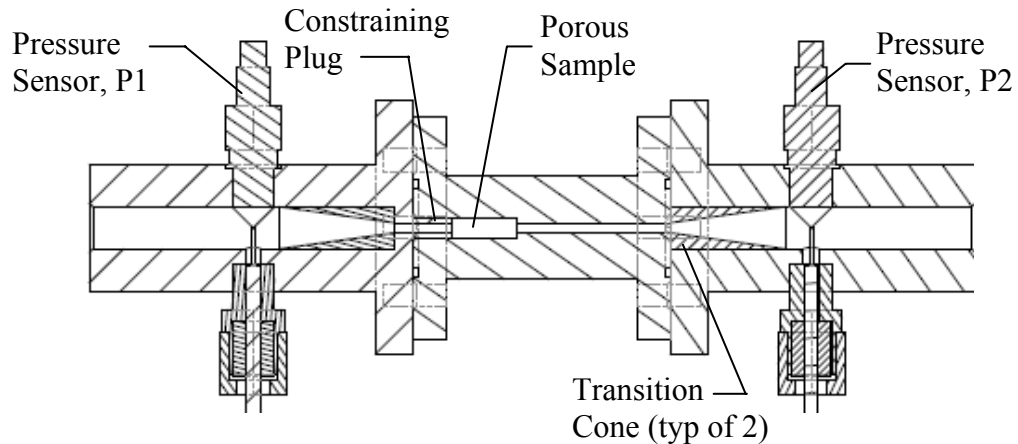


**Figure 3.14: Oscillatory axial flow test section detailed CAD view**

A sinusoidal signal sent from the function generator to the compressor is amplified to provide a stable pressure oscillation at each discrete frequency. The compressor's electrical input power is monitored and limited to 100 W to avoid any damages to the PWG. High flow data was taken for each sample at seven distinct frequencies in the 50 to 200 Hz range, in intervals of 25 Hz, at operating pressures of approximately 2.86 MPa and 3.55 MPa (400 and 500 psig). Low flow data obtained at 50 Hz for each charge pressure will be used to localize viscous resistances while high flow data will be used in determining inertial resistances. In this sense, an average set of resistance parameters will be found that satisfies the frequency band. Recorded periodic pressures are represented by their first three harmonics using a fast Fourier transform (FFT) of the experimentally measured waveform. Values and mathematical interpretation of this function will be explained in Section 4.4.

It should be mentioned that the PWG exhibits resonance in the frequency range of 30 to 60 Hz for loads similar to the oscillatory axial and radial flow test setups. These loads are dependent on the size, geometry and flow resistances such as the porous media.

It is possible to drive the compressor at off-resonant frequencies, however, stroke amplitude and the resulting pressure wave amplitudes diminish as the operating frequency moves further from resonance. This phenomenon is exhibited in Figure 3.15 for each oscillatory axial flow test sample and charge pressure (similar curves were found in the oscillatory radial flow testing). Although a compressor or a series of compressors with improved response in the frequency band of interest would be ideal; this model, unfortunately, was the only one available. Observations show that an increased charge pressure produces better compressor response and inlet pressure amplitude. This is due to a more favorable load as seen by the PWG.

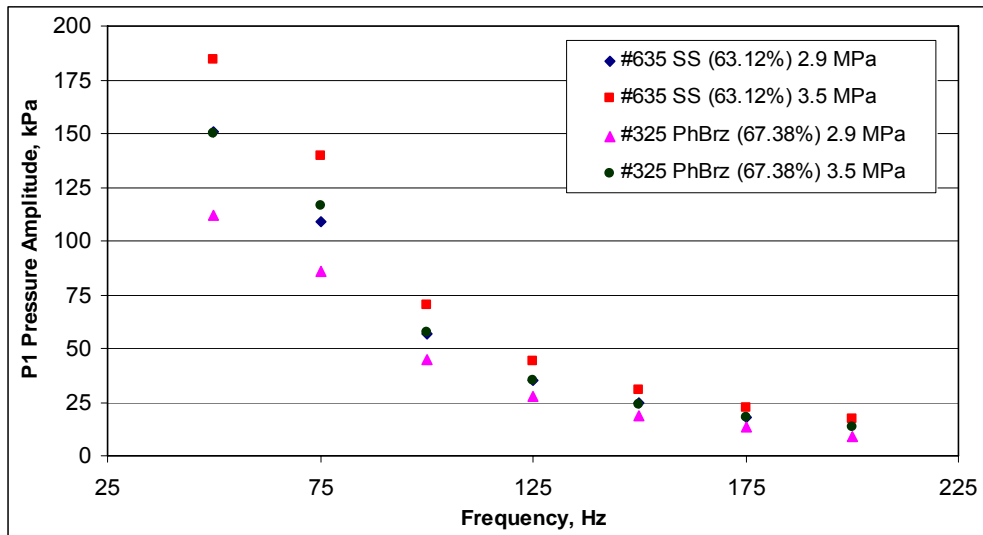


**Figure 3.15: Compressor response curves for oscillatory axial flow cases**

Sample empirical pressure waves at P1 and P2 locations for each frequency and charge pressure are characterized by their resulting amplitudes and the phase angle of P2 with respect to P1. The FFT representation of the experimental pressure at P1 will be used as a pressure inlet boundary condition for the CFD simulations. The iterative

solution process seeks to match the experimental and simulated pressures at P2 location by adjusting the hydrodynamic resistances of the porous sample. Experimental data for the oscillatory axial tests are listed in Appendix C.1.

### 3.5 Oscillatory Radial Flow

The oscillatory radial flow experimental setup consisted of the same equipment and experimental procedures as the oscillatory axial flow case, with the exception of porous test section, sample housing and its associated fittings and sensor integration. The setup contains the same tactical compressor, electronics, sensors and data acquisition structure. Visual aids for the oscillatory radial flow setup can be seen in Figure 3.16 through Figure 3.18.

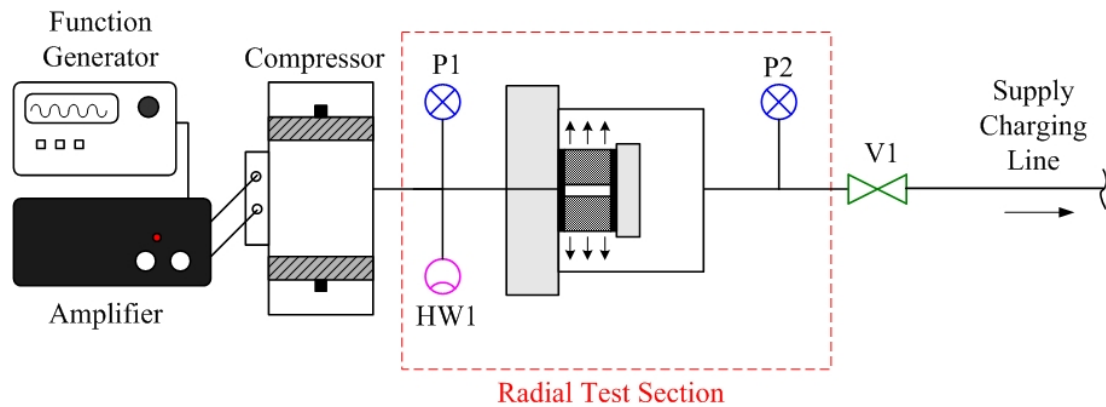


**Figure 3.16: Oscillatory radial flow experimental setup diagram**

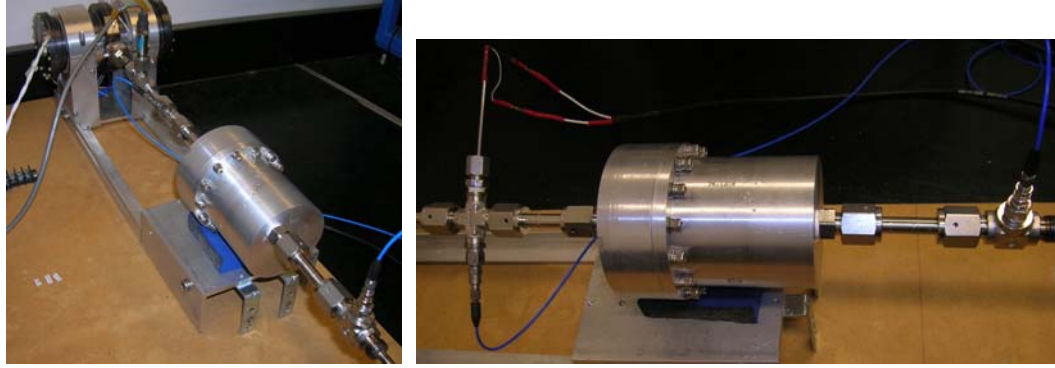


**Figure 3.17: Oscillatory radial flow experimental setup photographs**

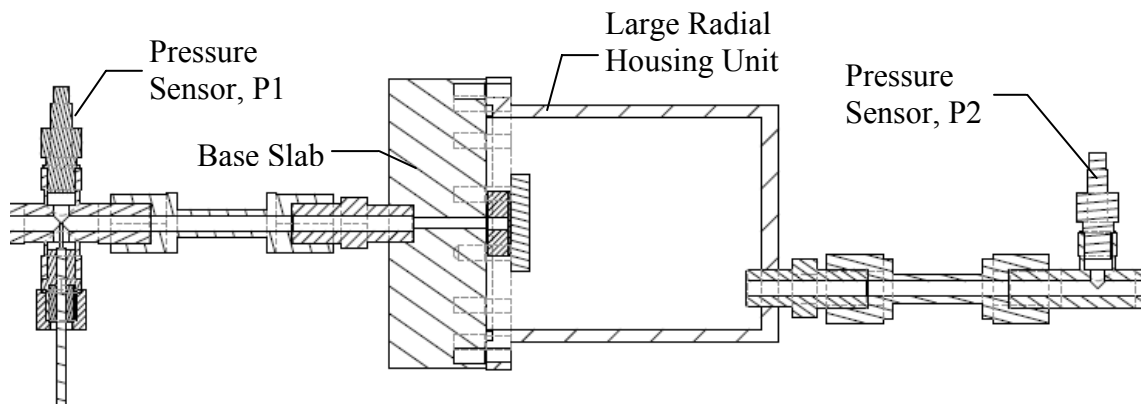


**Figure 3.18: Oscillatory radial flow test section detailed CAD view**

The radial test section utilized in the steady radial flow system is also employed in the oscillatory experiment. The setup is a closed system with pressurized helium bound by the compressor and valve V1. A dynamic pressure transducer (P1) and hot wire probe are located on the compressor side of the test section while another dynamic pressure transducer (P2) is positioned on the opposite side of the test section. Unlike the oscillatory axial flow test setup, sensory devices are mounted by inline fittings rather than end mounting brackets. Complete dimensions of the oscillatory radial flow experimental setup are tabulated in Appendix D.4.

Like the oscillatory axial flow case, testing is performed at charge pressures of 2.86 MPa (400 psig) and 3.55 MPa (500 psig) with operating frequencies ranging from 50 Hz to 200 Hz, at 25 Hz intervals. A sinusoidal signal sent to the compressor is amplified to provide stable pressure oscillations at each discrete frequency. The PWG produces pressure oscillations throughout the closed system and pressure waveforms at P1 and P2 locations are documented using the first three harmonics of an FFT.

At discrete frequencies, non-sinusoidal waveforms were recorded at the P2 location. As a result, two different radial housing units were employed in the oscillatory radial flow experimental setup. Each unit shared the same inner diameter of 65.8 mm (2.59 in) and flange connecting the housing to the radial slab. The smaller housing unit possessed an inside volume of 95 cm<sup>3</sup> (5.8 in<sup>3</sup>) and was originally utilized but then a larger shroud of 289 cm<sup>3</sup> (17.6 in<sup>3</sup>) was employed to avoid acoustical interference within the test section. Although this added another level of uncertainty, it seemed like a viable solution at the time. A summary of the oscillatory radial flow test runs and their associated housing unit is shown in Table 3.2.

Photographs of each of the radial housing units are shown in Figure 3.19 and experimental data for the oscillatory radial tests are listed in Appendix C.2.

**Table 3.2: Radial housing unit application**

Associated Housing Unit		Charge Pressure [psig]	Frequency [Hz]
#325 PhBrz	#635 SS		
Small	Large	400	50 (low)
Small	Large	400	50
Small	Large	400	75
Small	Large	400	100
Small	Large	400	125
Small	Large	400	150
Small	Large	400	175
Small	Large	400	200
Small	Large	500	50 (low)
Small	Large	500	50
Small	Large	500	75
Small	Large	500	100
Small	Large	500	125
Large	Large	500	150
Large	Large	500	175
Large	Large	500	200

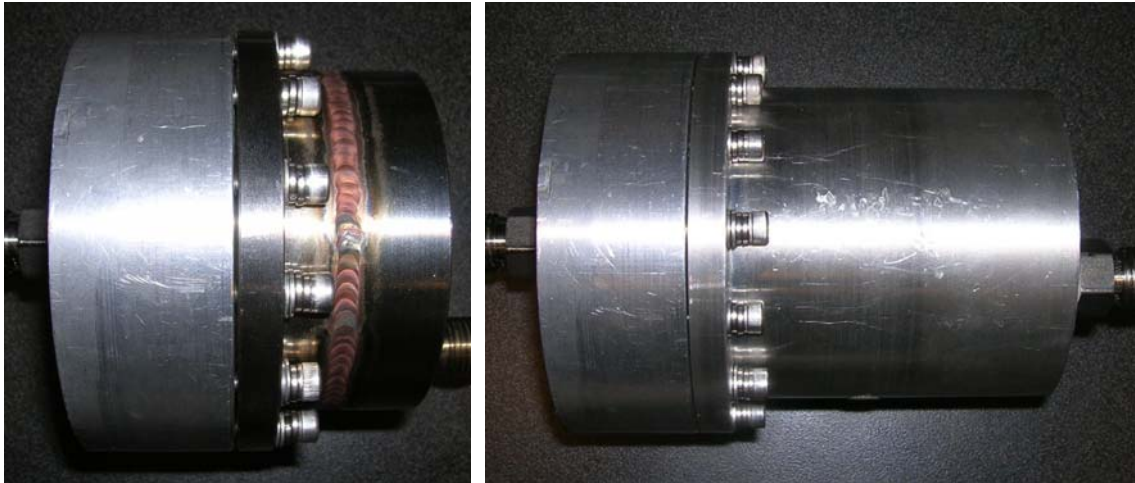


**Figure 3.19: Radial housing units**

## 4 COMPUTATIONAL METHODOLOGY

### 4.1 General Remarks

As described in section 3, four distinct types of hydrodynamic parameterization experiments were performed to completely characterize the flow resistances of stacked screens of #325 phosphor bronze and #635 stainless steel wire cloth samples. Consequently, four unique kinds of CFD cases were created to replicate the fluid behavior within test setups. Each simulation has attributes which are exclusive to the particular flow regime and direction. General statements concerning all CFD simulations will be followed by descriptions of the individual cases for each flow regime and direction.

The widely used CFD software package, Fluent, was used to determine the hydrodynamic parameters for both the steady and unsteady test samples. All computational models used a double precision, pressure based numerical solver with a Green-Gauss cell-based discretization scheme. All simulations comprised a nodalized grid representing the test section and its vicinity. This numerical solution technique applies initial conditions which converge on a complete solution of the flow field. All grids were two-dimensional, axisymmetric and created with Gambit. Appropriate boundary conditions are applied at the simulation inlet and outlet (where applicable) and all walls are treated as adiabatic with zero surface roughness.

Studies were performed on multiple grids for each case to determine how nodal spacing effected output variables. Reviews on steady flow simulations focused on how

mesh discretization altered the static pressure at the P1 location, while those created for oscillatory flow simulations observed amplitude and phase lag (with respect to the simulated pressure at P1) of the dynamic pressure predicted at the P2 location. Grids were refined until output variables reached their asymptotic limits. The grid with the fewest cell count and largest mesh spacing which provided negligible change in results within the accuracy of the measurements was used. This provide afforded the most efficient use of computational time.

The CFD code provides a complete picture of spatial and temporal (for unsteady cases) variations of local fluid velocity, pressure, density and temperature. Standard Navier-Stokes equations of motion govern laminar fluid flow while the Reynold's Average Navier-Stokes (RANS) k- $\epsilon$  model was used to describe turbulent flow fields where applicable. Energy calculation is performed through the ideal gas equation of state and continuity seeks to balance mass within the control volume. A universal set of convergence criteria or limits for errors associated with governing equations was employed for all simulations. These restrictions can be seen in Table 4.1 and include continuity, directional velocities, energy as well as k and epsilon for turbulent models. Model parameters such as first or second order discretization solver techniques and pressure velocity coupling methods were chosen for each setup to offer the best residual convergence.

**Table 4.1: Limits of convergence criteria**

Residual	Convergence Criteria
continuity	1.00E-07
x-velocity	1.00E-07
y-velocity	1.00E-07
energy	1.00E-08
k	1.00E-07
epsilon	1.00E-07

The porous sample within the test section is modeled by means of the volume averaged equations of fluid motion via sample porosity as explained in section 2.2. Theory of porous media offers simple macroscopic analysis but requires closure relationships to describe the complete fluid behavior through momentum sink terms. Fluent utilizes input values for the viscous and inertial resistances of the porous material. It is these values that are iteratively changed so that simulation results are equated to experimental data. The boundary conditions and matching techniques differ for the steady and oscillatory cases.

The chemical composition of the two mesh fillers is subject to the raw material obtained by the supplier and often varies with each purchase order. Therefore, a general constituent of representative stainless steel and phosphor bronze alloys and their subsequent average properties were inputted into the code for specific heat, thermal conductivity and density. Material properties for steel were obtained from Fluent's database while an average set of phosphor-bronze properties were found from matweb.com. Table 4.2 displays property values for both samples. With little variation in temperature, the contribution of these property values to the governing energy equations remains small.

**Table 4.2: Material property input values**

	Stainless Steel	Phosphor Bronze
Density [kg/m <sup>3</sup> ]	8030	8860
Specific Heat [kJ/kg·K]	502.48	380
Thermal Conductivity [W/m·K]	16.27	208

As with any numerical simulation there are always assumptions. First of all, the Research grade helium utilized in each experiment is modeled as a pure fluid with constant viscosity, as temperature generally remains constant at roughly 300 K. This assumption is also extended to the fluid and porous matrix properties of specific heat and thermal conductivity also being constant. Although model geometry is very close to the experimental setups things such as assembly thread depths, surface roughness and exact locations of pressure measurements are approximate. Radial flow setups are not entirely axisymmetric; with piping leading away from each housing unit as being slightly off center. Clearances between porous material and its housing are assumed to be negligible. Sample porous structures are also assumed to have uniform porosity. For hydrodynamic parameter determination for all cases, isotropic viscous and inertial resistances were assumed in Fluent simulations. This simplifying assumption was justified because the flow within the porous structure of each test apparatus was predominantly one-dimensional, constraining the viscous and inertial tensors to scalar form.

#### **4.2 Steady Axial Hydrodynamic Parameterization**

The steady axial flow experimental testing yielded axial pressure drops for discrete mass flow rates. Empirical data points for each sample were curve fitted to a 5<sup>th</sup> order polynomial with a zero intercept. Seven representative values across the full range of mass flow rates were chosen for CFD input analysis. A single Fluent case is created

for each of the seven data points and utilizes the mesh shown in Figure 4.1. Each case employs experimentally measured values of mass flow rate and pressure as boundary conditions at the simulation inlet and outlet, respectively. The grid used in each case modeled the fluid volume of the test setup geometry between the P1 and P2 pressure transducer locations spanning a channel of approximately 209 mm (8.22 in). A mesh comprised of 11,536 quadrilateral elements utilized a nodal spacing of 0.254 mm (0.01 in) in the longitudinal direction and an average radial spacing 0.18 mm (0.007 in).

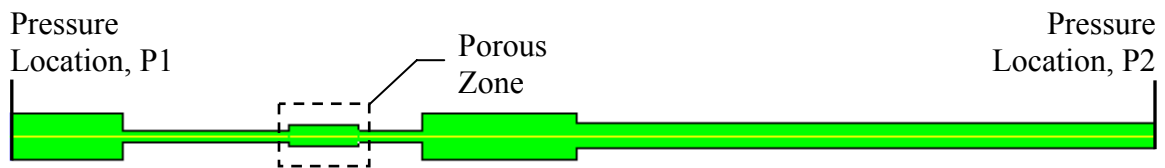


**Figure 4.1: Steady axial flow mesh**

Figure 4.1 displays the control volume used for CFD analysis. Inlet and outlet boundaries are labeled and the 4 mm channel housing the stacks of wire cloth samples is denoted as the porous zone. This region is modeled with isotropic hydrodynamic resistances or momentum sink terms while the other zones simply contain homogenous helium gas. The axisymmetric model is mirrored across its centerline axis and automatically sets all normal velocity components along this boundary to zero.

A control scheme of first order upwind discretization (FOUD) method with a simple pressure-velocity coupling was employed by the solver. As a result of the high Reynold's numbers observed during test runs, a turbulent viscous model was used. The two equation, k- $\epsilon$  turbulence model offered greater residual convergence than its laminar counterpart. A reference pressure of 1 atmosphere (101.325 kPa) was applied to the

system and a steady-state solver was employed. As previously mentioned, grid vertices of the steady axial flow setup are shown in Appendix D.1. Simulation grids for both the #635 stainless steel and #325 phosphor bronze samples were identical, only their porous zone material properties and subsequent resistance parameters differed.

Initial viscous and inertial resistances were applied to the porous zone and the model was iterated until residual convergence was obtained. At steady-state, the simulation's area-weighted average pressure at the P1 location was recorded and compared with experimental static gage pressure measured at that location. Viscous and inertial resistances were adjusted until there was agreement between the simulation's predicted pressure at the P1 and the empirical data. This process was done for all seven representative data points and another curve fit solution of the simulation's pressure drop as a function of mass flow rate was generated and matched the experimental data curve with the least amount of error for the given range of flow rates. A unique set of resistance parameters were determined for each sample filler material.

For both the steady axial and radial flow cases, the viscous resistance could be deduced at low flow conditions when inertial effects were small. Using the described procedure, the first two or three data points were utilized to resolve the viscous resistance parameter. Once this value was established, only the inertial resistance was iteratively attuned while the viscous term was fixed. This concept is rooted in the theory of porous media, as described in section 2.2. At low flow rates the viscous resistance term dominates while the inertial term is small. On the other hand, at large velocities the inertial term prevails over the viscous term. This technique would be slightly modified for the oscillatory cases.

### 4.3 Steady Radial Hydrodynamic Parameterization

The procedure for determining the steady radial flow hydrodynamic parameters was very similar to the steady axial flow parameterization. The implicit solution processes were identical; however, the geometry and subsequent model grids differed from the steady flow cases. Steady radial flow experimentation produced pressure drops for discrete mass flow rates for the stainless steel and phosphor-bronze samples. Each simulation models the 170 mm (6.71 in) long fluid volume within the test section and its vicinity between the P1 and P2 locations. A display of the simulation's mesh is shown in Figure 4.2.

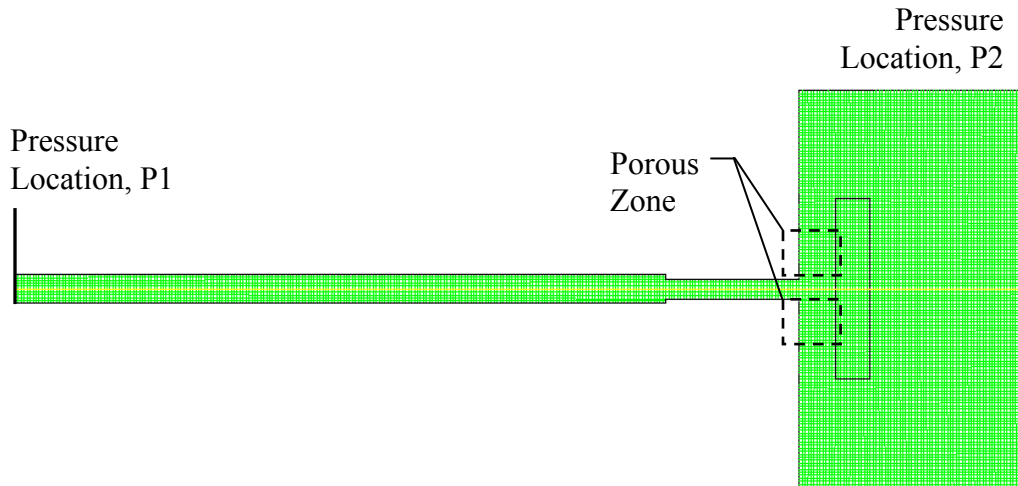


**Figure 4.2: Steady radial flow mesh**

Figure 4.2 is the CFD representation of the fluid control volume for the steady radial flow tests. Boundaries are displayed at inlet (P1) and outlet (P2) pressure locations and the annular sample is labeled as a porous zone.

A control scheme of FOU D with a simple pressure-velocity coupling was used by the solver. Laminar flow regimes provided excellent model convergence and negligible

differences were observed in output variables when turbulence flow was applied. A reference pressure of 1 atm was applied to the system and a steady-state solver was used. Grids for both the #635 stainless steel and #325 phosphor bronze samples were similar; however the length of the radial porous segment varied for each sample and lengths can be found in Table 3.1. The stainless steel and phosphor bronze sample grids both resulted in 6,730 nodes, utilizing a mesh scheme of quadrilateral elements with an average grid spacing of 0.5 mm in the longitudinal and lateral directions.

The physical length of the radial test sample was modeled; however, gaskets and threaded rods used in the experimental setup were excluded from the simulation. The end cap which constrained the radial samples was included in the model and treated as a homogeneous aluminum solid with adiabatic surfaces. Model grid vertices are shown in Appendix D.2.

Using the curve fit data of the pressure drop versus mass flow rate plot, seven data points across the full range of flow rates are used for CFD analysis. Each Fluent case applies experimental values of mass flow at the inlet face and pressure at the outlet or P2 location. Initial viscous and inertial resistances were applied to the porous zone and the steady-state model was iterated until residual convergence was obtained. Upon convergence, the simulation's area-weighted average pressure at the P1 location was recorded and resulting plots of pressure drop versus mass flow were generated from the simulation's predicted inlet pressure.

Viscous and inertial resistances of the porous region were adjusted until there was agreement between the simulated pressures predicted at P1 and those experimentally measured at P1 for all seven representative data points. As mentioned in section 4.2, the

viscous resistance term was identified at low flow conditions and affixed at higher flow data points where the inertial resistance parameter was then optimized. A unique set of steady radial flow resistance parameters were determined for each sample filler material.

#### 4.4 Oscillatory Axial Hydrodynamic Parameterization

The oscillatory axial flow experimentation produced pressure waveforms at P1 and P2 locations at discrete frequencies and charge pressures. Consequently, a single unsteady Fluent case was constructed for each frequency and fill pressure. The mesh utilized in each case modeled the fluid control volume within the axial test section and its vicinity between the P1 location and the valve V1. A mesh scheme comprised of quadrilateral elements was applied with a grid spacing of 0.5 mm (0.02 in) for both the longitudinal and lateral directions. This, coupled with the transition cones included on either side of the test sample, resulted in a mesh of 1,975 cells for all oscillatory axial flow cases. A display of the simulation's grid can be seen in Figure 4.3 spanning a length of 202 mm.

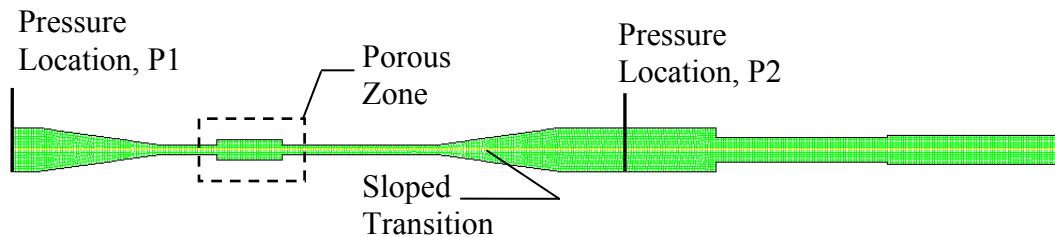


**Figure 4.3: Oscillatory axial flow mesh**

A second order upwind discretization (SOUND) control scheme was implemented in the solver with a simple pressure-velocity coupling. Reference pressures of approximately 2.86 MPa (400 psig) and 3.55 MPa (500 psig) were applied to their

respective cases. Laminar flow was utilized in the simulation offering efficient use of computational time. Turbulence models were applied, but produced negligible changes in results. It is believed that the pressure waves generate a flow field where gas displacements and velocities are small and therefore a transition to turbulence is never reached.

FFT representations of the experimental pressure waveform data documented at the P1 and P2 locations lay the foundation for the CFD-assisted methodology for all oscillatory cases. The empirical pressure waveform measured at P1 is applied as the model's inlet boundary condition. The first three harmonics of the FFT are utilized in a user defined function (UDF) to create a periodic pressure profile at the simulation's inlet. The resulting oscillating boundary condition takes the form of Eq. (4-1) where series amplitudes are expressed as  $Z_j$  and their associated phase angles are shown with  $\phi_j$ . Any DC offset of this measured series is excluded from the UDF as it is already accounted in the model charge pressure. The C+ code compiled by Fluent which defines the UDF can be found in the Appendix B.

$$P_{osc} = Z_1 \cos(\omega t + \phi_1) + Z_2 \cos(2\omega t + \phi_2) + Z_3 \cos(3\omega t + \phi_3) \quad \text{Eq (4-1)}$$

$$\omega = 2\pi\lambda \quad \text{Eq (4-2)}$$

Eq. (4-2) specifies the angular frequency,  $\omega$  in *rad/s* from the operating frequency,  $\lambda$  in Hz. The three terms of the FFT representation each have unique amplitude and phase

angle component. Only the first three terms were included in the series as higher order terms have a diminishing effect the resulting waveform.

An example of the experimental data collected for the #325 phosphor-bronze sample oscillatory axial flow case is shown in Table 4.3. This data and the rest of the oscillatory flow experimental values are charted in Appendix C.

**Table 4.3: Experimental FFT representation of #325 Ph-Brz data for axial flow**

Operating Frequency [Hz]	Charge Pressure [MPa]	P1 Location					
		Pressure Amplitude			Phase Angle		
		Z <sub>1</sub> [Pa]	Z <sub>2</sub> [Pa]	Z <sub>3</sub> [Pa]	φ <sub>1</sub> [rad]	φ <sub>2</sub> [rad]	φ <sub>3</sub> [rad]
50 (low)	2.84	17336.472	86.738499	188.09321	-0.425857	-1.024908	0.4870898
50	2.84	110914.81	1829.4656	909.33229	-0.568598	-1.341476	1.3395003
75	2.85	85728.893	842.88224	941.66388	-1.199184	-2.668835	-1.083498
100	2.86	44860.351	127.29729	403.82399	-1.482928	2.5186019	-2.437729
125	2.87	27501.717	82.402821	258.82494	-1.644879	2.4533432	-1.830782
150	2.88	18880.253	57.437168	169.12335	-1.756874	2.0603642	2.4902432
175	2.88	13606.072	35.045127	120.21811	-1.791937	1.9546105	2.0192996
200	2.88	8570.085	18.769055	70.198325	-1.806852	1.8336795	1.5486806

Unsteady Fluent cases must be solved at discrete instances in time. These time steps are very important to the simulation’s accuracy of the resulting pressure waveforms. Ideally, the time step should be small enough to capture significant changes in output variables and large enough to allow efficient use of computational time. A standard of roughly 200 times steps per period was employed in all unsteady simulations to provide a resolution of at least 2.0 degrees when comparing the phase angle of the P2 pressure waveform with respect to P1. An increased number of time steps per period were necessary for model convergence of lower frequency cases.

Table 4.4 shows the frequency dependent solution parameters used in all unsteady models.

**Table 4.4: Unsteady simulation time steps**

Frequency [ Hz ]	Period [ s ]	Time Step [ s ]	Steps / Period [ - ]
50	0.02000	5.00E-05	400.00
75	0.01333	5.00E-05	266.67
100	0.01000	5.00E-05	200.00
125	0.00800	4.00E-05	200.00
150	0.00667	3.00E-05	222.22
175	0.00571	3.00E-05	190.48
200	0.00500	2.50E-05	200.00

Experimental pressure data at the P1 and P2 locations was obtained for seven distinct frequencies from 50 to 200 Hz, at 25 Hz intervals, and at low flow conditions at 50 Hz, resulting in eight separate CFD cases for each sample filler and charge pressure. Initial guesses for viscous and inertial resistances are applied to the porous zone and unsteady models are required to run for multiple period cycles to reach periodic steady state. Generally, 10 periods from initiation to periodic a steady-state provided enough time for any transient phenomena to stabilize. Monitors record the simulation's dynamic pressure at the P1 and P2 locations. It is this simulated pressure waveform at the P2 location that is compared and matched to the experimental waveform at that location, providing the basis for oscillatory hydrodynamic parameter determination.

The model porous region's viscous and inertial resistances are iteratively corrected until there is good agreement between the simulation and experimental dynamic pressures at the P2 location across the range of tested frequencies. Graphical interpretation of harmonic waveforms includes pressure amplitude and phase lag with respect to the pressure waveform at P1. These tools will be used to numerically compare simulated results to those measured in experiments. Ideally, a unique set of

hydrodynamic parameters will provide a match in amplitude and phase angle between experimental and simulation waveforms at P2.

Similar to its steady state counterpart, the viscous resistance was initially determined at 50 Hz low flow conditions, where inertial effects were considered to be small. A range of prescribed viscous resistances were established, inertial resistances were adjusted to match experimental conditions.

#### 4.5 Oscillatory Radial Hydrodynamic Parameterization

The CFD-assisted methodology for determining the oscillatory radial hydrodynamic parameters was identical to the oscillatory axial case with the exception of the simulation geometry including the radial test section and its surrounding area. The mesh represents the area between the pressure sensor at P1 location and the valve V1. A display of a typical oscillatory radial flow mesh is shown in Figure 4.4.

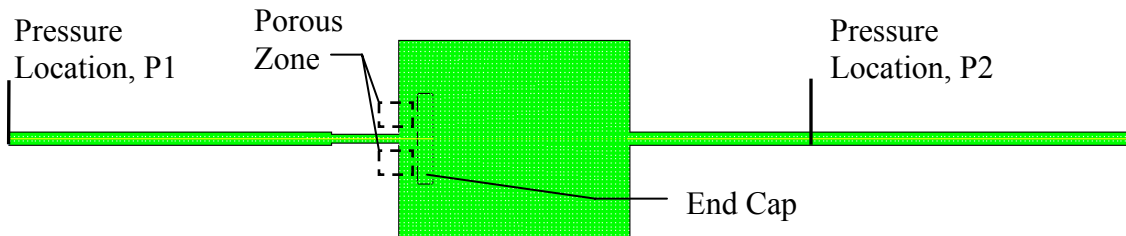


**Figure 4.4: Oscillatory radial flow mesh for large radial housing unit**

Grids for both the #635 stainless steel and #325 phosphor-bronze samples were similar; however the length of the radial porous segment differed for each sample. Even though the oscillatory radial flow experimental setup does not possess uniform radial symmetry, all Fluent cases contain an axisymmetric mesh for simplicity.

A mesh of quadrilateral elements was applied with a spacing of 0.5 mm in the longitudinal and lateral directions resulting in a total of 7,374 and 14,007 cells for the small and large volumes, respectively. The solver utilized a SOUD control scheme with a PISO pressure-velocity coupling. Appropriate charge pressures were applied and a laminar flow model was used. The FFT representation of experimental pressure at P1 in the form of Eq. 4-1 is applied through a UDF pressure profile as an inlet boundary condition. Complete grid dimensions can be found in Appendix D.3.

The implicit solution and matching technique remains the same as the oscillatory axial flow case. Experimental measurements produce pressure waveforms at the P1 and P2 locations and the CFD-assisted process iteratively changes viscous and inertial resistances, seeking to match empirical and simulation data.

## 5 RESULTS

In this chapter, experimental measurements obtained from each test setup are provided and discussed. The results of CFD analysis used for determining the anisotropic hydrodynamic resistance parameters of the #635 stainless steel and #325 phosphor bronze samples are also explained. Steady and oscillatory hydrodynamic parameters are used to calculate the directional Darcy permeability and Forchheimer's inertial coefficient for filler materials. Dimensionless friction factors using a particular Reynolds number will be employed for comparison. Findings from the pressure dependence study are also reported.

### 5.1 Steady Flow Results

Steady flow experimental testing produced pressure drop data for a range of mass flow rates as previously discussed in sections 3.2 and 3.3. Using empirical data as boundary conditions, the fluid control volume within the axial and radial test section and its vicinity were modeled using CFD code. Simulations sought to iteratively change porous media hydrodynamic resistances so that model predictions of inlet pressure matched experimental measurements.

Steady flow tests were performed for both porous structures at a supply pressure of 2.86 MPa (400 psig). Flow was modulated from the supply bottle to provide a suitable range of mass flow rates while limiting the maximum pressure drop to 0.69 MPa (100

psi). Multiple test runs were performed for each mesh filler in axial and radial flow directions.

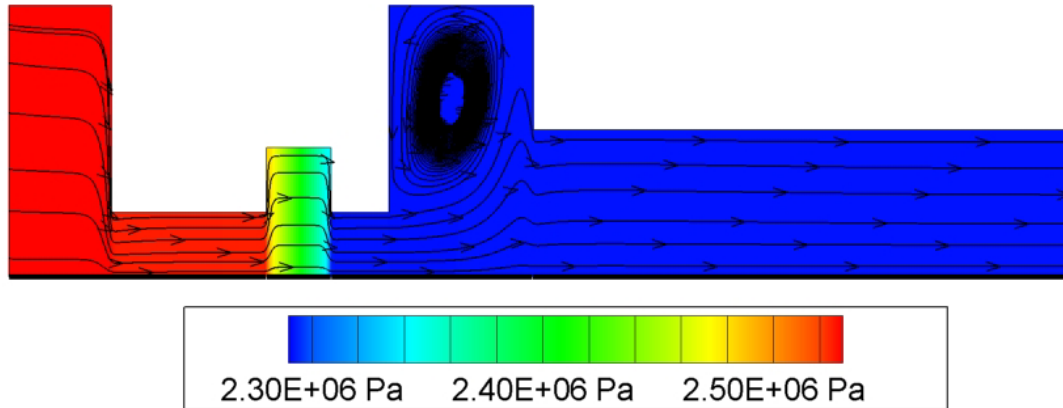


**Figure 5.1: Pressure contour of #325 Ph Brz steady axial flow case at 0.546 g/s**

Figure 5.1 illustrates the pressure drop across the porous sample in for a #325 phosphor bronze steady axial flow case at 0.546 g/s. The contour plot suggests that virtually all of the fluid's flow resistance can be attributed to the stacked screens of wire cloth material and that other pressure loss mechanisms are small in comparison. With adiabatic wall surfaces and a constant ambient temperature of 300 K used at the inlet and outlet boundaries, steady flow simulations reported negligible temperature deviations. Accordingly, fluid density reacted with changes in pressure through the ideal gas relationship. Several streamlines are added for increased visualization within the test section. A recirculation zone is observed downstream of the porous region as a result of the sharp step change in diameter.

Figure 5.2 displays pressure drop as a function of mass flow rate for the two axial flow test samples. Discrete experimental data points are shown for the stainless steel and phosphor-bronze samples. Curves representing the simulation's predicted pressure drop

across the range of flow rates are superimposed on the chart for comparison. Steady axial flow tests yielded a range of flow rates from 0.044 g/s to 0.911 g/s. Error bars represent the uncertainty of pressure drop and mass flow rate associated with empirical data points. The combined uncertainty for both static pressure measurements was  $\pm 17.1$  kPa while the mass flow meter yielded an uncertainty of  $\pm 0.0225$  g/s.

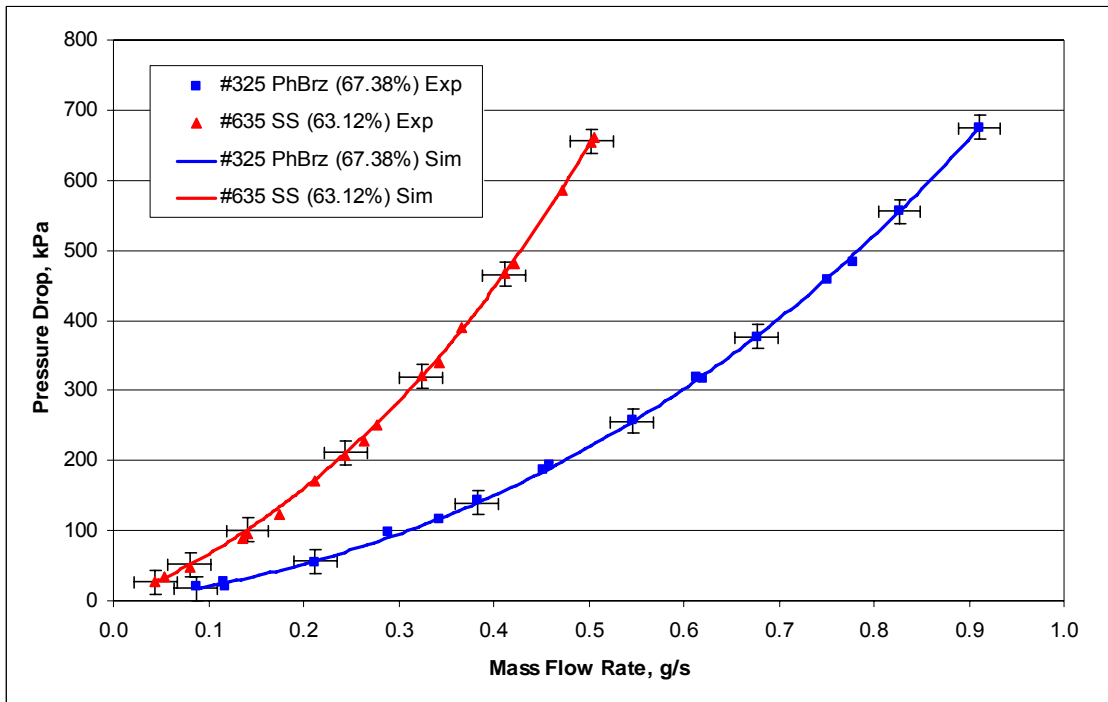


**Figure 5.2: Steady axial flow pressure plot**

The steady axial flow measurements were found to be very reproducible and uncertainty remained small with respect to the recorded pressure drops across the range of flow rates. Due to the small cross sectional area of the axial test sample and housing, large pressure drops of up to 674 kPa were recorded in those tests offering a maximum mass flow rate of 0.91 g/s for the more porous, #325 phosphor bronze sample. Viscous and inertial resistances of  $9.95E10 \text{ m}^{-2}$  and  $69,000 \text{ m}^{-1}$  displayed excellent agreement for

the #635 stainless steel axial sample for the tested flow rates while resistances of  $2.85 \times 10^4 \text{ m}^{-2}$  and  $27,500 \text{ m}^{-1}$  produced simulated pressure drops for the #325 phosphor-bronze in accord with experimental results.

To determine the accuracy of the CFD predicted pressure drops, polynomial trend lines representing the experimental data and simulation predictions are numerically compared. A maximum deviation of 4.7% was reported for all axial samples' CFD-calculated pressure drops as compared with experimental data for discrete flow rates ranging from 0.1 g/s to 0.9 g/s. Average deviations of 1.3% and 2.2% were evaluated for the #325 phosphor-bronze and #635 stainless steel axial samples, respectively.

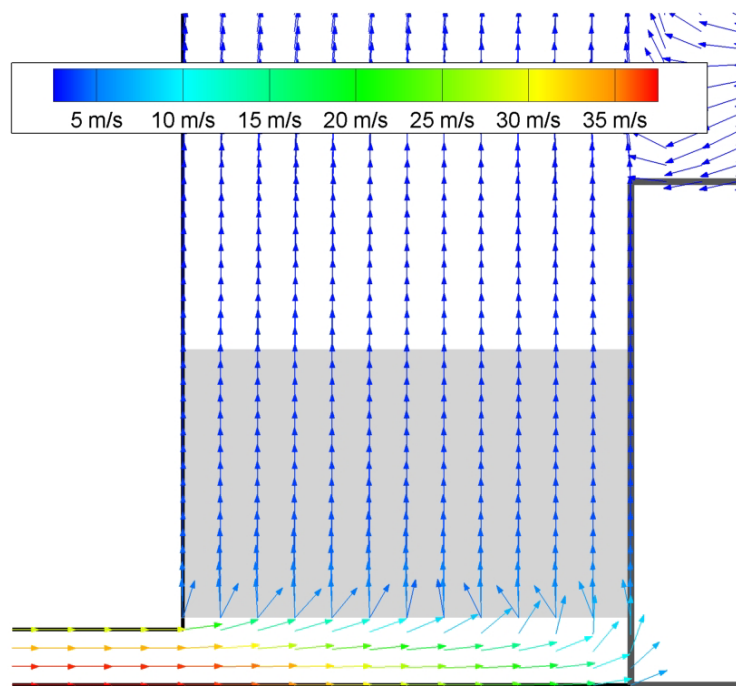


**Figure 5.3: Vector plot of #635 stainless steel radial porous sample at 1.218 g/s**

As mentioned in section 3, the design of each test apparatus was expected to render the flow in the porous test section primarily one-dimensional. The CFD

simulations have shown that this was indeed the case. The velocity vector plot of a typical steady flow radial test run is displayed in Figure 5.3. The two dimensional view of the fluid control volume focuses on the porous sample which is shaded and its immediate surrounding area. This particular case depicts the velocity vectors of the #635 stainless steel case at a mass flow rate of 1.218 g/s. The flow is evidently predominately radial within the porous region, except for flow within the annular sample. As expected, high velocities are recorded at the inlet channel and the porous segment decreases the fluid motion to roughly 5 m/s as gas exits the sample.

Steady radial flow testing produced only minor pressure losses across the range of mass flow rates. A possible solution to this issue was thought to decrease the length of the radial samples by using a fewer number of annular screens. This modification would increase the lateral mass flux passing through the sample for a given flow rate, therefore increasing the loss of pressure. The lengths of the radial samples must also be large enough to provide an identifiable continuous porous structure of random orientation. Sample lengths discussed in section 3.1 were finalized and resulted in a maximum pressure drop of only 40 kPa for the less porous, stainless steel filler.

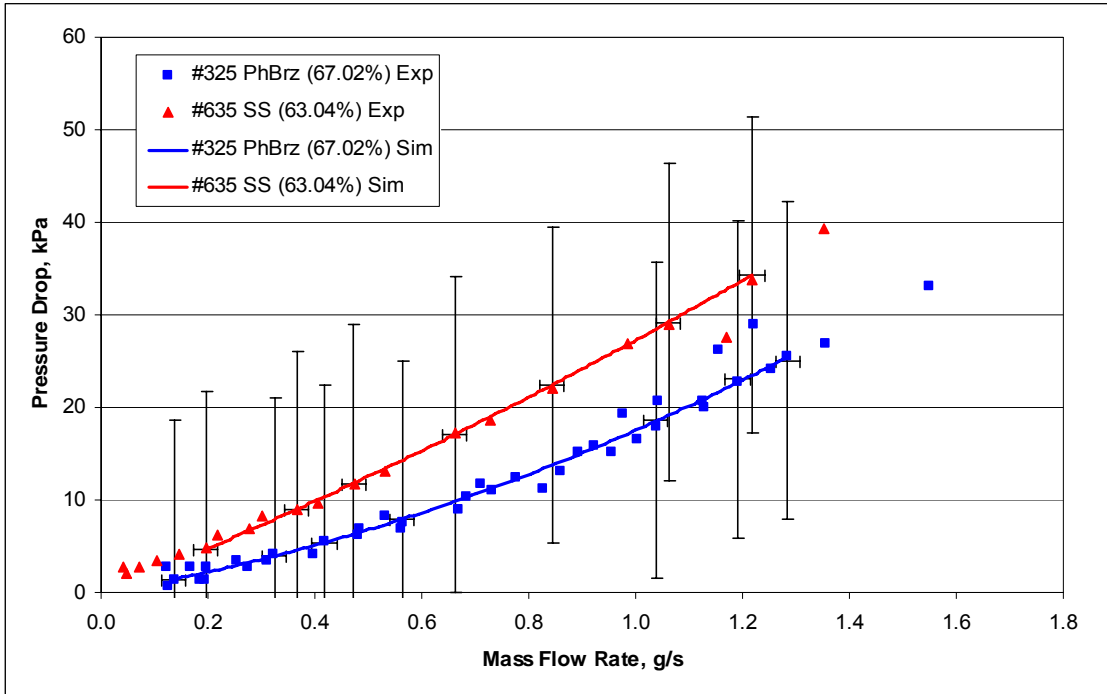


**Figure 5.4: Steady radial flow pressure plot**

Figure 5.4 plots discrete radial pressure drops for the #325 phosphor bronze and #635 stainless steel samples. Polynomial curves with zero intercept represent the CFD simulation's predicted pressure drop across the range of flow rates. The approximately linear profile of the radial pressure drop plots would suggest a predominately Darcy or viscous flow pattern in these experiments, with little inertial effects. Scatter can be observed in the data as the pressure differences recorded approached the uncertainty associated with the pressure transducers.

Nevertheless, comparative analysis was performed on the experimental and simulated quadratic curve fits. A maximum deviation of 5.7% was reported for all radial samples' CFD-calculated pressure drops as compared with experimental trend lines. Average deviations of 3.6% and 0.8% were evaluated for the #325 phosphor bronze and #635 stainless steel radial samples, respectively. The optimal steady radial flow viscous

and inertial resistance parameters which minimized this error were  $2.85E10 \text{ m}^{-2}$  and  $58,000 \text{ m}^{-1}$  for the #325 phosphor-bronze filler and  $1.24E11 \text{ m}^{-2}$  and  $59,000 \text{ m}^{-1}$  for the #635 stainless steel mesh.

Due to the relatively small pressure changes viewed for steady radial testing, resulting data and directional parameterization is suspect. Radial sample geometry had inner and outer diameters of 4 mm and 20 mm, respectively. This created a superficial length of only 16 mm for the fluid to traverse in the lateral direction. By employing an annular sample with larger outer diameter and an increased porous fluid flow path, enlarged pressure drops would be reported for a given flow rate. Another option to decrease uncertainty in pressure measurements would be to make use of different sensors with enhanced accuracy. Both of these concepts would provide more precise measurements leading to improved steady radial flow mesh characterization. Due to high material costs for the #635 stainless steel mesh cloth, the predetermined radial test sample geometry could not readily be redesign with newly fabricated screens. Using Eq. 2-19 and Eq. 2-20 from section 2.2, hydrodynamic resistances along with sample porosity are used to calculate the Darcy permeability and Forchheimer's inertial coefficient of the volume averaged porous region.

Table 5.1 summarizes the steady flow results including the directional viscous and inertial resistances and their associated directional permeability and inertial coefficient for the #325 phosphor bronze and #635 stainless steel mesh filler samples.

**Table 5.1: Steady flow sample hydrodynamic parameters**

Porous Media	Measured Porosity [-]	Viscous Resistance [m <sup>-2</sup> ]	Inertial Resistance [m <sup>-1</sup> ]	Darcy Permeability [m <sup>2</sup> ]	Forchheimer's Coefficient [-]
Axial Samples					
#325 Phosphor Bronze	0.6738	2.85E+10	27500	1.593E-11	0.179
#635 Stainless Steel	0.6312	9.95E+10	69000	4.004E-12	0.275
Radial Samples					
#325 Phosphor Bronze	0.6702	2.85E+10	58000	1.576E-11	0.382
#635 Stainless Steel	0.6304	1.24E+11	59000	3.205E-12	0.211

The directional hydrodynamic parameters listed in Table 5.1 are the culmination of the iterative solution process used to determine the fluid behavior within the porous sample under steady flow conditions. It is shown that the less porous, #635 stainless steel mesh exhibited much greater pressure drops for a given flow rate and consequently possessed larger resistances when compared to the #325 phosphor bronze sample for both the axial and radial tests. Differences are exhibited in hydrodynamic resistances for both filler materials in either the lateral or longitudinal flow directions; however, this discrepancy is amplified for the #635 stainless steel set. These findings confirm the fact that when multidimensional effects are apparent in systems like miniature cryocoolers, it is essential to utilize anisotropic mesh filler characteristics for accurate modeling of fluid behavior.

With knowledge of material resistance parameters, a non-dimensional comparison using the friction factor can be correlated. By employing the average superficial velocity within the porous material, a steady flow friction factor can be solved for a range of Reynolds numbers. These results are shown in Figure 5.5 and Figure 5.6.

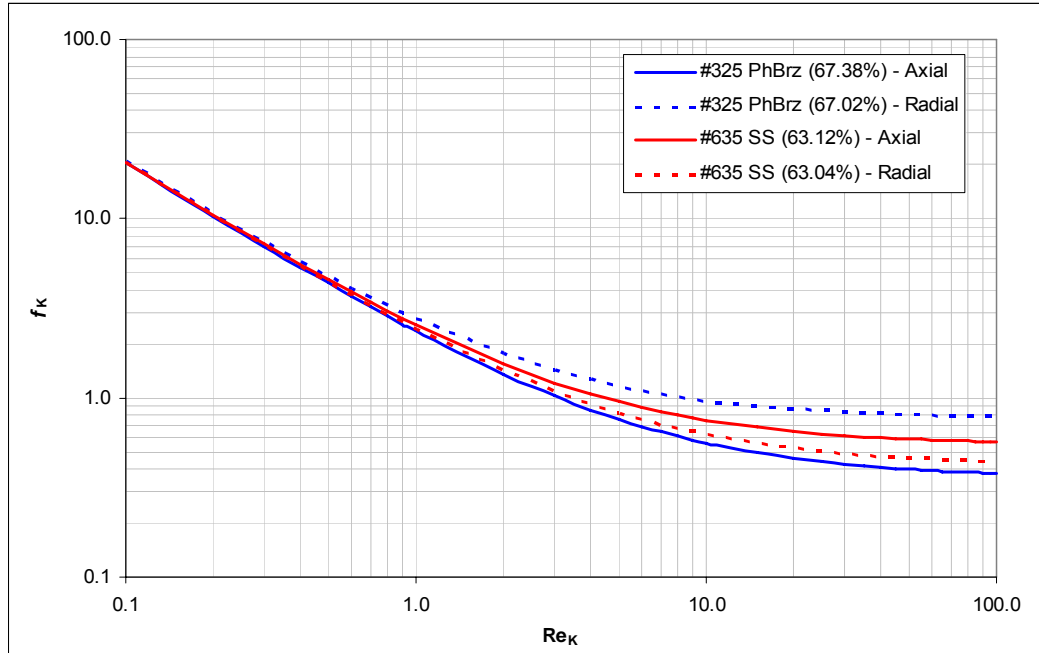


**Figure 5.5: Steady flow friction factors based on Darcy permeability**

The measured steady flow data for the axial and radial #325 phosphor bronze and #635 stainless steel fillers spanned a range of  $Re_k$  numbers of 0.02 to 14.9 though data from the resulting resistance parameters are extrapolated from 0.1 to 100. As mentioned in section 2.2, the steady friction factor asymptotically approaches a constant value at very large  $Re_k$ . Results of Figure 5.5 suggest that flow impedance is greatest for the radial #325 phosphor-bronze sample and smallest for the axial #325 sample.

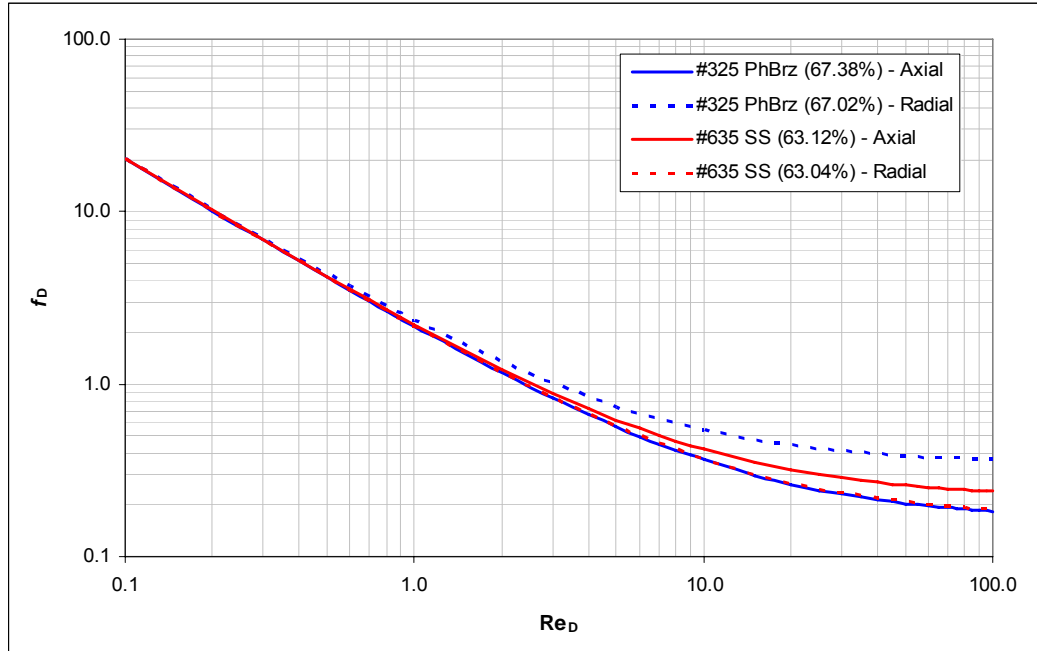


**Figure 5.6: Steady flow friction factors based on viscous resistance**

Figure 5.6 shows another interpretation of the steady flow friction factor; using a characteristic length of the inverse square root of the viscous resistances as described in section 2.2. In this interpretation, sample friction factors for the same range exhibit smaller values; however, both graphs maintain the resistive nature of each sample. Consistent with Figure 5.5, the radial #325 phosphor bronze sample was most resistive for the range of Reynolds numbers. Table 5.2 lists the range of Reynolds parameters for each sample and flow direction.

**Table 5.2: Reynolds ranges for steady flow tests**

Porous Media	Re <sub>K</sub>		Re <sub>D</sub>	
	Min	Max	Min	Max
Axial Samples				
#325 Phosphor Bronze (67.38%)	1.38	14.88	2.05	22.08
#635 Stainless Steel (63.12%)	0.18	4.13	0.28	6.54
Radial Samples				
#325 Phosphor Bronze (67.02%)	0.08	4.32	0.13	6.44
#635 Stainless Steel (63.04%)	0.02	0.95	0.03	1.50

The steady flow friction factor formulations have direct applications of modeling flow through cryocooler component structures; however, their relevance can be generalized to any system in which helium steadily flows through material of this type. Similar geometric characteristics must be taken into account such as porosity, aspect ratio and packing orientation to accurately model the complete fluid behavior.

## 5.2 Pressure Dependence Study

Another experimental investigation was carried out to measure the effect of average pressure on hydrodynamic resistance parameters relevant to steady axial flow. Multiple regenerator filler materials were tested at three discrete supply pressures; 300 psig (2.07 MPa), 400 psig (2.76 MPa) and 500 psig (3.45 MPa). The four samples tested included stacked screens of #325 stainless steel, #400 stainless steel, sintered #400 stainless steel and stainless steel metal foam. The experimental setup and procedure was identical to that explained for the steady axial flow case in section 3.2; however, the associated sample geometry and axial housing section were slightly different. These alterations of axial sample geometry are summarized in Table 5.3 along with important filler details. Details such as wire diameter, pore size and mesh thickness are not applicable to the #400 stainless steel sintered mesh because during the fabrication

process, modular stacks of screens are melted together creating a non-uniform matrix structure. Similarly, the metal foam sample is manufactured through casting techniques that yield irregular pore configurations.

**Table 5.3: Pressure dependence study axial sample details**

Porous Media	Sample Geometry		Mesh Geometry			Measured Porosity [-]
	Dia [mm]	Length [mm]	Wire Dia [micron]	Pore Size [micron]	Thickness [micron]	
#325 Stainless Steel	7.938	38.1	35.6	43	71.1	0.6969
#400 Stainless Steel	7.938	38.1	25.4	33	50.8	0.6969
#400 Stainless Steel (Sintered)	7.938	38.1	N/A	N/A	N/A	0.6165
Stainless Steel Foam	7.938	38.1	N/A	N/A	N/A	0.5547

A schematic of the experimental steady axial flow test setup used for the pressure dependence study can be viewed in Appendix E.2. Like the axial test section design used for the #324 phosphor-bronze and #635 stainless steel samples, the test sample and housing was designed with an aspect ratio of 4.8 to produce a predominately axial flow regime and the computer methodology for characterizing the mesh fillers assumes isotropic flow resistances. Complete experimental and simulation test geometry is listed as grid vertices in Appendix E.3.

In each steady axial flow test run, the system was closed and charged to the particular supply pressure as indicated by the pressure regulator. Flow of research grade helium was modulated through the system and data was recorded for a range of mass flows. Multiple test runs were performed for each sample at the three distinct supply pressures, providing pressure drops for discrete mass flow rates. In order to avoid large variations in the mean pressure during experiments with each sample, the maximum axial pressure drop across the test section was constrained to approximately 0.69 MPa (100

psi). Therefore, the average pressure in the test section can deviate no more than 50 psi during any test run.

All test runs are performed at room temperature where the working fluid is considered isothermal and the viscosity is assumed to be a constant. Hydrodynamic parameters of the porous samples are determined through the solutions process explained in section 4.2. Results are reported by the nominal supply pressure set by the regulator. Figure 5.7 through Figure 5.10 display the axial pressure drops versus mass flow rate for the four tested regenerator samples at three average pressures. Discrete experimental data points are superimposed with 5<sup>th</sup> order polynomials created from representative data points predicted by the simulation.

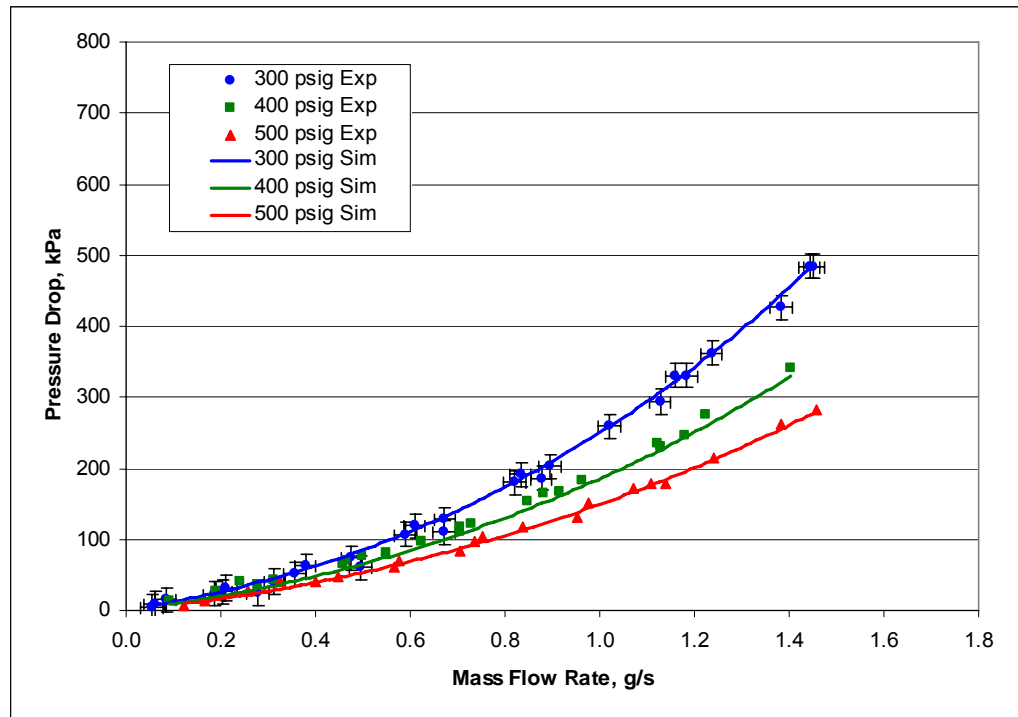


**Figure 5.7: #325 stainless steel (69.69%) pressure plot**

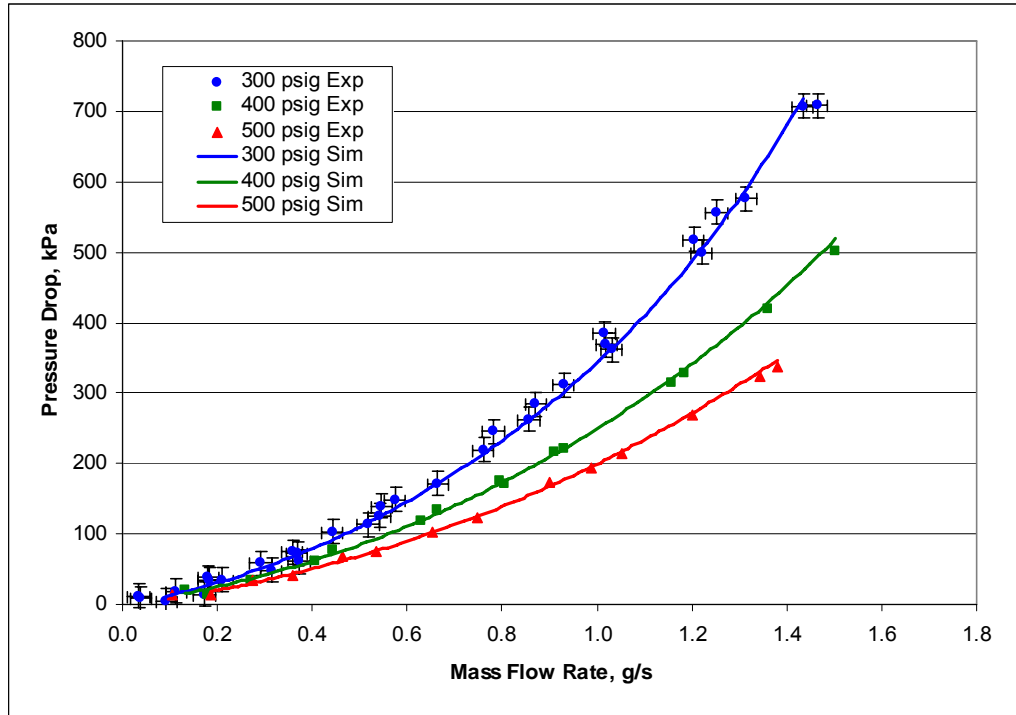


**Figure 5.8: #400 stainless steel (69.69%) pressure plot**

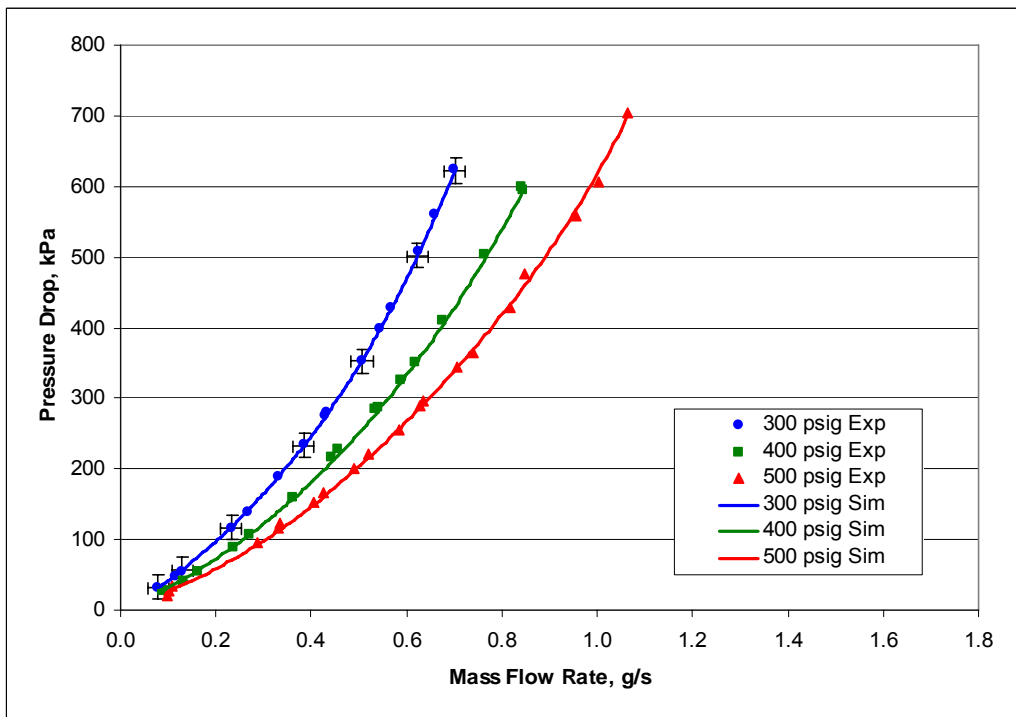


**Figure 5.9: Sintered #400 stainless steel (61.65%) pressure plot**

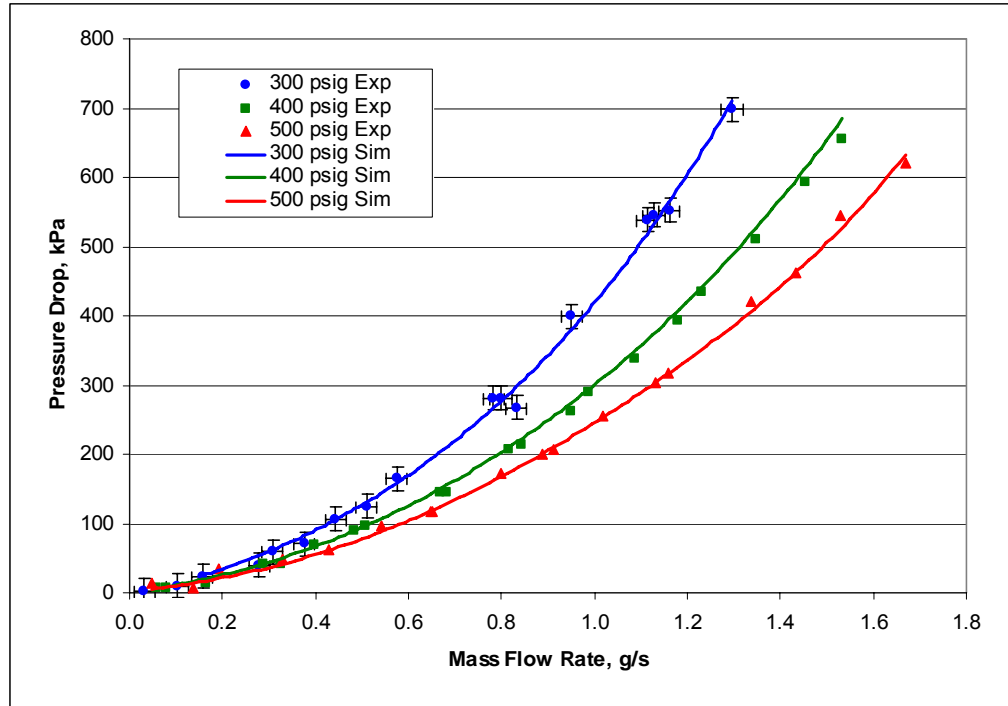


**Figure 5.10: Metal foam (55.47%) pressure plot**

Helium superficial velocity (Darcy velocity) through the porous samples covered a range from 0.2 to 19 m/s while the mass flow rates ranged from 0.032 g/s to 1.668 g/s with pressure drops across the test section limited to 0.69 MPa. All test runs were found to be well repeatable and uncertainties were relatively small when compared to the pressures changes exhibited across the range of flow rates.

Sample results show three unique empirical data curves for the separate supply pressures. For a given mass flow rate, axial pressure drops are increased as the average pressure is decreased. This comes from the ideal gas relationship of density and pressure and the resulting mass flow. At low pressures within the test section, the helium density is proportionally reduced. According to Eq. (2-14), the mass flow rate is directly proportional to the quantity of the average fluid velocity multiplied by its density for a constant cross sectional area. The volume averaged porous media governing equations

state that the pressure gradients are a function of velocity and the square of velocity. This means that for a given mass flow rate, the as pressure (and thus density) is lowered the resulting average velocity is increased, therefore producing a larger pressure drop.

Fluent simulations were performed for all four porous structures at supply pressures of 300, 400 and 500 psig. Hydrodynamic parameters were initially determined at the supply pressure which presented the greatest range of axial pressure drops and mass flow rates. These parameters were then applied to the data representing the other two supply pressures. The 300 psig supply pressure was suitable for the initial determination of flow parameters for the high-porosity samples such as the #325 and #400 stainless steel mesh fillers, whereas the maximum supply pressure of 500 psig offered the largest range of pressure drop and mass flow rate variations for more resistive materials like the #400 sintered mesh and metal foam.

Despite the differences in the flow rate to pressure drop curves for the independent supply pressures, a single set of viscous and inertial resistances for each porous structure resulted in good agreement between experimental data and simulation predictions for the three supply pressures. This suggests that steady axial flow resistances are not a function of fluid pressure. The resulting hydrodynamic parameters are summarized in Table 5.4.

**Table 5.4: Pressure independent steady axial hydrodynamic parameters**

Porous Media	Measured Porosity [-]	Viscous Resistance [m <sup>-2</sup> ]	Inertial Resistance [m <sup>-1</sup> ]	Darcy Permeability [m <sup>2</sup> ]	Forchheimer's Coefficient [-]
#325 Stainless Steel	0.6969	2.35E+10	47000	2.067E-11	0.316
#400 Stainless Steel	0.6969	2.77E+10	73000	1.753E-11	0.452
#400 Stainless Steel (Sintered)	0.6165	8.00E+10	205000	4.751E-12	0.953
Stainless Steel Foam	0.5547	2.65E+10	99000	1.161E-11	0.988

As previously done with the axial and radial #325 phosphor bronze and #635 stainless steel samples, friction factors are correlated and plotted against the appropriate Reynolds number. Measured data for the pressure dependence study covered a  $Re_K$  range of 0.11 to 5.84 but is extrapolated to cover 0.1 to 100  $Re_K$ . Sample Reynolds ranges are summarized in Table 5.5 for both characteristic length scales. Charts were also constructed for the friction factor based on sample viscous resistance.

**Table 5.5: Reynolds ranges for pressure dependence study**

Porous Media	$Re_K$		$Re_D$	
	Min	Max	Min	Max
#325 Stainless Steel (69.69%)	0.25	6.84	0.36	9.82
#400 Stainless Steel (69.69%)	0.14	6.56	0.21	9.41
#400 Stainless Steel (Sintered) (61.65%)	0.18	2.69	0.28	4.37
Stainless Steel Foam (55.47%)	0.11	5.84	0.20	10.53

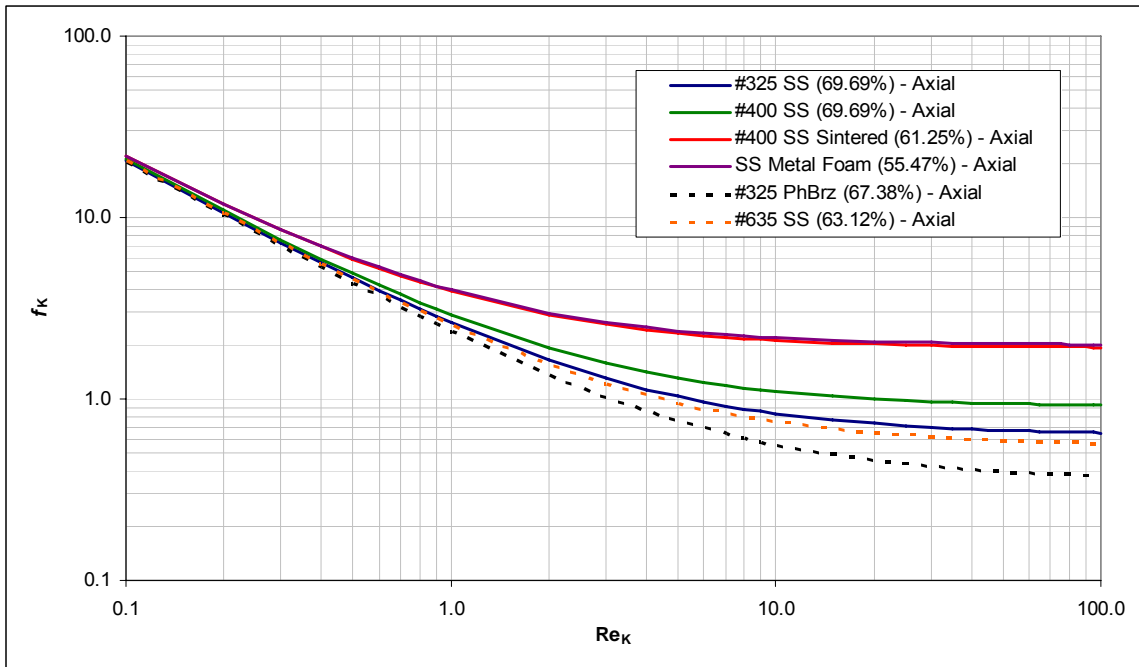


**Figure 5.11: Steady axial flow friction factors based on Darcy permeability**

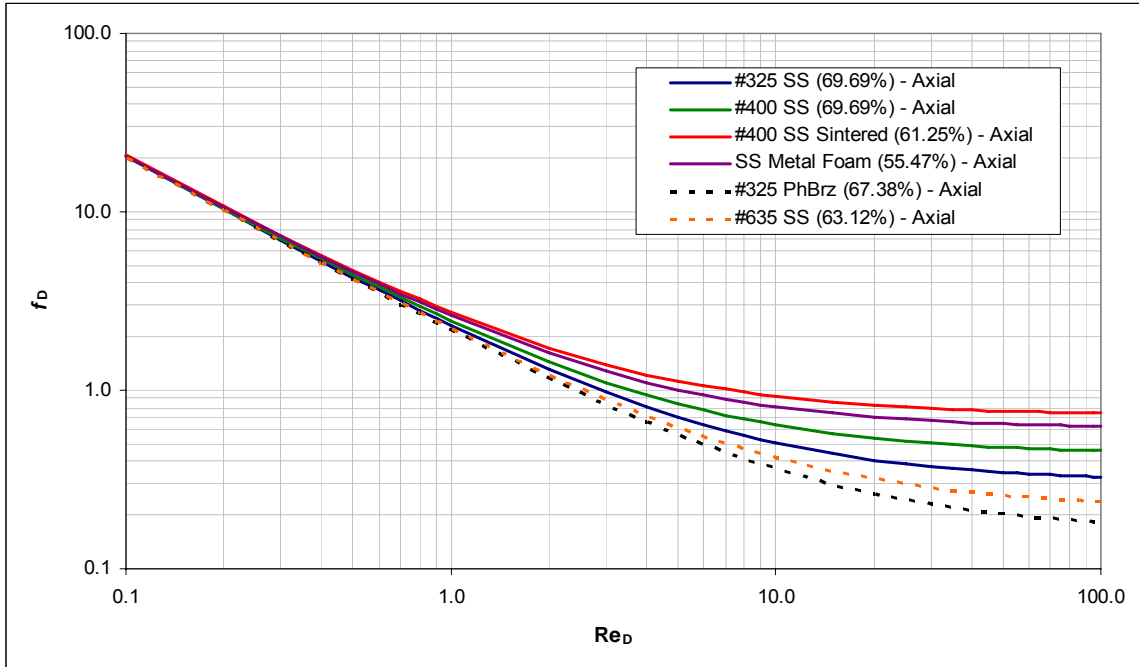


**Figure 5.12: Steady axial flow friction factors based on viscous resistance**

Results of the non-dimensional analysis of steady axial flow samples prove what intuition would suggest. More porous structures like the #325 and #400 stainless steel samples are less resistive than less porous structures like the sintered #400 stainless steel and metal foam samples. These differences are more apparent at higher flow rates where inertial effects are more prominent. The #325 phosphor bronze and #635 stainless steel materials proved to be the least resistive samples.

This insensitivity of the hydrodynamic parameters to average pressure is in contrast to the observation suggested in a previous investigation [Clearman (2007, [6])], where steady axial flow resistances were established for a single regenerator filler at four distinct supply pressures; 300 psig (2.07 MPa), 350 psig (2.41 MPa), 400 psig (2.76 MPa) and 500 psig (3.45 MPa). A review of the experimental data of Clearman (2007, [6]), however, presented substantial pressure drops ranging from 13.8 to 2,113 kPa across

the porous media with fluctuations in average pressure amounting to over 1.0 MPa. Without a fine limit on the change in pressure, it is difficult to categorize porous hydrodynamic parameters based upon average pressure. These large pressure variations evidently make it difficult to unambiguously separate frictional pressure drop from other pressure drop terms resulting for example from gas compressibility and potential small temperature variations. With the total pressure drop limited to 0.7 MPa in this study, this ambiguity is relatively insignificant.

### **5.3 Oscillatory Flow Results**

The #325 phosphor-bronze and #635 stainless steel samples were also tested under conditions of oscillating flows. Oscillatory experimentation was implemented in both the axial and radial flow directions over a frequency range of 50 to 200 Hz at 25 Hz intervals at charge pressures of 2.86 and 3.55 MPa. The same axial and radial test samples and appropriate housing units that were employed in the steady flow analysis were also applied for oscillatory cases, rendering the fluid motion within the porous sample predominately one-dimensional. Experimental measurements recorded FFT series representations of pressure waveforms on either side of the porous segment at P1 and P2 locations, respectively positioned on the compressor side and closed end of the test section. CFD code modeled the oscillatory flow test section and its vicinity by applying a periodic pressure boundary condition obtained from experimental data on the compressor side of the system.

Initial viscous and inertial resistances were applied to the porous region of the model and the simulation was run for ten cycles. Monitors sampled the dynamic pressures at the P1 and P2 locations at discrete time steps. The resulting waveforms were

characterized using amplitude and phase angle, then graphically compared to the experimental FFT representations. Hydrodynamic parameters of the model's porous section were iteratively adjusted until agreement was achieved between experimental and simulation pressure profiles at the location P2. Resistance parameters were manually adjusted based upon the error generated through post-processing. A unique set of resistances were determined which satisfied the range of tested frequencies.

The viscous resistance term is first ascertained at 50 Hz low flow conditions where input (P1) pressure amplitudes are just large enough to provide a viable signal. Flow in this regime can be considered Darcy flow where viscous effects dominate and inertial effects are considered negligible. For this low flow case, only the viscous resistance term is iteratively solved for at these low flow conditions while the inertial resistance is fixed at zero. Several applications of this process are shown below in Figure 5.13 and Figure 5.14 for the axial and radial #635 stainless steel mesh filler at the large charge pressure.

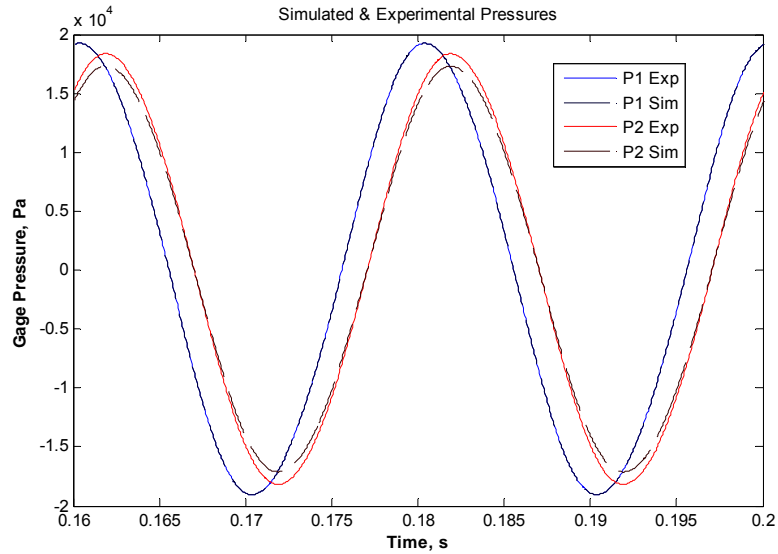


**Figure 5.13: #635 stainless steel axial flow pressure plots at 50 Hz low flow conditions (3.51 MPa)**

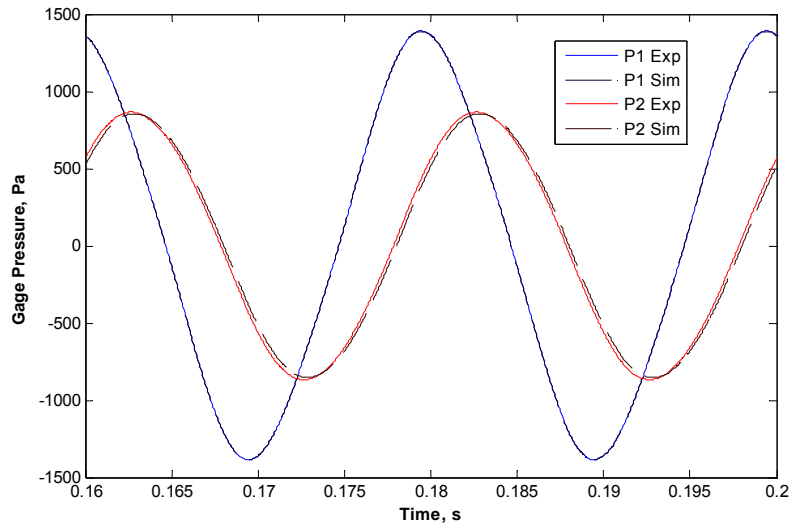


**Figure 5.14: #635 stainless steel radial flow pressure plots at 50 Hz low flow conditions (3.44 MPa)**

The figures above depict the experimental waveforms and simulated dynamic pressures at the P1 and P2 locations. Several observations are readily apparent in these plots. Model and empirical waveforms at P1 are shown to be identical as the CFD code

utilized experimental data for the P1 boundary condition. It is also clear that the P1 pressure signals are lagged by the signals at P2 which also exhibit smaller amplitudes in these cases. Parameter determination aimed to match the simulated and experimental pressures at P2 with respect to their amplitude and phasing. When comparing simulation prediction to experimental results, the axial and radial #635 stainless steel low flow cases shown above have errors in P2 amplitude of 1.06 and 0.01 kPa, respectively with phasing discrepancies of 0.157 and 0.063 rad.

Although the P2 amplitudes of the experimental and simulated data are not exact, the phase shift relative to P1 is nearly identical. Once the experimental and simulated phase and pressure amplitude at P2 are in accord, the viscous term is then set and the inertial term can be solved for at higher flow conditions. Slight amendments to the viscous term were implemented to offer better agreement for higher flow cases across the range of operating frequencies.

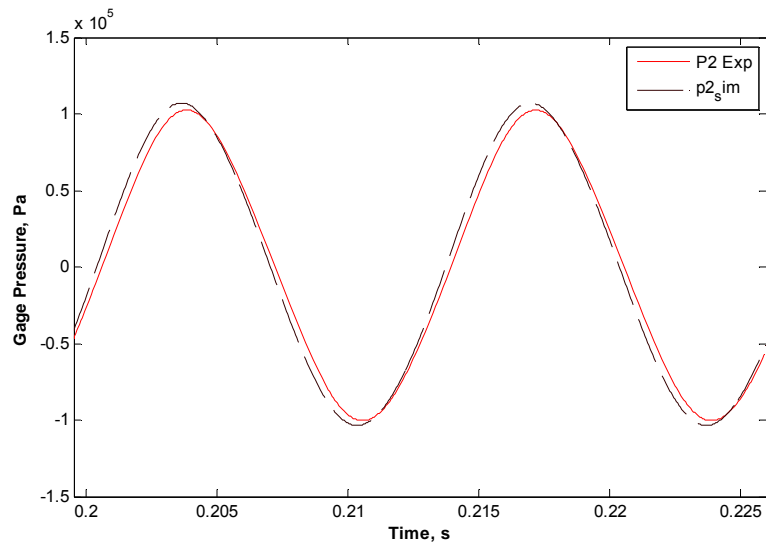


**Figure 5.15: #635 stainless steel axial flow pressure plots at 75 Hz (3.54 MPa)**

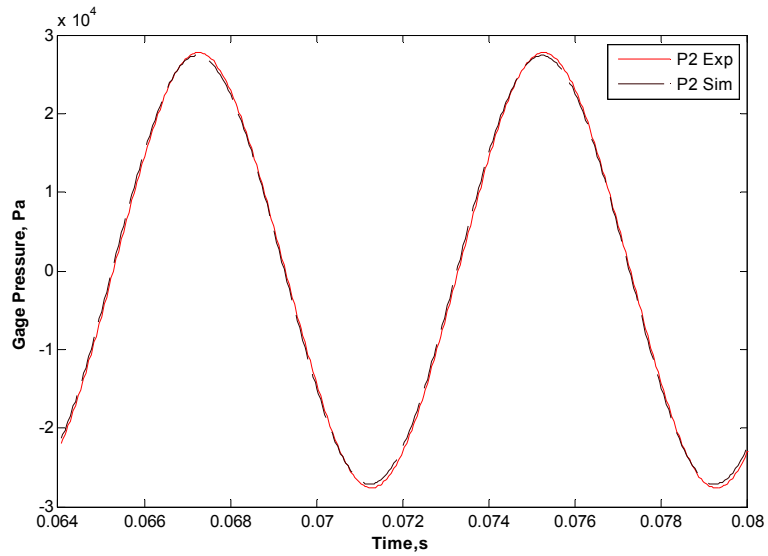


**Figure 5.16: #635 stainless steel axial flow pressure plots at 125 Hz (3.58 MPa)**

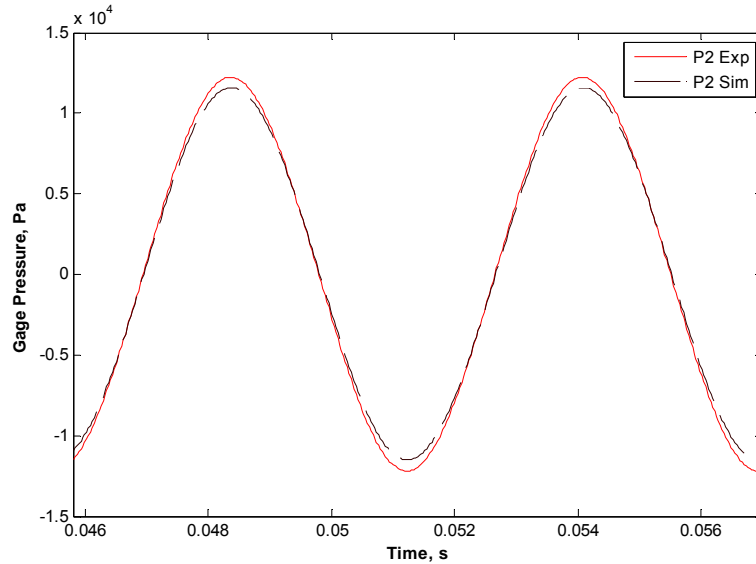


**Figure 5.17: #635 stainless steel axial flow pressure plots at 175 Hz (3.61 MPa)**

A series of pressure comparison plots of P2 are shown in Figure 5.15 through Figure 5.17 for the #635 stainless steel axial flow case at frequencies of 75, 125 and 175 Hz and at charge pressures of approximately 3.6 MPa. As mentioned in section 3.4,

compressor response at off resonant conditions generated diminished pressure amplitudes for higher test frequencies. This concept is seen in the amplitudes of the P2 comparison plots and axes are scaled accordingly. Good agreement between experimental and simulated results is exhibited with viscous and inertial resistances of  $9.95E10 \text{ m}^{-2}$  and  $40,000 \text{ m}^{-1}$  for the #635 stainless steel axial case at a charge pressure of 3.5 MPa across the entire frequency band. This series produced an average error in P2 simulated pressure amplitude of 3.6% relative to experimental data with a maximum deviation of 6.6%. Average variation in simulated phase angle was 0.043 rad or 2.5 deg with a maximum discrepancy of 6.3 deg.

The set of oscillatory flow hydrodynamic parameters used for the #635 axial flow series at 3.6 MPa demonstrated excellent agreement for the same sample at a charge pressure of 2.9 MPa. Results of this application are displayed in Figure 5.18 and Figure 5.19. Average deviations of 3.3% in simulated pressure amplitudes and 2.0 deg were reported.

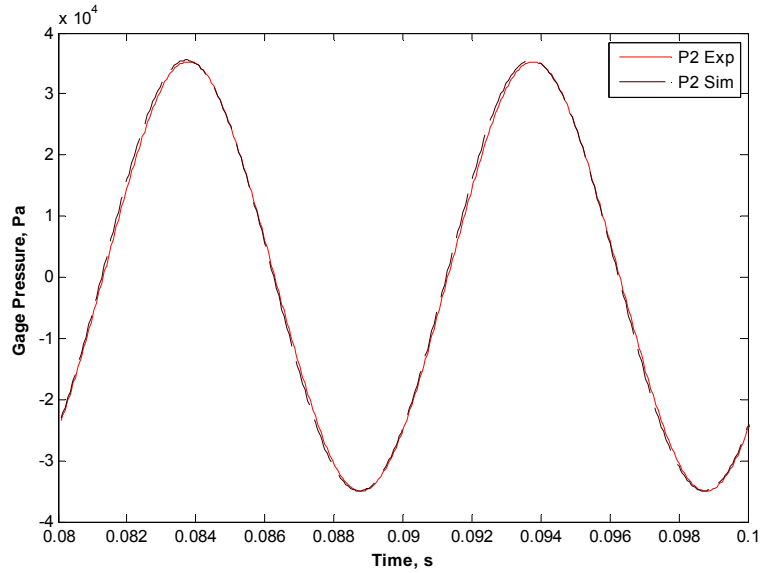


**Figure 5.18: #635 stainless steel axial flow pressure plot at 100 Hz (2.87 MPa)**

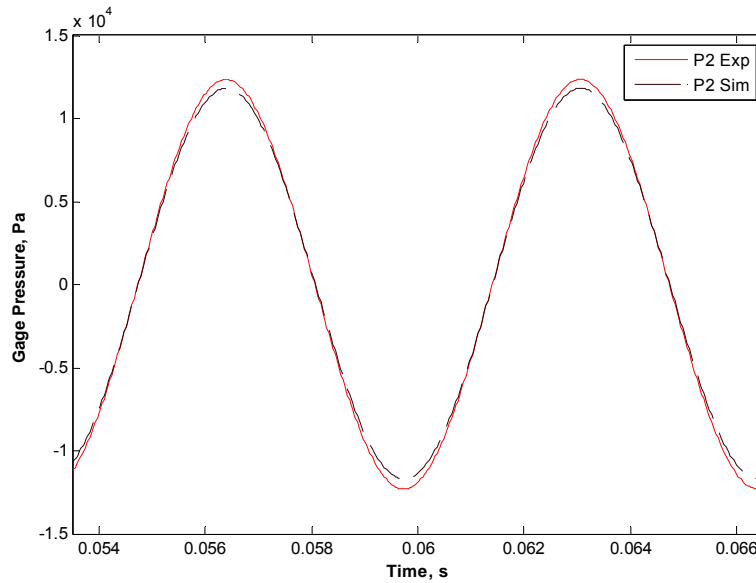


**Figure 5.19: #635 stainless steel axial flow pressure plot at 150 Hz (2.89 MPa)**

It is unclear how the sample viscous and inertial resistances would affect the resulting simulated pressure amplitude and phase lag at P2. Rather, each resistance term had a combined effect on the predicted amplitude and phase. This relationship is best

explained when the harmonic signal is broken into a segmented pressure rise from zero to its peak. In this sense it can be viewed as a one-dimensional steady flow problem with a quadratic correlation with the hydrodynamic resistances. The viscous resistance commands a linear relationship between flow rate and pressure drop while the inertial resistance has a squared correlation with flow rate. By increasing the viscous resistance coefficient of the porous region, a decrease in pressure would consistently be seen across that rise; generating a smaller P2 amplitude and larger phase lag with respect to P1. Conversely, by increasing the inertial resistance coefficient, the rate at which the pressure rises would be diminished. This change would also produce a slight shift in phase. Note that the mass flow rate or velocity within test section and at sensor locations most likely will not be in phase with the pressure. Direct interpretation of periodic pressure drops must be performed with time-dependent harmonic flow rates.

The oscillatory radial flow testing with the #635 stainless steel sample produced good waveforms at the P2 locations across the range of operating frequencies. Good agreement was displayed between experimental and simulation predictions for cases with an average charge pressure of 2.9 MPa when applying viscous and inertial resistances of  $1.05E11 \text{ m}^{-2}$  and  $120,000 \text{ m}^{-1}$ , respectively. Plots utilizing these parameters can be viewed in Figure 5.20 and Figure 5.21.

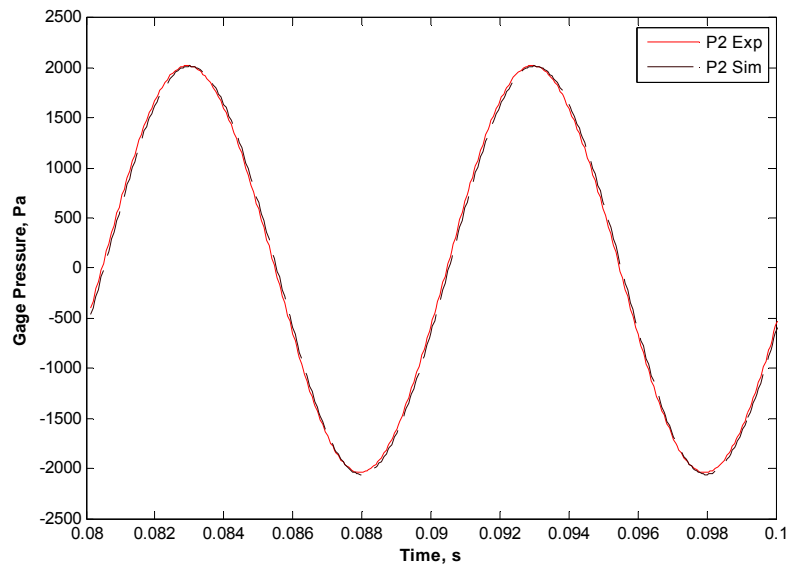


**Figure 5.20: #635 stainless steel radial flow pressure plot at 100 Hz (2.88 MPa)**

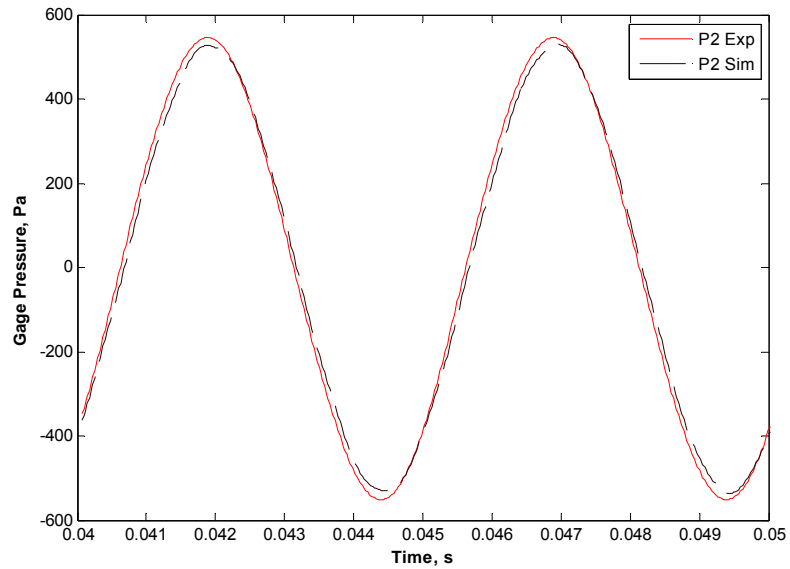


**Figure 5.21: #635 stainless steel radial flow pressure plot at 200 Hz (2.84 MPa)**

Similar parameters with a slightly larger viscous resistance but equal inertial resistance demonstrated exceptional agreement between experimental results and

simulation predictions at P2. Hydrodynamic parameters of  $1.11E10 \text{ m}^{-2}$  and  $120,000 \text{ m}^{-1}$  yielded average simulation errors of 4.4% in amplitude and 1.6 deg in phase for the #635 stainless steel radial sample at an average charge pressure of 3.6 MPa.

During experimentation, it was observed that the majority of #325 phosphor bronze cases across the range of frequencies exhibited pressure amplitudes at the P2 location which were larger than the inlet pressure amplitude. It was originally thought that any constructive acoustical interference seen in testing could be solved and demonstrated through CFD simulations. After processing the results, it was later realized that the standard axisymmetric models governing the fluid behavior would not always produce the amplified pressures at P2. It may be possible that through the use of three dimensional simulations of the entire closed system and the incorporation of acoustical governing equations and the associated boundary conditions that this phenomenon could be consistently replicated; however, it was out of the scope of this investigation.

This amplified signal at P2 could be matched through phase angle but not in amplitude. Several #325 phosphor bronze oscillatory axial and radial flow cases at increased operating frequencies, however, did provide viable P2 amplitudes which could be matched in both amplitude and phase. Viscous and inertial resistance parameters of  $1.70E10 \text{ m}^{-2}$  and  $50,000 \text{ m}^{-1}$  demonstrated tolerable agreement for the range of axial flow #325 phosphor-bronze sample tests at both charge pressures. Plots of this application are shown in Figure 5.22 and Figure 5.23.

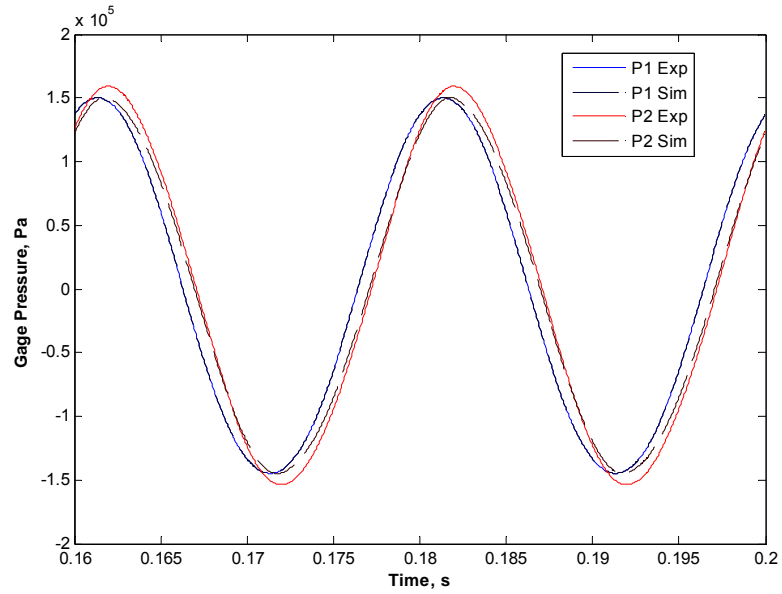


**Figure 5.22: #325 phosphor bronze axial flow pressure plot at 50 Hz (3.51 MPa)**

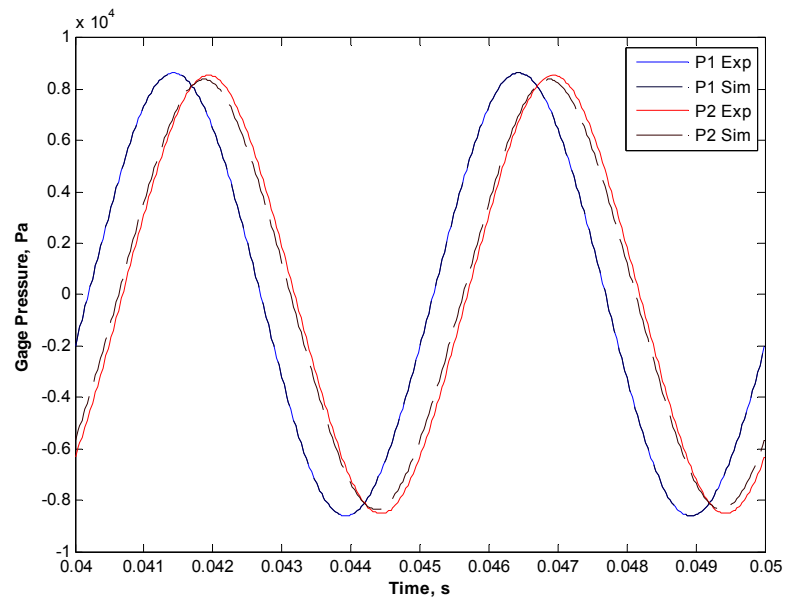


**Figure 5.23: #325 phosphor bronze axial flow pressure plot at 200 Hz (2.88 MPa)**

Figure 5.22 and Figure 5.23 present simulated and experimental pressures for the #325 phosphor bronze axial flow sample tests. The pressure amplitudes at P1 and P2

locations show how little change in pressure was exhibited for this case. This reduced resistive element enabled the constructive acoustical phenomena to occur on the closed side of the system in the form of enlarged pressure amplitudes at P2 (Figure 5.22). Only at frequencies of 175 and 200 Hz was this resonant behavior not observed.

Acoustical interference was also seen in many of the #325 phosphor-bronze oscillatory radial flow experiments. In some cases the CFD code was able to generate an amplified pressure signal at P2; however, this behavior is not conducive for parameter determination. Just like its axial counterpart, an average set of parameters was determined which produced satisfactory agreement for most cases. Viscous and inertial resistances of  $2.90E10 \text{ m}^{-2}$  and  $50,000 \text{ m}^{-1}$  were applied to the simulated radial porous media at each charge pressure and several resulting plots are illustrated in Figure 5.24 and Figure 5.25.

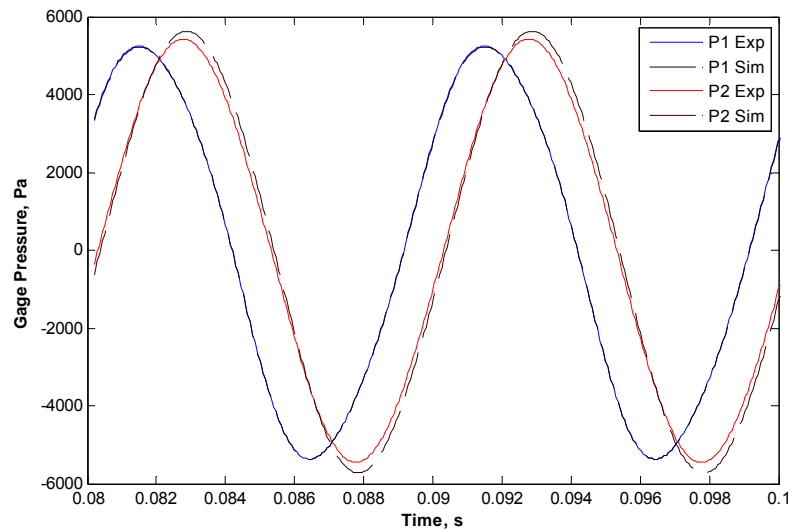


**Figure 5.24: #325 phosphor bronze radial flow pressure plot at 100 Hz (2.82 MPa)**

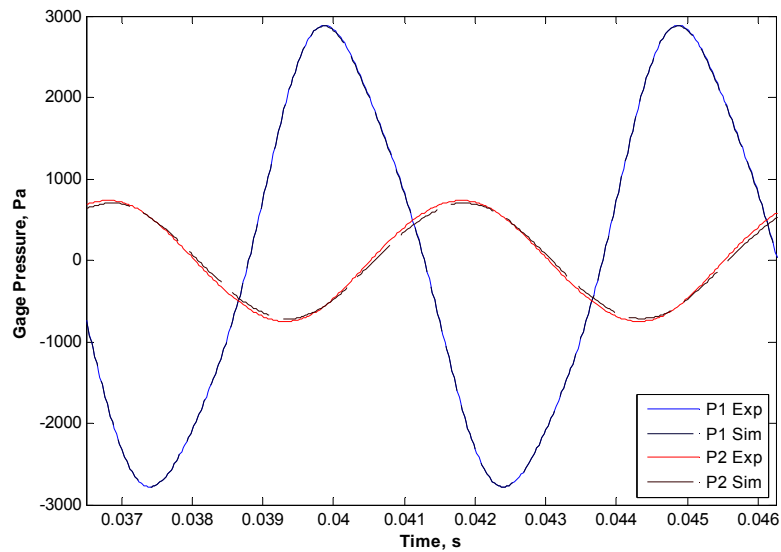


**Figure 5.25: #325 phosphor bronze radial flow pressure plot at 150 Hz (3.44 MPa)**

The iterative solution method produced a unique set of oscillatory resistance parameters for each sample material, flow direction, and charge pressure that satisfied all investigated frequencies. Differences between simulated and experimental pressure amplitude at P2 was calculated as a percentage difference based upon the experimental amplitude at P2. For all oscillatory flow pressure plot matching, the average error for simulated pressure calculation at P2 was 3.7% and 3.5% of the experimental pressure for the axial and radial cases, respectively. Average deviations in simulated phase angle between the pressures recorded at P1 and P2 were 1.48 deg and 1.43 deg for axial and radial tests. The average oscillatory flow hydrodynamic resistances, Darcy permeabilities and Forchheimer's coefficients are summarized in Table 5.6. A chart of the experimental and simulated pressure amplitudes and phase angles including the simulated errors for all oscillatory flow cases can be found in Appendix C.3 and C.4.

**Table 5.6: Average oscillatory flow sample hydrodynamic parameters**

Porous Media	Charge Pressure [MPa]	Viscous Resistance [m <sup>-2</sup> ]	Inertial Resistance [m <sup>-1</sup> ]	Darcy Permeability [m <sup>2</sup> ]	Forchheimer's Coefficient [-]
Axial Samples					
#325 PhBrz (67.38%)	2.9	1.70E+10	50000	2.672E-11	0.422
#325 PhBrz (67.38%)	3.6	1.70E+10	50000	2.672E-11	0.422
#635 SS (63.12%)	2.9	9.50E+10	40000	4.194E-12	0.163
#635 SS (63.12%)	3.6	9.50E+10	40000	4.194E-12	0.163
Radial Samples					
#325 PhBrz (67.02%)	2.9	2.90E+10	50000	1.549E-11	0.327
#325 PhBrz (67.02%)	3.6	2.90E+10	50000	1.549E-11	0.327
#635 SS (63.04%)	2.9	1.05E+11	120000	3.785E-12	0.466
#635 SS (63.04%)	3.6	1.11E+11	120000	3.596E-12	0.454

Results of the oscillatory flow parameterization suggest that periodic flow hydrodynamic parameters may be insensitive to charge pressure. Three of the four oscillatory flow directional samples exhibited good agreement for both charge pressures of 2.9 and 3.6 MPa using a single set of hydrodynamic parameters with the exception being the #635 stainless steel radial cases. However, this discrepancy in porous media resistance is relatively minute and any conclusions concerning the effect of pressure on oscillatory flow hydrodynamics requires further verification.

It is beyond question that the #325 phosphor bronze and #635 stainless steel sample resistance parameters are very different for the two orthogonal flow directions. Hydrodynamic behavior is also altered when these porous structures are subjected to dissimilar flow fields; as being either predominately steady, one-dimensional flow or primarily steady-state oscillating flow. These differences are contrasted through sample plots of the directional oscillatory and steady flow friction factors. Figure 5.26 shows the four independent parameters determined for the #325 phosphor bronze sample while Figure 5.27 presents the friction factors for the #635 stainless steel material filler.

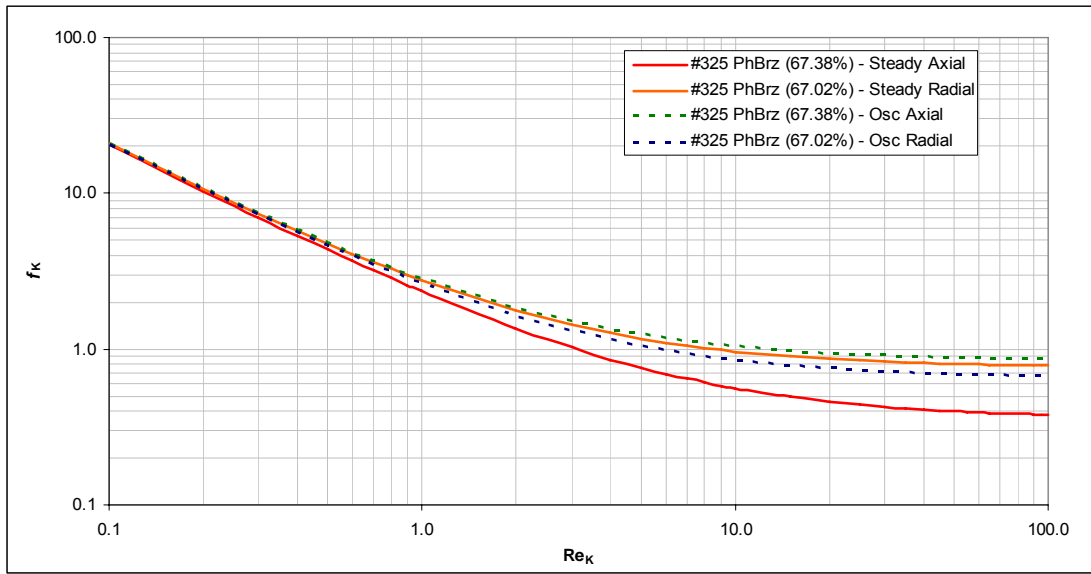


**Figure 5.26: Friction factor comparison for #325 phosphor bronze sample**

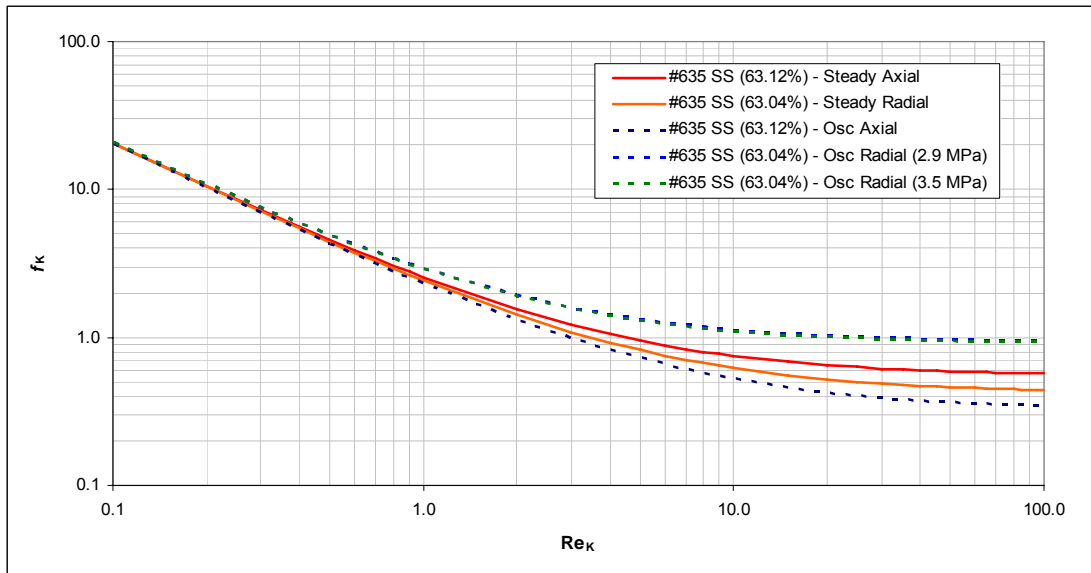


**Figure 5.27: Friction factor comparison for #635 stainless steel sample**

The friction factor correlations offer direct comparison of resistance parameters over a range of flow parameters. At low flow conditions in the range of 0.1 to 1.0  $Re_K$ , these differences are negligible; however, at larger flow rates, for Reynolds numbers

greater than 10.0, these dissimilarities are amplified. These plots reinforce the concepts of anisotropy and the unique nature of flow conditions on the material hydrodynamics.

## 6 CONCLUDING REMARKS

Anisotropic hydrodynamic parameters of stacked screens of #325 phosphor bronze and #635 stainless steel were determined using a CFD-assisted methodology. Using specially designed test sections which rendered a predominately one-dimensional flow regime within the porous media, measurements were made in the radial and axial directions under steady and oscillatory flow conditions. Experimental test setups for steady flow cases included static pressure transducers and a mass flow meter; producing pressure drops over a range of discrete mass flow rates. Oscillatory flow tests utilized a closed setup powered by a tactical compressor and included dynamic pressure transducers to measure pressure waveforms on either side of the porous media. Periodic flow cases were performed over a frequency range between 50 and 200 Hz at two different charge pressures; conditions which are applicable to miniature cryocooler operation. Anisotropic parameters were also used to calculate sample directional Darcy permeabilities and directional Forchheimer's inertial coefficients.

The fluid control volume within the experimental test section and its vicinity were modeled using a CFD code. Pressure and flow rate measurements obtained through testing were input as boundary conditions. The model's porous regions utilized volume averaged governing momentum equations which include additional sink terms in the form of the viscous and inertial resistance coefficients to predict the hydrodynamic behavior with respect to the porous structure. Flow is predominately one-dimensional within each test section, so isotropic model resistances were applied. It is these closure

parameters of the simulated porous region which are iteratively changed until there is agreement is reached between experimental and simulated results.

Steady axial and radial flow measurements produced unique viscous and inertial resistances which minimized the error between polynomial curve fits of the experimental data and simulated predictions. Large pressure drops were generated by the steady axial flow setup, affording a wide range of data utilized for parameter determination. On the other hand, the radial test section only produced minor changes in pressure. These small radial pressure drops were on the order of the sensor's uncertainty and the resulting hydrodynamic resistances are subject to error. A more precise parameterization of the steady radial flow samples would involve modifying the test apparatus. Several options include utilizing different static pressure transducers with greater accuracy or fabricating new mesh screens with an increased outer diameter and enlarged housing unit. A larger distance traversed by the fluid within the porous structure creates increased pressure losses.

Steady flow results also reiterated the importance of anisotropic hydrodynamic resistances. Although inertial resistances seemed to follow a set range of values, viscous resistances established for the radial cases were nearly an order of magnitude larger than those found for the axial direction. Porous media simulations in which multidimensional effects are significant must apply the appropriate directional resistances for accurate analysis. There is reasonable confidence that these resistance parameters determined in this thesis may be applied to any general simulation which utilizes similar porous structures at designated parameter ranges. However, caution must be exercised when doing so, as those materials which are being modeled may vary in packing orientation,

porosity and aspect ratio from the tested samples. These inconsistencies may also lead to simulation errors.

The effect of average pressure on hydrodynamic parameters relevant to steady axial flow was investigated for several regenerator filler materials including stacked screens of #325 stainless steel and #400 stainless steel mesh, sintered #400 stainless steel mesh and a stainless steel metal foam. Measurements were obtained at three distinct supply pressures and the maximum pressure drop across the porous material was limited to clearly categorize the average pressure of a particular data set. Results showed that a single unique set of viscous and inertial resistances for each sample exhibited good agreement for the separate pressures. The insensitivity of the hydrodynamic parameters to pressure is encouraging, and provides us with reasonable confidence that the derived closure parameters can be applied to conditions outside the range of experimental data. Similar investigations to examine the effect of pressure on flow resistance parameters in radial flow, and more importantly under oscillatory flow conditions, are recommended.

A previous investigation by Clearman et al. (2008, [7]) analyzed the uniqueness of flow parameters and the sensitivity of the simulated predictions on these parameters. This study utilized a single mesh filler under steady axial flow conditions and multiple combinations of viscous and inertial hydrodynamic parameters were applied to the porous region. The resulting simulated pressure curves were compared with experimental data and simulated error was calculated through an average percentage. It was found that the viscous resistance may be varied by about  $\pm 3\%$  and the inertial resistance varied by  $\pm 5\%$  without appreciably changing the accuracy of the simulated predicted pressure

curve. Although no such assessment was performed on results from this thesis, it sheds light on the precision of steady flow resistance parameters.

An average set of axial and radial oscillatory flow hydrodynamic parameters were also determined for the #325 phosphor bronze and #635 stainless steel samples at two distinct charge pressures covering a range of operating frequencies. Results indicate that oscillatory flow resistances may also be independent of pressure. A slight dependence of these parameters on pressure was observed for the radial flow #635 stainless steel case. Directional resistances ascertained for oscillatory flow tests showed large discrepancies from their steady flow counterparts. Therefore, when modeling porous media exposed to periodic flow regimes, the appropriate structure oscillatory flow hydrodynamic parameters should be employed to provide accurate results.

Several aspects of the oscillatory flow test setup could be altered to provide improved sample characterization. First of all, the compressor used for powering the system had a limited response across the range of test frequencies. The pressure wave generator's resonant conditions for the oscillatory setups were observed to be around 50 Hz; however, parameters must be obtained for applications at higher frequencies. The diminished performance at off-resonant conditions limits the attainable flow rates and fluid velocities. Reduced flow rates decreases the significance of the viscous and inertial resistances within the subsequent volume averaged governing equations. As a result, determining the sample hydrodynamics at low flow conditions may prove to be inaccurate. It may be possible to perform these oscillatory flow tests using a different compressor or a series of compressors with suitable response across the range of

operating frequencies, although the commercial availability of such a device has yet to be seen.

Another issue encountered in the oscillatory flow test setups was acoustical interference. At discrete operating frequencies and charge pressures, the oscillatory flow experimental setups would exhibit some acoustical behavior resulting in pressure amplitudes on the closed end of the porous material which were greater than those measured on the compressor side. This constructive interference was the result of resonant excitation occurring within sensor's chamber bound by the porous material. It is unclear whether the CFD software can accurately model acoustics without applying the appropriate acoustical governing equations and boundary conditions. A solution to this issue would be to employ a modular experimental test rig which would drive out any acoustical phenomena from the tested frequencies. This design assembly could make use of tunable buffer volumes which would function to avoid any constructive interference while minimizing void space.

The iterative solution process used for steady flow analysis was fairly proficient as simulated data curves could be directly compared to empirical results in a matter of minutes. However, oscillatory flow parameterization was grossly inefficient. A novel computational methodology beyond the simple graphical interpretations could improve the accuracy and effectiveness of the oscillatory flow parameter determination. A two dimensional optimization routine would have to be created which would automatically minimize the difference between simulated and experimental pressure amplitudes and phases by intelligently adjusting the porous sample resistances. This method would have to interface directly with the CFD code and could be applied as a user defined function.

The directional oscillatory flow hydrodynamic resistance parameters determined in this study will be directly applied to simulated porous regions of miniature cryocooler models. The #635 stainless steel sample parameters are utilized for predicting fluid behavior within the regenerator while the #325 phosphor-bronze sample parameters are employed in the heat exchangers. With accurate knowledge of constituent material hydrodynamics, CFD simulations can provide detailed performance predictions and system analysis. Such a tool can offer critical design information and optimization.

A previous investigation by Cha et al. (2007, [5]) studied the impact of uncertainties associated with regenerator hydrodynamic closure parameters on the performance of an ITPTR. A parametric test was done on a single CFD model utilizing ten different materials for the system's porous regenerator matrix. The models employed oscillatory and steady flow hydrodynamic closure relations and the systems were run to near steady periodic conditions. Results showed that steady flow resistances can produce no load temperatures which can deviate up to 20 K from their oscillatory flow counterparts. Other factors such as the regenerator's material specific heat also have a profound effect on system performance.

The tested filler materials have direct application to cryocooler components. All hydrodynamic tests were performed at ambient temperatures; however, the systems which they model are subjected to a range of conditions from near ambient to cryogenic. It is recognized that the applicability of these parameters to cryogenic conditions needs experimental confirmation.

It has been shown in this study and in others that directional oscillatory flow parameters can be different from those determined for steady flow. Research has also

suggested that parameters determined for low frequency oscillation mimics results obtained for steady flow [Hsu et al. (1999, [14])]. The dependence of hydrodynamic resistances on oscillating frequency is an ongoing topic of debate. An extension to the work which has been presented in this thesis would be to analyze the frequency dependence of the directional hydrodynamic resistances. High and low flow measurements would need to be obtained at each discrete frequency with sufficient compressor response to produce clean waveforms. An equal contribution of both the viscous and inertial resistance terms would provide an accurate basis for parameter determination. This work is currently in progress and will be presented at the Cryogenic Engineering Conference in the summer of 2009.

## APPENDIX A: STEADY FLOW DATA

### A.1: Steady Axial Flow Experimental Data

#### A.1.1: #325 Phosphor Bronze - 67.38% Porosity

Mass Flow [g/s]	Static Pressure		
	P1 [kPa]	P2 [kPa]	$\Delta P$ [kPa]
0.087	2675.2	2654.5	20.7
0.117	2640.7	2620.0	20.7
0.212	2620.0	2564.9	55.2
0.343	2591.8	2475.2	116.5
0.452	2566.2	2378.7	187.5
0.620	2531.1	2213.2	317.9
0.779	2504.2	2020.2	484.0
0.911	2482.1	1807.8	674.3
0.117	2655.2	2626.9	28.3
0.290	2600.7	2502.8	97.9
0.383	2591.1	2447.7	143.4
0.459	2558.7	2364.9	193.7
0.546	2538.7	2282.2	256.5
0.614	2524.9	2206.3	318.5
0.677	2513.2	2137.4	375.8
0.751	2499.4	2040.9	458.5
0.827	2485.6	1930.5	555.0

#### A.1.2: #635 Stainless Steel - 63.12% Porosity

Mass Flow [g/s]	Static Pressure		
	P1 [kPa]	P2 [kPa]	$\Delta P$ [kPa]
0.053	2675.2	2640.7	34.5
0.141	2654.5	2558.0	96.5
0.264	2626.9	2399.4	227.5
0.343	2607.6	2268.4	339.2
0.422	2598.7	2116.7	481.9
0.506	2583.5	1923.6	659.8
0.044	2654.5	2626.9	27.6
0.080	2640.7	2592.4	48.3
0.136	2633.8	2544.2	89.6
0.175	2620.0	2495.9	124.1
0.212	2618.6	2447.7	171.0
0.244	2613.1	2406.3	206.8
0.278	2609.0	2358.0	251.0
0.324	2602.8	2282.2	320.6
0.367	2595.9	2206.3	389.6
0.411	2591.1	2123.6	467.5
0.472	2584.9	1999.5	585.4
0.503	2578.7	1923.6	655.0

## A.2: Steady Radial Flow Experimental Data

### A.2.1: #325 Phosphor Bronze - 67.02% Porosity

Mass Flow [g/s]	Static Pressure		
	P1 [kPa]	P2 [kPa]	$\Delta P$ [kPa]
0.126	2706.9	2706.2	0.7
0.184	2692.4	2691.0	1.4
0.276	2670.4	2667.6	2.8
0.397	2644.2	2640.0	4.1
0.560	2608.3	2601.4	6.9
0.670	2586.2	2577.3	9.0
0.827	2558.9	2547.6	11.2
0.957	2538.7	2523.5	15.2
1.548	2444.9	2411.8	33.1
0.122	2709.0	2706.2	2.8
0.137	2702.8	2701.4	1.4
0.167	2695.2	2692.4	2.8
0.197	2700.0	2697.2	2.8
0.253	2675.2	2671.7	3.4
0.324	2657.3	2653.1	4.1
0.418	2633.1	2627.6	5.5
0.484	2618.0	2611.1	6.9
0.564	2599.3	2591.8	7.6
0.682	2576.6	2566.2	10.3
0.777	2558.7	2546.2	12.4
0.922	2533.1	2517.3	15.9
1.038	2513.2	2495.2	17.9
1.125	2496.6	2475.9	20.7
1.191	2483.5	2460.8	22.8
1.284	2463.5	2438.0	25.5
0.195	2673.8	2672.4	1.4
0.310	2634.5	2631.1	3.4
0.479	2581.4	2575.2	6.2
0.709	2529.0	2517.3	11.7
0.893	2487.0	2471.8	15.2
0.977	2466.3	2447.0	19.3
1.042	2433.9	2413.2	20.7
1.155	2395.3	2369.1	26.2
1.221	2363.5	2334.6	29.0
0.530	2611.1	2602.8	8.3
0.731	2579.3	2568.3	11.0
0.859	2548.3	2535.2	13.1
1.002	2537.3	2520.7	16.5
1.130	2522.1	2502.1	20.0
1.254	2515.2	2491.1	24.1
1.356	2498.0	2471.1	26.9

A.2.2: #635 Stainless Steel - 63.04% Porosity

Mass Flow [g/s]	Static Pressure		
	P1 [kPa]	P2 [kPa]	$\Delta P$ [kPa]
0.042	2736.5	2733.8	2.8
0.049	2725.5	2723.4	2.1
0.072	2718.6	2715.9	2.8
0.105	2708.3	2704.8	3.4
0.147	2704.1	2700.0	4.1
0.196	2692.4	2687.6	4.8
0.218	2689.7	2683.5	6.2
0.277	2680.0	2673.1	6.9
0.300	2677.9	2669.7	8.3
0.366	2667.6	2658.6	9.0
0.406	2661.4	2651.7	9.7
0.473	2652.4	2640.7	11.7
0.532	2644.2	2631.1	13.1
0.662	2626.9	2609.7	17.2
0.730	2618.0	2599.3	18.6
0.844	2600.7	2578.7	22.1
0.985	2582.8	2555.9	26.9
1.062	2573.8	2544.9	29.0
1.169	2559.3	2531.8	27.6
1.218	2554.5	2520.7	33.8
1.353	2539.4	2500.1	39.3

## APPENDIX B: UDF PRESSURE INLET BOUNDARY CONDITION

```
/*
unsteady_pressure.c
UDF for specifying a transient pressure/velocity profile boundary condition
Udf given is a sample
*/
#include "udf.h"
#define freq 150
#define M1 24176.177599
#define M2 63.074900
#define M3 92.718264
#define Phi1 -1.781290
#define Phi2 2.398692
#define Phi3 1.501484

DEFINE_PROFILE(unst_p_inlet, thread, position)
{
    face_t f;
    real t = CURRENT_TIME;
    real omega = 2*M_PI*freq;
    begin_f_loop(f, thread)
    {
        F_PROFILE(f, thread, position) =
(M1*cos(1*omega*t+Phi1)+M2*cos(2*omega*t+Phi2)+M3*cos(3*omega*t+Phi3));
    }
    end_f_loop(f, thread)
}
```

# APPENDIX C: OSCILLATORY EXPERIMENTAL DATA

## C.1: Oscillatory Axial Flow Pressure Waveform Data

### C.1.1: #325 Phosphor Bronze - 67.38% Porosity

Operating Frequency [Hz]	Charge Pressure [MPa]	P1 Location						P2 Location					
		Pressure Amplitude			Phase Angle			Pressure Amplitude			Phase Angle		
		Z <sub>1</sub> [Pa]	Z <sub>2</sub> [Pa]	Z <sub>3</sub> [Pa]	φ <sub>1</sub> [rad]	φ <sub>2</sub> [rad]	φ <sub>3</sub> [rad]	Z <sub>1</sub> [Pa]	Z <sub>2</sub> [Pa]	Z <sub>3</sub> [Pa]	φ <sub>1</sub> [rad]	φ <sub>2</sub> [rad]	φ <sub>3</sub> [rad]
50 (low)	2.84	17336.472	86.738499	188.09321	-0.425857	-1.024908	0.4870898	18439.289	92.51603	237.997	-0.584708	-1.248216	-0.161858
50	2.84	110914.81	1829.4656	909.33229	-0.568598	-1.341476	1.3395003	114719.65	1795.645	1616.981	-0.822769	-1.624895	-1.440774
75	2.85	85728.893	842.88224	941.66388	-1.199184	-2.668835	-1.083498	85459.188	779.1725	1693.085	-1.579256	-2.957974	2.292982
100	2.86	44860.351	127.29729	403.82399	-1.482928	2.5186019	-2.437729	44589.034	97.0021	927.3109	-1.909984	1.118589	1.118934
125	2.87	27501.717	82.402821	258.82494	-1.644879	2.4533432	-1.830782	27222.233	84.62083	503.8763	-2.124223	2.303025	0.451641
150	2.88	18880.253	57.437168	169.12335	-1.756874	2.0603642	2.4902432	18569.249	42.92693	330.5715	-2.294351	1.740237	-0.207366
175	2.88	13606.072	35.045127	120.21811	-1.791937	1.9546105	2.0192996	13294.033	19.39578	227.3002	-2.37632	1.469544	-0.619288
200	2.88	8570.085	18.769055	70.198325	-1.806852	1.8336795	1.5486806	8409.2601	9.20559	124.7456	-2.433347	0.795078	-0.962229
50 (low)	3.51	4044.947	49.904161	211.75933	-0.239427	-0.537751	1.2989433	4353.9309	59.06791	229.9225	-0.359587	-0.739112	0.924561
50	3.51	148692.32	2654.5054	1285.0209	-0.423192	-0.946728	1.8899351	155207.23	2701.753	2282.89	-0.658475	-1.238692	-0.922858
75	3.53	116330.13	1252.4249	1367.44	-1.176331	-2.548069	-0.887185	117551.35	1209.76	2485.131	-1.532636	-2.872386	2.475449
100	3.55	58038.413	189.91263	561.93448	-1.48156	2.1890879	-2.108169	59006.656	156.8553	1258.403	-1.868026	2.403678	1.334026
125	3.56	34878.319	76.067239	335.7523	-1.669878	2.2975534	-3.005602	35562.742	94.15594	733.7405	-2.097942	2.326273	0.54124
150	3.58	23640.419	60.70523	227.36468	-1.773931	2.1055366	2.6615527	24163.702	48.06545	491.6434	-2.250902	1.911759	-0.057382
175	3.59	17686.109	41.379762	166.23749	-1.816747	1.7274479	2.1031212	18077.961	20.76682	366.3343	-2.338043	1.494105	-0.501559
200	3.60	13412.75	25.142787	112.78127	-1.866928	1.438009	1.5577663	13741.798	12.24775	264.4619	-2.440034	0.93351	-1.044938

### C.1.2: #635 Stainless Steel - 63.12% Porosity

Operating Frequency [Hz]	Charge Pressure [MPa]	P1 Location						P2 Location					
		Pressure Amplitude			Phase Angle			Pressure Amplitude			Phase Angle		
		Z <sub>1</sub> [Pa]	Z <sub>2</sub> [Pa]	Z <sub>3</sub> [Pa]	φ <sub>1</sub> [rad]	φ <sub>2</sub> [rad]	φ <sub>3</sub> [rad]	Z <sub>1</sub> [Pa]	Z <sub>2</sub> [Pa]	Z <sub>3</sub> [Pa]	φ <sub>1</sub> [rad]	φ <sub>2</sub> [rad]	φ <sub>3</sub> [rad]
50 (low)	N/A	N/A	N/A	N/A	N/A	N/A	N/A	N/A	N/A	N/A	N/A	N/A	N/A
50	2.85	147590.37	3217.8941	1362.6494	-0.329192	-0.682207	0.5248245	118792.31	2502.873	1972.628	-1.022544	-1.512821	-2.628701
75	2.86	107330.49	1378.4289	824.38887	-1.074524	-2.242725	-2.339433	72624.989	902.7357	1242.613	-1.949059	1.226228	0.720132
100	2.87	56475.396	209.11615	349.62885	-1.424009	-2.917525	2.5602481	34727.634	213.9456	417.5508	-2.382826	2.231943	-0.623303
125	2.88	34997.957	102.69089	192.87035	-1.615848	2.2777514	1.8696013	19560.115	85.24363	162.8348	-2.65284	1.779422	-1.416663
150	2.89	24176.203	63.074967	92.718361	-1.78129	2.398692	1.5014844	12253.252	36.5845	69.47417	-2.886879	1.22709	-2.146775
175	2.89	18136.816	36.957364	82.292926	-1.832697	1.9592772	1.4003039	8339.582	16.66052	34.8502	-2.987969	1.021471	-2.425549
200	2.90	13983.829	20.155364	72.638655	-1.923743	1.5418588	1.0546548	5871.3979	7.693382	25.5438	-1.871996	0.62644	-2.822277
50 (low)	3.51	19088.781	103.80191	285.60709	-0.166976	-0.555715	0.9448448	18253.97	92.46106	190.1794	-0.632842	-1.161224	-0.313177
50	3.52	180755.61	3995.7974	1906.6753	-0.191666	-0.386717	1.149865	154317.01	3310.837	2850.516	-0.821646	-1.159178	-1.963449
75	3.54	136687.98	1823.6137	1262.3705	-1.020686	-2.108179	-2.022732	99572.808	1311.727	1962.414	-1.837257	-3.021898	1.102069
100	3.57	69586.953	284.51779	513.61208	-1.399144	-2.980941	2.848919	47632.458	210.0011	821.4078	-2.28722	2.717375	-0.328786
125	3.58	43408.585	39.284851	331.97783	-1.610638	1.871634	1.9124515	27371.452	109.0776	319.0704	-2.57391	1.783891	-1.188748
150	3.60	30339.898	67.333911	144.88069	-1.764164	2.4388818	1.5357802	17723.834	48.48904	158.0443	-2.796165	1.325521	-1.886761
175	3.61	22500.907	34.02634	114.11711	-1.829515	1.8784083	1.3390103	12133.787	22.19428	82.0865	-2.912202	1.116793	-2.174806
200	3.62	17115.22	16.704856	93.600018	-1.89535	1.5026132	1.0781601	8556.6825	9.258438	46.69227	-3.030647	0.817146	-2.477838

## C.2: Oscillatory Radial Flow Pressure Waveform Data

### C.2.1: #325 Phosphor Bronze - 67.02% Porosity

Operating Frequency [Hz]	Charge Pressure [MPa]	P1 Location						P2 Location					
		Pressure Amplitude			Phase Angle			Pressure Amplitude			Phase Angle		
		Z <sub>1</sub> [Pa]	Z <sub>2</sub> [Pa]	Z <sub>3</sub> [Pa]	φ <sub>1</sub> [rad]	φ <sub>2</sub> [rad]	φ <sub>3</sub> [rad]	Z <sub>1</sub> [Pa]	Z <sub>2</sub> [Pa]	Z <sub>3</sub> [Pa]	φ <sub>1</sub> [rad]	φ <sub>2</sub> [rad]	φ <sub>3</sub> [rad]
50 (low)	2.81	2002.9864	3.1172439	19.483102	-0.49867	-1.195894	0.7757049	1994.8105	3.658344	21.30657	-0.783828	-1.996435	-0.591304
50	2.85	26747.527	180.57866	761.37586	-0.577993	-2.682118	1.5419516	25533.802	45.58953	109.93	-0.976404	1.940982	-1.098517
75	2.85	10643.205	96.495127	320.454	-0.91525	2.8512207	-0.052014	10503.616	30.89921	62.7784	-1.465524	0.734359	-1.171031
100	2.82	5300.6577	77.437294	180.90232	-1.019114	1.9521848	-1.370853	5407.6278	15.61316	45.07041	-1.760129	-0.134483	1.84588
125	2.79	3483.8122	35.044858	174.83465	-0.98961	0.7785852	-2.028255	3548.819	22.63466	34.70064	-1.959177	-0.63539	1.444436
150	2.83	2478.0836	25.755083	194.36235	-0.888708	0.9956958	-2.881213	2513.4721	7.222837	34.32147	-2.103316	-1.150059	0.569564
175	2.82	2030.2269	26.131489	230.2403	-0.700039	0.9648969	2.3242513	1909.0325	8.535668	35.31762	-2.174384	-1.444093	-0.511169
200	2.79	1845.1563	31.076126	143.35001	-0.548565	0.8263699	1.3379338	1518.7291	9.309846	19.47956	-2.260749	-1.721092	-1.547708
50 (low)	3.41	1720.7327	2.59744	17.934668	-0.578493	-1.306015	0.6024033	1734.8191	2.974345	21.66893	-0.812179	-1.439653	-0.608351
50	3.46	32000.07	198.84277	890.03542	-0.618078	-2.717463	1.5899815	31061.39	65.68119	117.2504	-0.972874	1.983581	-1.085019
75	3.43	11982.698	111.12291	361.64476	-0.963043	2.8782205	0.0284917	12247.277	41.41215	67.82096	-1.450409	0.806113	2.296697
100	3.43	6319.6937	100.42051	239.45018	-1.076005	2.1078493	-1.214428	6840.5356	24.60546	51.06803	-1.742403	-0.067459	1.996633
125	3.43	4555.7275	75.956655	276.97946	-1.059081	1.024893	-1.893863	5084.9337	22.77976	61.71649	-1.960446	-1.03297	1.24895
150	3.44	2552.7108	30.738076	273.13339	-0.139696	1.1837529	-2.978156	1081.4463	4.04729	16.25244	-2.106855	-1.221428	0.331062
175	3.45	2933.8971	52.902265	326.90194	-0.053889	1.1210383	2.1347603	976.05045	7.588985	17.98355	-2.177442	-1.544669	-0.83157
200	3.41	2749.0083	64.156381	164.15002	0.0077237	0.9099173	1.2993289	739.48832	8.157872	8.773751	-2.24774	-1.770178	-1.765466

### C.2.2: #635 Stainless Steel - 63.04% Porosity

Operating Frequency [Hz]	Charge Pressure [MPa]	P1 Location						P2 Location					
		Pressure Amplitude			Phase Angle			Pressure Amplitude			Phase Angle		
		Z <sub>1</sub> [Pa]	Z <sub>2</sub> [Pa]	Z <sub>3</sub> [Pa]	φ <sub>1</sub> [rad]	φ <sub>2</sub> [rad]	φ <sub>3</sub> [rad]	Z <sub>1</sub> [Pa]	Z <sub>2</sub> [Pa]	Z <sub>3</sub> [Pa]	φ <sub>1</sub> [rad]	φ <sub>2</sub> [rad]	φ <sub>3</sub> [rad]
50 (low)	2.85	1232.7906	15.278732	29.401992	0.0534443	-2.353655	0.3374401	696.20947	5.055819	6.891759	-1.029673	2.268736	-1.539297
50	2.85	17396.073	176.57134	485.63147	0.0029146	-1.870505	1.0554052	8905.9974	26.65801	31.59151	-1.128788	0.695452	-1.686481
75	2.83	9529.557	114.75523	217.76993	-0.232226	2.5158003	-0.640715	3665.9149	14.02409	19.73583	-1.588219	-0.025784	0.743796
100	2.88	6614.3126	99.198198	156.30405	-0.342435	1.6660458	-1.883797	2028.3033	9.215797	9.753454	-1.861258	-0.763309	1.895677
125	2.87	4714.2157	45.641673	111.50353	-0.386106	1.0244499	-2.505282	1181.8302	21.36257	8.044975	-2.031199	0.144823	1.538424
150	2.86	4375.4126	29.388321	134.95334	-0.436419	0.6729551	2.9098056	912.02986	2.794342	7.207506	-2.190775	-1.247744	0.316532
175	2.86	3903.5008	27.999592	147.93792	-0.415548	0.7736585	2.2121939	690.23889	2.971406	6.17688	-2.257054	-1.835233	-0.334797
200	2.84	3575.7944	22.734725	119.87041	-0.442706	0.495988	1.4971022	544.23295	3.458423	4.513052	-2.362396	-2.048126	-1.346796
50 (low)	3.44	1346.5885	2.3024697	48.01697	0.1282873	0.4967092	0.9715007	867.66685	1.206455	12.10717	-0.87714	1.096575	-0.879228
50	3.46	18517.671	207.56053	629.6631	-0.033729	-3.04143	1.1360351	10731.183	35.28367	45.94108	-1.10128	0.930515	-1.476418
75	3.45	9795.261	127.89345	284.86311	-0.260944	2.5692355	-0.553607	4437.8953	10.68616	26.91851	-1.576306	-0.23093	1.906997
100	3.47	7376.9867	127.01148	246.4748	-0.334594	1.8116293	-1.706504	2652.509	11.67686	15.953	-1.84134	-0.651842	1.995508
125	3.46	5894.7166	76.504053	202.09136	-0.370628	0.8559628	-2.313	1722.297	17.72948	12.61733	-2.019811	-0.492765	1.201896
150	3.44	4771.9156	40.314789	191.60295	-0.401728	0.5751424	3.0474723	1163.9092	3.391156	10.13349	-2.18334	-1.515363	0.425958
175	3.44	4338.4991	35.496772	212.26899	-0.375046	0.7185794	2.2153209	895.63927	4.328376	9.522137	-2.256791	-1.907997	-0.496028
200	3.44	4025.706	39.900225	158.69723	-0.375258	0.3722677	1.4110368	711.01836	4.644817	5.953522	-2.348379	-2.32559	-1.489004

### C.3: Oscillatory Axial Flow Pressure Plot Comparison Data

#### C.3.1: #325 Phosphor Bronze - 67.38% Porosity

Operating Frequency [Hz]	Charge Pressure [MPa]	Experimental Data			Simulated Data			Error	
		P1 [kPa]	P2 [kPa]	$\phi$ [rad]	P1 [kPa]	P2 [kPa]	$\phi$ [rad]	$\Delta P2$ [%]	$\Delta\phi$ [deg]
50 (low)	2.84	17.3930	18.5390	-0.0314	17.3930	17.4090	0.0000	6.0953	1.7991
50	2.84	111.8000	117.4200	-0.1571	111.8000	111.6400	-0.1100	4.9225	2.6986
75	2.85	85.7860	87.5340	-0.3770	85.7860	84.6580	-0.3063	3.2856	4.0508
100	2.86	44.7820	45.4100	-0.4084	44.7820	44.0310	-0.3456	3.0368	3.5982
125	2.87	27.3110	27.7460	-0.4712	27.3110	26.8250	-0.4084	3.3194	3.5982
150	2.88	18.9440	18.9200	-0.5089	18.9430	18.4430	-0.4241	2.5211	4.8587
175	2.88	13.6880	13.5360	-0.5608	13.6880	13.2510	-0.4948	2.1055	3.7815
200	2.88	8.6375	8.5405	-0.5655	8.6375	8.3837	-0.5027	1.8360	3.5982
50 (low)	3.51	4.0470	4.3651	-0.1257	4.0470	4.0756	-0.0157	6.6322	6.3025
50	3.51	150.0500	159.1400	-0.1100	150.0500	150.3000	-0.0785	5.5549	1.8048
75	3.53	116.3700	120.6000	-0.3534	116.3600	115.6500	-0.3063	4.1045	2.6986
100	3.55	57.7330	60.1910	-0.3770	57.7330	57.5660	-0.3142	4.3611	3.5982
125	3.56	34.8060	36.2960	-0.4084	34.8060	34.7660	-0.3456	4.2153	3.5982
150	3.58	23.6680	24.6680	-0.4524	23.6680	23.6770	-0.3958	4.0174	3.2429
175	3.59	17.7650	18.4560	-0.4948	17.7640	17.7690	-0.4288	3.7224	3.7815
200	3.60	13.4980	14.0160	-0.5341	13.4980	13.5250	-0.4712	3.5031	3.6039

#### C.3.2: #635 Stainless Steel - 63.12% Porosity

Operating Frequency [Hz]	Charge Pressure [MPa]	Experimental Data			Simulated Data			Errors	
		P1 [kPa]	P2 [kPa]	$\phi$ [rad]	P1 [kPa]	P2 [kPa]	$\phi$ [rad]	$\Delta P2$ [%]	$\Delta\phi$ [deg]
50 (low)	N/A	N/A	N/A	N/A	N/A	N/A	N/A	N/A	N/A
50	2.85	150.9300	122.8200	-0.5812	150.9300	125.5700	-0.5027	2.2390	4.4977
75	2.86	109.2400	74.1810	-0.8482	109.2400	77.5640	-0.7775	4.5605	4.0508
100	2.87	56.9840	35.2960	-0.9111	56.9840	35.5340	-0.9111	0.6743	0.0000
125	2.88	35.2440	19.7780	-0.9739	35.2440	19.3360	-0.9739	2.2348	0.0000
150	2.89	24.3140	12.3490	-1.0179	24.3140	11.8190	-1.0462	4.2918	1.6215
175	2.89	18.2330	8.3858	-1.0556	18.2320	7.9073	-1.0886	5.7061	1.8908
200	N/A	N/A	N/A	N/A	N/A	N/A	N/A	N/A	N/A
50 (low)	3.51	19.2420	18.3520	-0.3299	19.2420	17.2960	-0.3142	5.7541	0.8995
50	3.52	184.5400	159.8800	-0.5027	184.5400	161.7900	-0.3927	1.1946	6.3025
75	3.54	139.1800	102.5200	-0.8011	139.1700	107.1500	-0.7069	4.5162	5.3973
100	3.57	70.2440	48.5470	-0.8482	70.2430	48.9220	-0.8168	0.7724	1.7991
125	3.58	43.7220	27.7670	-0.9111	43.7220	27.3870	-0.8796	1.3685	1.8048
150	3.60	30.5280	17.9170	-0.9613	30.5280	17.2750	-0.9613	3.5832	0.0000
175	3.61	22.6240	12.2300	-0.9896	22.6220	11.5910	-1.0226	5.2249	1.8908
200	3.62	17.2070	8.6083	-1.0681	17.2070	8.0364	-1.0996	6.6436	1.8048

## C.4: Oscillatory Radial Flow Pressure Plot Comparison Data

### C.4.1: #325 Phosphor Bronze - 67.02% Porosity

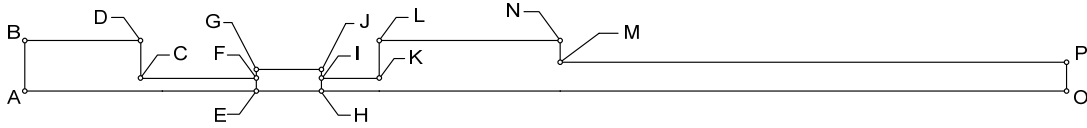
Operating Frequency	Charge Pressure	Experimental Data			Simulated Data			Errors	
		P1	P2	$\phi$	P1	P2	$\phi$	$\Delta P2$	$\Delta\phi$
[Hz]	[MPa]	[kPa]	[kPa]	[rad]	[kPa]	[kPa]	[rad]	[ % ]	[deg]
50 (low)	2.81	1.9939	1.9950	-0.1728	1.9938	2.0866	-0.2042	4.5915	1.7991
50	2.85	25.9840	25.4730	-0.3142	26.0120	26.7790	-0.3142	5.1270	0.0000
75	2.85	10.3540	10.4140	-0.5184	10.3280	11.0070	-0.5419	5.6943	1.3465
100	2.82	5.2463	5.4225	-0.7226	5.2234	5.6249	-0.7540	3.7326	1.7991
125	2.79	3.5772	3.5447	-0.9425	3.5545	3.6848	-1.0053	3.9524	3.5982
150	2.83	2.6453	2.5352	-1.1592	2.6287	2.5573	-1.2723	0.8717	6.4802
175	2.82	2.0464	1.9349	-1.3854	2.0350	1.9041	-1.4844	1.5918	5.6723
200	2.79	1.7057	1.5203	-1.6022	1.6971	1.4567	-1.7279	4.1834	7.2021
50 (low)	3.41	1.7113	1.7334	-0.1257	1.7112	1.8192	-0.1571	4.9498	1.7991
50	3.46	31.1970	30.9850	-0.2670	31.1720	32.6320	-0.2827	5.3155	0.8995
75	3.43	11.6400	12.1820	-0.4477	11.6180	12.8930	-0.4712	5.8365	1.3465
100	3.43	6.1930	6.8478	-0.6597	6.1666	7.1951	-0.6912	5.0717	1.8048
125	3.43	4.6182	5.1052	-0.8796	4.5806	5.3387	-0.9425	4.5738	3.6039
150	3.44	2.4001	1.0927	-1.9227	2.3830	1.0587	-1.9792	3.1116	3.2372
175	3.45	2.9060	0.9842	-2.0122	2.8978	0.9496	-2.0782	3.5113	3.7815
200	3.41	2.8825	0.7345	-2.1677	2.8759	0.7037	-2.2305	4.1953	3.5982

### C.4.2: #635 Stainless Steel - 63.04% Porosity

Operating Frequency	Charge Pressure	Experimental Data			Simulated Data			Errors	
		P1	P2	$\phi$	P1	P2	$\phi$	$\Delta P2$	$\Delta\phi$
[Hz]	[MPa]	[kPa]	[kPa]	[rad]	[kPa]	[kPa]	[rad]	[ % ]	[deg]
50 (low)	2.85	1.2499	0.6945	-0.9739	1.2489	0.7087	-1.0053	2.0355	1.7991
50	2.85	17.6080	8.8763	-1.0210	17.4420	9.0511	-1.0524	1.9693	1.7991
75	2.83	9.6339	3.6662	-1.2723	9.5660	3.6736	-1.2959	0.2018	1.3522
100	2.88	6.6499	2.0230	-1.4451	6.6134	2.0187	-1.4765	0.2126	1.7991
125	2.87	4.7344	1.1733	-1.5708	4.7152	1.1685	-1.6022	0.4091	1.7991
150	2.86	4.3237	0.9152	-1.6399	4.3081	0.8980	-1.6965	1.8806	3.2429
175	2.86	3.7632	0.6937	-1.7153	3.7519	0.6782	-1.7813	2.2390	3.7815
200	2.84	3.4708	0.5450	-1.8221	3.4626	0.5291	-1.8535	2.9114	1.7991
50 (low)	3.44	1.3907	0.8651	-0.8796	1.3895	0.8553	-0.9425	1.1366	3.6039
50	3.46	18.5930	10.6850	-0.9582	18.4070	10.5520	-1.0053	1.2447	2.6986
75	3.45	9.9464	4.4528	-1.2252	9.8707	4.2752	-1.2723	3.9885	2.6986
100	3.47	7.4706	2.6466	-1.4137	7.4227	2.5297	-1.4765	4.4170	3.5982
125	3.46	5.9783	1.7131	-1.5708	5.9469	1.6331	-1.6022	4.6699	1.7991
150	3.44	4.7172	1.1686	-1.6682	4.6980	1.0974	-1.7247	6.0928	3.2372
175	3.44	4.1346	0.9014	-1.7483	4.1205	0.8424	-1.8143	6.5490	3.7815
200	3.44	3.9316	0.7122	-1.8535	3.9217	0.6621	-1.9164	7.0340	3.6039

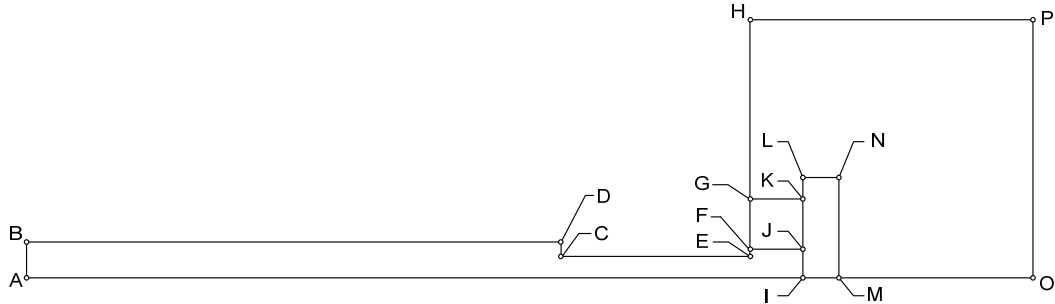
## APPENDIX D: SIMULATION DIMENSIONS

### D.1: Steady Axial Flow Experimental Setup Grid Vertices



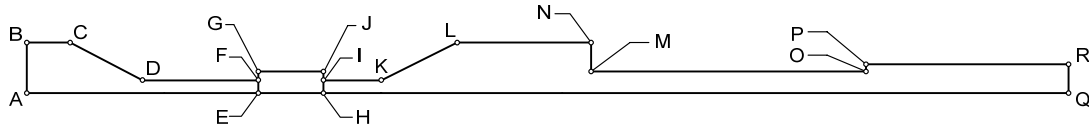
Vertex	Coordinates	
	x mm	y mm
A	0.00000	0.00000
B	0.00000	4.21640
C	20.32000	1.00330
D	20.32000	4.21640
E	50.80000	0.00000
F	50.80000	1.00330
G	50.80000	2.00660
H	63.50000	0.00000
I	63.50000	1.00330
J	63.50000	2.00660
K	74.93000	1.00330
L	74.93000	4.21640
M	103.37800	2.28600
N	103.37800	4.21640
O	208.78800	0.00000
P	208.78800	2.28600

## D.2: Steady Radial Flow Experimental Setup Grid Vertices



Vertex	#635 SS Coordinates		#325 PhBrz Coordinates	
	x mm	y mm	x mm	y mm
A	0.00000	0.00000	0.00000	0.00000
B	0.00000	2.34950	0.00000	2.34950
C	109.83400	1.65000	109.83400	1.65000
D	109.83400	2.34950	109.83400	2.34950
E	132.33400	1.65000	132.33400	1.65000
F	132.33400	2.00000	132.33400	2.00000
G	132.33400	10.00000	132.33400	10.00000
H	132.33400	32.89300	132.33400	32.89300
I	138.43400	0.00000	135.73400	0.00000
J	138.43400	2.00000	135.73400	2.00000
K	138.43400	10.00000	135.73400	10.00000
L	138.43400	14.98600	135.73400	14.98600
M	144.27600	0.00000	140.81400	0.00000
N	144.27600	14.98600	140.81400	14.98600
O	170.43400	0.00000	170.43400	0.00000
P	170.43400	32.89300	170.43400	32.89300

### D.3: Oscillatory Axial Flow Experimental Setup Grid Vertices



Vertex	Coordinates	
	x mm	Y mm
A	0.00000	0.00000
B	0.00000	4.21640
C	5.08000	4.21640
D	27.94000	1.00330
E	39.37000	0.00000
F	39.37000	1.00330
G	39.37000	2.00660
H	52.07000	0.00000
I	52.07000	1.00330
J	52.07000	2.00660
K	82.55000	1.00330
L	105.41000	4.21640
M	135.89000	2.34950
N	135.89000	4.21640
O	169.16400	2.34950
P	169.16400	2.79400
Q	202.05700	0.00000
R	202.05700	2.79400



#### D.4.2: Small Radial Housing Unit

#325 PhBrz Coordinates		
Vertex	x mm	y mm
A	0.00000	0.00000
B	0.00000	2.35000
C	108.38620	1.65000
D	108.38620	2.35000
E	130.88620	1.65000
F	130.88620	2.00000
G	130.88620	10.00000
H	130.88620	33.02000
I	134.28620	0.00000
J	134.28620	2.00000
K	134.28620	10.00000
L	134.28620	14.98600
M	139.36620	0.00000
N	139.36620	14.98600
O	158.82620	2.35000
P	158.82620	33.02000
Q	325.95820	0.00000
R	325.95820	2.35000

## APPENDIX E: PRESSURE DEPENDENCE STUDY

### E.1: Experimental Data

#### E.1.2: #325 Stainless Steel - 69.69% Porosity

300 PSIG SUPPLY PRESSURE			
Mass Flow [g/s]	Static Pressure		
	P1 [kPa]	P2 [kPa]	$\Delta P$ [kPa]
0.083	1998.1	1982.9	15.2
0.212	1970.5	1938.8	31.7
0.379	1947.1	1884.3	62.7
0.610	1920.9	1801.6	119.3
0.833	1898.8	1707.1	191.7
1.161	1866.4	1535.5	330.9
1.443	1840.2	1356.2	484.0
0.059	2002.2	1993.3	9.0
0.203	1974.0	1947.8	26.2
0.356	1951.2	1900.2	51.0
0.590	1921.6	1814.7	106.9
0.820	1896.1	1716.1	180.0
1.020	1872.6	1613.4	259.2
1.236	1850.6	1488.6	362.0
1.452	1828.5	1344.5	484.0
0.054	2011.9	2006.4	5.5
0.278	1975.3	1950.5	24.8
0.495	1944.3	1884.3	60.0
0.671	1916.7	1807.1	109.6
0.876	1885.7	1699.6	186.2
1.128	1854.7	1561.0	293.7
1.383	1825.7	1398.9	426.8
0.185	1979.5	1956.7	22.8
0.313	1962.9	1922.3	40.7
0.476	1925.7	1851.9	73.8
0.673	1893.3	1765.1	128.2
0.895	1860.9	1658.2	202.7
1.185	1829.2	1498.2	330.9

<b>400 PSIG SUPPLY PRESSURE</b>			
Mass Flow [g/s]	Static Pressure		
	P1 [kPa]	P2 [kPa]	$\Delta P$ [kPa]
0.093	2654.5	2640.7	13.8
0.191	2626.9	2599.3	27.6
0.310	2606.9	2564.8	42.1
0.463	2585.5	2516.6	68.9
0.549	2570.4	2489.0	81.4
0.624	2558.6	2461.4	97.2
0.730	2542.8	2420.1	122.7
0.847	2524.9	2371.8	153.1
0.964	2507.6	2323.5	184.1
1.128	2485.6	2254.6	231.0
1.224	2471.1	2195.3	275.8
0.240	2639.3	2599.3	40.0
0.458	2589.7	2523.5	66.2
0.705	2545.5	2427.0	118.6
0.882	2515.9	2351.1	164.8
1.122	2482.1	2247.7	234.4
1.404	2443.5	2102.9	340.6
0.278	2593.1	2558.0	35.2
0.500	2544.2	2468.3	75.8
0.706	2503.5	2392.5	111.0
0.917	2471.1	2302.8	168.2
1.181	2432.5	2185.6	246.8

<b>500 PSIG SUPPLY PRESSURE</b>			
Mass Flow [g/s]	Static Pressure		
	P1 [kPa]	P2 [kPa]	$\Delta P$ [kPa]
0.326	3192.3	3150.9	41.4
0.575	3144.0	3075.1	68.9
0.753	3116.4	3013.0	103.4
0.978	3082.0	2930.3	151.7
1.110	3061.3	2882.0	179.3
1.383	3026.8	2764.8	262.0
0.122	3219.9	3213.0	6.9
0.257	3192.3	3164.7	27.6
0.447	3157.8	3109.5	48.3
0.566	3137.1	3075.1	62.1
0.735	3109.5	3013.0	96.5
0.838	3095.7	2978.5	117.2
1.070	3061.3	2888.9	172.4
1.239	3033.7	2820.0	213.7
1.458	3006.1	2723.4	282.7
0.168	3275.0	3261.2	13.8
0.401	3213.0	3171.6	41.4
0.704	3144.0	3061.3	82.7
0.953	3102.6	2971.6	131.0
1.140	3075.1	2895.8	179.3

E.1.2: #400 Stainless Steel - 69.69% Porosity

300 PSIG SUPPLY PRESSURE			
Mass Flow [g/s]	Static Pressure		
	P1 [kPa]	P2 [kPa]	$\Delta P$ [kPa]
0.039	2167.0	2158.7	8.3
0.113	2135.3	2116.7	18.6
0.209	2103.6	2068.4	35.2
0.368	2057.4	1985.0	72.4
0.542	2015.3	1889.2	126.2
0.664	1987.1	1815.4	171.7
0.856	1947.8	1685.1	262.7
1.031	1909.8	1547.9	362.0
1.221	1866.4	1366.5	499.9
1.434	1818.1	1110.7	707.4
0.093	2149.1	2144.3	4.8
0.172	2117.4	2102.9	14.5
0.313	2068.4	2020.2	48.3
0.372	2046.4	1985.7	60.7
0.517	2002.9	1889.2	113.8
0.760	1941.6	1722.3	219.3
0.930	1893.3	1581.7	311.6
1.252	1793.3	1236.2	557.1
0.034	2013.3	2000.9	12.4
0.180	1971.9	1933.3	38.6
0.291	1945.7	1887.1	58.6
0.442	1926.4	1823.0	103.4
0.574	1911.9	1763.7	148.2
0.871	1883.6	1599.6	284.1
1.020	1869.9	1501.0	368.9
1.314	1844.3	1267.9	576.4
1.464	1830.6	1122.5	708.1
0.181	1954.0	1919.5	34.5
0.358	1910.5	1836.1	74.5
0.546	1872.6	1732.7	140.0
0.782	1832.6	1586.5	246.1
1.016	1799.5	1414.8	384.7
1.203	1772.0	1254.2	517.8

400 PSIG SUPPLY PRESSURE			
Mass Flow [g/s]	Static Pressure		
	P1 [kPa]	P2 [kPa]	$\Delta P$ [kPa]
0.131	2654.5	2633.8	20.7
0.270	2626.9	2592.4	34.5
0.443	2608.3	2530.4	77.9
0.665	2595.2	2461.4	133.8
0.795	2573.8	2399.4	174.4
0.912	2561.4	2344.2	217.2
1.185	2542.1	2213.2	328.9
1.359	2514.5	2096.0	418.5
1.503	2500.0	1999.5	500.6
0.179	2620.0	2606.2	13.8
0.406	2592.4	2530.4	62.1
0.630	2566.2	2447.6	118.6
0.804	2550.4	2378.7	171.7
0.930	2537.3	2316.6	220.6
1.158	2513.1	2199.4	313.7

500 PSIG SUPPLY PRESSURE			
Mass Flow [g/s]	Static Pressure		
	P1 [kPa]	P2 [kPa]	$\Delta P$ [kPa]
0.185	3275.0	3261.2	13.8
0.359	3219.9	3178.5	41.4
0.536	3199.2	3123.3	75.8
0.749	3178.5	3054.4	124.1
0.987	3178.5	2985.4	193.1
1.200	3144.0	2875.1	268.9
1.380	3130.2	2792.4	337.8
0.107	3254.3	3240.5	13.8
0.272	3206.1	3171.6	34.5
0.464	3178.5	3109.5	68.9
0.653	3178.5	3075.1	103.4
0.900	3123.3	2951.0	172.4
1.052	3102.6	2888.9	213.7
1.344	3068.2	2744.1	324.1

E.1.3: #400 Sintered Stainless Steel - 61.65% Porosity

300 PSIG SUPPLY PRESSURE			
Mass Flow [g/s]	Static Pressure		
	P1 [kPa]	P2 [kPa]	$\Delta P$ [kPa]
0.116	1956.7	1909.2	47.6
0.268	1931.2	1792.6	138.6
0.429	1911.2	1634.7	276.5
0.567	1896.1	1466.5	429.5
0.701	1883.0	1259.0	624.0
0.079	1987.1	1954.7	32.4
0.130	1967.1	1911.9	55.2
0.232	1951.2	1834.0	117.2
0.330	1937.4	1747.8	189.6
0.384	1929.8	1696.1	233.7
0.433	1922.9	1643.0	279.9
0.507	1928.5	1574.1	354.4
0.544	1910.5	1510.6	399.9
0.623	1899.5	1392.1	507.5
0.660	1894.0	1334.1	559.9

400 PSIG SUPPLY PRESSURE			
Mass Flow [g/s]	Static Pressure		
	P1 [kPa]	P2 [kPa]	$\Delta P$ [kPa]
0.132	2647.6	2606.2	41.4
0.272	2615.9	2509.7	106.2
0.360	2601.4	2440.7	160.6
0.444	2588.3	2371.8	216.5
0.540	2575.2	2289.1	286.1
0.618	2564.8	2213.2	351.6
0.762	2544.2	2040.8	503.3
0.845	2532.4	1937.4	595.0
0.088	2647.6	2620.0	27.6
0.100	2640.7	2613.1	27.6
0.161	2626.9	2571.7	55.2
0.238	2620.0	2530.4	89.6
0.456	2593.8	2364.9	228.9
0.535	2574.5	2289.1	285.4
0.589	2566.2	2240.8	325.4
0.674	2554.5	2144.3	410.2
0.840	2530.4	1930.5	599.8

500 PSIG SUPPLY PRESSURE			
Mass Flow [g/s]	Static Pressure		
	P1 [kPa]	P2 [kPa]	$\Delta P$ [kPa]
0.097	3226.7	3206.1	20.7
0.286	3192.3	3095.7	96.5
0.405	3171.6	3019.9	151.7
0.521	3150.9	2930.3	220.6
0.635	3137.1	2840.6	296.5
0.848	3102.6	2626.9	475.7
1.065	3068.2	2364.9	703.3
0.101	3309.5	3281.9	27.6
0.330	3247.4	3130.2	117.2
0.491	3213.0	3013.0	199.9
0.630	3178.5	2888.9	289.6
0.740	3157.8	2792.4	365.4
0.956	3116.4	2558.0	558.5
0.110	3302.6	3268.1	34.5
0.333	3247.4	3123.3	124.1
0.425	3219.9	3054.4	165.5
0.584	3185.4	2930.3	255.1
0.707	3157.8	2813.1	344.7
0.816	3137.1	2709.6	427.5
1.002	3102.6	2495.9	606.7

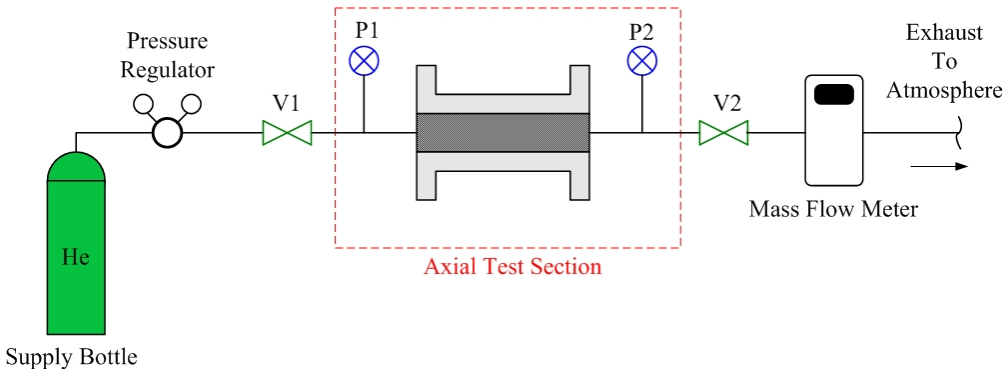
E.1.4: Metal Foam - 55.47% Porosity

300 PSIG SUPPLY PRESSURE			
Mass Flow [g/s]	Static Pressure		
	P1 [kPa]	P2 [kPa]	$\Delta P$ [kPa]
0.032	2025.0	2021.5	3.4
0.156	1994.0	1970.5	23.4
0.308	1967.8	1908.5	59.3
0.444	1952.6	1845.7	106.9
0.575	1942.3	1777.5	164.8
0.783	1929.2	1648.5	280.6
0.951	1919.5	1520.3	399.2
1.113	1907.1	1368.6	538.5
1.296	1894.7	1174.2	720.5
0.832	1925.7	1658.9	266.8
1.161	1891.9	1339.7	552.3
1.296	1883.6	1185.9	697.7
0.103	2011.2	2000.9	10.3
0.278	1974.7	1934.7	40.0
0.377	1958.1	1887.1	71.0
0.510	1939.5	1814.7	124.8
0.799	1905.0	1624.4	280.6
1.128	1866.4	1321.0	545.4

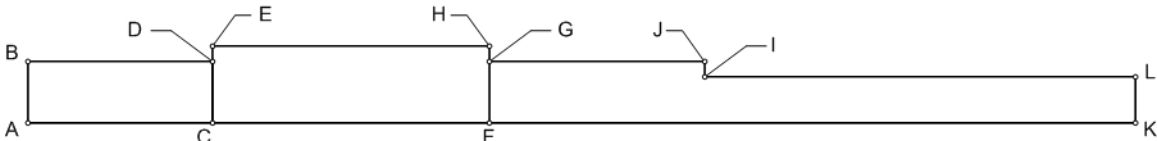
<b>400 PSIG SUPPLY PRESSURE</b>			
Mass Flow [g/s]	Static Pressure		
	P1 [kPa]	P2 [kPa]	$\Delta P$ [kPa]
0.078	2695.9	2689.0	6.9
0.165	2668.3	2654.5	13.8
0.326	2640.7	2599.3	41.4
0.485	2620.0	2530.4	89.6
0.668	2592.4	2447.6	144.8
0.816	2571.7	2364.9	206.8
0.989	2544.2	2254.6	289.6
1.181	2523.5	2130.5	393.0
1.347	2502.8	1992.6	510.2
1.533	2475.2	1820.2	655.0
0.059	2716.5	2709.6	6.9
0.287	2661.4	2620.0	41.4
0.396	2633.8	2564.8	68.9
0.509	2613.1	2516.6	96.5
0.681	2578.6	2433.8	144.8
0.844	2558.0	2344.2	213.7
0.948	2537.3	2275.3	262.0
1.087	2516.6	2178.7	337.8
1.230	2495.9	2061.5	434.4
1.452	2454.5	1861.6	592.9

<b>500 PSIG SUPPLY PRESSURE</b>			
Mass Flow [g/s]	Static Pressure		
	P1 [kPa]	P2 [kPa]	$\Delta P$ [kPa]
0.047	3295.7	3281.9	13.8
0.191	3247.4	3213.0	34.5
0.330	3199.2	3150.9	48.3
0.541	3144.0	3047.5	96.5
0.647	3116.4	2999.2	117.2
0.797	3082.0	2909.6	172.4
0.889	3061.3	2861.3	199.9
1.017	3033.7	2778.6	255.1
1.133	2999.2	2695.9	303.4
1.338	2944.1	2523.5	420.6
1.530	2882.0	2337.3	544.7
0.136	3219.9	3213.0	6.9
0.430	3178.5	3116.4	62.1
0.650	3144.0	3026.8	117.2
0.912	3116.4	2909.6	206.8
1.158	3095.7	2778.6	317.2
1.434	3068.2	2606.2	461.9
1.668	3047.5	2427.0	620.5

### E.2: Experimental Setup Control Schematic

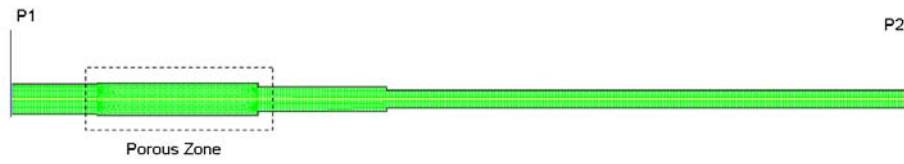


### E.3: Test Setup Grid Vertices



Vertex	Coordinates	
	x mm	y mm
A	0.00000	0.00000
B	0.00000	3.81000
C	20.32000	0.00000
D	20.32000	3.81000
E	20.32000	3.96875
F	58.42000	0.00000
G	58.42000	3.17500
H	58.42000	3.96875
I	88.90000	2.28600
J	88.90000	3.17500
K	212.09000	0.00000
L	212.09000	2.28600

#### E.4: Simulated Fluid Control Volume



## REFERENCES

1. Cha, J.S., "Hydrodynamic Parameters of Micro Porous Media for Steady and Oscillatory Flow: Application to Cryocooler Regenerators," Doctoral Thesis, Georgia Institute of Technology, Atlanta, GA (2007).
2. Cha, J.S., Ghiaasiaan, S.M., Desai, P.V., Harvey, J.P., Kirkconnell, C.S., "Multi-Dimensional Effects in Pulse Tube Refrigerator," *Cryogenics* 46 (2006), pp. 658-665.
3. Cha, J.S., Ghiaasiaan, S.M., Kirkconnell, C.S., "Longitudinal Hydraulic Resistance Parameters of Cryocooler and Stirling Regenerators in Periodic Flow," Proceedings of Cryogenics Engineering Conf. and International Cryogenics Materials Conf., Chattanooga, TN, July 2007.
4. Cha, J.S., Ghiaasiaan, S.M., Kirkconnell, C.S., "Oscillatory Flow Anisotropic Hydrodynamic Parameters of Microporous Media Applied in Pulse Tube and Stirling Cryocooler Regenerators", *Experimental Thermal Fluid Science* 32 (2008), pp. 1264-1278.
5. Cha, J.S., Ghiaasiaan, S.M., Kirkconnell, C.S., Clearman, W.M., "The Impact of Uncertainties Associated with Regenerator Closure Parameters on the Performance of Inertance Tube Pulse Tube Cryocoolers," AIP Conference Proceedings 985 (2007), pp. 243-250.
6. Clearman, W.M., "Measurement and Correlation of Directional Permeability and Forchheimer's Coefficient of Micro Porous Structures Used in Pulse-Tube Cryocoolers," Masters Thesis, Georgia Institute of Technology, Atlanta, GA (2007).
7. Clearman, W.M., Cha, J.S., Ghiaasiaan, S.M., Kirkconnell, C.S., "Anisotropic Steady-Flow Hydrodynamic Parameters of Microporous Media Applied to Pulse Tube and Stirling Cryocooler Regenerators", *Cryogenics* 48 (2008), pp. 112-121.
8. Conrad, T.J., Landrum, E.C., Ghiaasiaan, S.M., Kirkconnell, C.S., Crittenden, T., Yorish, S., "Anisotropic Hydrodynamic Parameters of Regenerator Materials Suitable for Miniature Cryocoolers," Proceedings of Cryocoolers 15, Long Beach, CA (June 2008).

9. Conrad, T.J., Landrum, E.C., Ghiaasiaan, S.M., Kirkconnell, C.S., Crittenden, T., Yorish, S., "CFD Modeling of Meso-Scale and Micro-Scale Pulse Tube Refrigerators," Proceedings of Cryocoolers 15, Long Beach, CA (June 2008).
10. FLUENT 6 Users Manual, Fluent Inc., 2003.
11. Garaway, I., Grossman, G., "A Study of a High Frequency Miniature Reservoir-Less Pulse Tube," AIP Conference Proceedings, Vol. 985 (2008), pp. 1547-1554.
12. Harvey, J. P., "Oscillatory Compressible Flow and Heat Transfer in Porous Media – Application to Cryocooler Regenerators," Doctoral Thesis, Georgia Institute of Technology, Atlanta, GA (2003).
13. Hsu, C., *Handbook of Porous Media* (2<sup>nd</sup> Ed.), Taylor and Francis Group, Boca Raton (2005), pp. 39-64.
14. Hsu, C., Fu, H., Cheng, P., "On Pressure-Velocity Correlation of Steady and Oscillating Flows in Regenerators Made of Wire Screens," *Journal of Fluids Engineering* 121 (1999), pp. 52-56.
15. Ju, Y., Jiang, Y., Zhou, Y., "Experimental Study of the Oscillating Flow Characteristics for a Regenerator in a Pulse Tube Cryocooler," *Cryogenics* 38 (1998), pp. 649-656.
16. Kirkconnell, C. S., "Numerical Analysis of the Mass Flow and Thermal Behavior in High-Frequency Pulse Tubes," Doctoral Thesis, Georgia Institute of Technology, Atlanta, GA (1995).
17. Landrum, E.C., Conrad, T.J., Ghiaasiaan, S.M., Kirkconnell, C.S., "Effect of Pressure on Hydrodynamic Parameters of Several PTR Regenerator Fillers In Axial Steady Flow", Proceedings of Cryocoolers 15, Long Beach, CA, June 2008.
18. Nam, K., Jeong, S., "Investigation of Oscillating Flow Friction Factor for Cryocooler Regenerator Considering Cryogenic Temperature Effect," *Cryogenics* 45 (2006), pp. 733-738.
19. Nam, K., Jeong, S., "Measurement of Cryogenic Regenerator Characteristics Under Oscillating Flow and Pulsating Pressure," *Cryogenics* 43 (2003), pp. 575-581.

20. Nield, D.A., Bejan, A., *Convection in Porous Media* (2<sup>nd</sup> Ed.), Springer, New York (1999), pp. 1-31.
21. Olson, J.R., Swift, G.W., "Acoustic Streaming in Pulse Tube Refrigerators: Tapered Pulse Tubes," *Cryogenics* 37 (1997), pp. 769-776.
22. Organ, A.J., *Thermodynamics & Gas Dynamics of the Stirling Cycle Machine*, Cambridge University Press, (1992), pp. 1-92.
23. Popescu, G., Radcenco, V., Gargalian, E., Ramay Bala, P., "A Critical Review of Pulse Tube Cryogenerator Research," *International Journal of Refrigeration* 24 (2001), pp. 230-237.
24. Radebaugh, R., "Development of the Pulse Tube Refrigerator as an Efficient and Reliable Cryocooler," National Institute of Standards and Technology, Submitted to Proc. Institute of Refrigeration, London, 1999-2000.
25. Radebaugh, R., Gully, W., "Foundations of Cryocoolers Short Course," Presented at the 15<sup>th</sup> International Cryocooler Conference, Long Beach, CA, June 9<sup>th</sup>, 2008.
26. Richardson, R.N., Evans, B.E., "A Review of Pulse Tube Refrigeration," *International Journal of Refrigeration* 20 (1997), pp. 367-373.
27. Ross Jr., R.G., Johnson, D.L., "Effect of Gravity Orientation on the Thermal Performance of Stirling-Type Pulse Tube Cryocoolers," *Cryogenics* 44 (2004), pp. 403-408.
28. Scott Specialty Gases, "How to Choose a Gas Regulator that's Right for your Application," <http://www.scottcatalog.com/scotttec.nsf/74923c9ec562a6fb85256825006eb87d/057078ba0233fc8a85256b8f0059ad09?opendocument> (Accessed July 28<sup>th</sup>, 2008).
29. Shen, Q.Q., Ju, Y.L., "A New Correlation of Friction Factor for Oscillating Flow Regenerator Operating at High Frequencies," AIP Conference Proceedings 985 (2008), pp. 267-274.
30. Sonntag, R.E., Borgnakke, C., Van Wylen, G.J., *Fundamentals of Thermodynamics* (6<sup>th</sup> Ed.), John Wiley & Sons, (2003), pp. 433-434.

31. Wilson, L., Narasimhan, A., Venkateshan, S.P., "Permeability and Form Coefficient Measurement of Porous Inserts With Non-Darcy Model Using Non-Plug Flow Experiments," *Journal of Fluids Engineering* 128 (2006), pp. 638-642.
32. Zhu, S.W., Zhou, S.L., Yoshimura, N., Matsubara, Y., "Phase Shift Effect of the Long Neck Tube for Pulse Tube Refrigerator," Proceedings of Cryocoolers 9, Waterville Valley, New Hampshire (June 1996).